Combined pseudo-spectral / actuator line model for wind turbine applications

Dag, Kaya Onur

Publication date:
2017

Document Version
Publisher's PDF, also known as Version of record

Citation (APA):
Dag, K. O. (2017). *Combined pseudo-spectral / actuator line model for wind turbine applications*. DTU Wind Energy PhD Vol. 67

Combined pseudo-spectral / actuator line model for wind turbine applications

Department of
Wind Energy
PhD Report 2017

Kaya Onur Dag

DTU Wind Energy PhD-0067(EN)

May 2017

DTU Wind Energy
Department of Wind Energy

Authors: Kaya Onur Dag
Title: Combined pseudo-spectral / actuator line model for wind turbine applications
Department: Fluid Mechanics Section

DTU Wind Energy PhD-0067(EN)
May 2017

Education:
PhD

Supervisors:
Jens Nørkær Sørensen
Niels N. Sørensen
Wen Zhong Shen

Technical University of Denmark
Department of Wind Energy
Nils Koppels Allé
Building 403
2800 Kgs. Lyngby
Denmark
Telephone

www.vindenergi.dtu.dk

Combined pseudo-spectral/actuator line model for wind turbine applications

by

Kaya Onur Dag

Department of Wind Energy

Technical University of Denmark

Submitted to the Department of Wind Energy in partial fulfilment of the requirements for the degree of

Doctor of Philosophy

at

The Technical University of Denmark

Jens N. Sørensen, Wen Z. Shen, Niels N. Sørensen

2017

"If you want to find the secrets of the universe,
think in terms of energy, frequency and vibration."

Nikola Tesla

Preface

This thesis is submitted in partial fulfillment of the requirements for the *Doctor of Philosophy* degree from the Technical University of Denmark. The research was conducted during the period from October 2013 to October 2016 at the Department of Wind Energy, Fluid Mechanics Section.

I am grateful to my main supervisor, Jens N. Sørensen for providing me such a free work environment which allowed me to implement my own ideas. Many thanks to my co-supervisors, Wen Zhong Shen and Niels N. Sørensen giving me the necessary support during the development of the code. I shall also thank to Philipp Schlatter, Torben Bilgrav Christiansen and Allan Peter Engsig-Karup for the contributions to the project. In addition, I am also thankful to Peter P. Sullivan for his time and the valuable comments.

Last but not least, I shall thank to my close friend Emre Barlas and my colleagues for the priceless discussions we had, which eventually allowed me to reach this knowledge level.

Kaya Onur Dag
October 2016, Copenhagen

Abstract

This work contains a development of a new large eddy simulation (LES) tool for wind farm computations. One of the main goals of the development part has been to produce a scalable and efficient flow solver using pseudo-spectral discretization. In the first part of the thesis, details of the developed code is presented and verifications are carried out. In the second part, by using the new LES code, a comprehensive investigation is made for the well-known actuator line model (ALM), which is cost-efficient for investigation of the loading estimations on wind turbine blades. In ALM, the body forces are first distributed on a line to represent a blade and then projected to the CFD domain by a smearing function to avoid oscillations in the solver. As a result of the smearing application, the vorticity from the airfoil sections become distributed in 3D space which then causes over estimations of the blade tip loadings. To avoid the effect, researchers either use Prandtl's tip correction, which is conceptually wrong under ALM framework, or employ extremely fine grid resolutions which result is excessive computational load. In this thesis detailed investigation of the issue is made and a correction procedure is introduced to avoid the effect. First an investigation is held for a simple planar wing that is represented with ALM in the CFD domain and the correction is presented in detail. Furthermore, NREL 5MW and Phase VI rotors are used for rotor applications and it is concluded by various validation cases that the new tip correction greatly improves the loading distributions on the blades. Additionally, it is found that by using grid resolutions as coarse as 10 grid points per blade, comparable results can be obtained.

Dansk resumé

Der er udviklet et nyt LES (Large Eddy Simulation) vrktøj til at beregne strømningen i en vindmølle park. En af hovedmålene er at lave skalerbar og effektiv strømnings løser ved brug af pseudo-spektral diskretisering. Raporten starter med en detaljeret gennemgang af den udviklede kode samt verificering. Det nste afsnit beskriver en udførlig undersøgelse af Aktuator linie modellen (ALM) i den nye LES baserede strømningsløser. ALM er en kost effektiv metode til at estimere laster på vindmølle blade, idet de aerodynamiske laster ligger langs en linje omkring bladet og smurt ud ved brug af en normalfordeling for endelig at blive interpoleret til de omkringliggende celler i beregningsnettet. Pga. af glatningen af lasterne bliver vorticitien smurt så meget ud at det medfører en overestimering af de aerodynamiske laster ved tippen. For at undgå dette har der tidligere vret anvendt en Prandtl tip tabs korrektion, hvilket er fysisk forkert da den hidrører fra at lasterne er fordelt over en skive og ikke langs linjer. Man kan i stedet anvende et meget fint beregningsnet, men på bekostning af beregningstid. I dette PhD projekt er problemet udførligt undersøgt og en procedure er beskrevet hvordan den uønskede effekt af udglatningen af lasterne kan undgås uden at skulle anvende et meget fint beregningsnet. Metoden er først verificeret på en plan og ikke roterende vinge, og dernst på NREL 5MW og Phase VI rotoren, hvor der er vist at den ny tip korrektion giver en betydelig forbedret radial lastfordeling. Der er også vist, at metoden giver gode resultater, selv for en grov opløsning på omkring 10 punkter per blad.

Contents

Chapter 1

Introduction

With growing wind turbine rotor diameters and giga-watt scale wind farms, high-fidelity simulations of turbine wake and atmospheric boundary layer (ABL) interactions are gaining interest among researchers. The key to decrease the cost of energy from wind turbines is to lower the uncertainties that occur both in turbine design and wind farm siting processes. From the developer's perspective, with the increased number of turbines, wake recovery has become the most important parameter in the energy extraction mechanism from the ABL. Thus, for larger wind farms, since more turbines operate in the wake of an upstream turbine, the estimated power production is increasingly dependent on the accuracy of the wake model. Furthermore, from the manufacturers point of view, the installed turbines in various turbulent conditions are expected to withstand the occurring fatigue loads throughout the design lifetime. Thus, to be able to push the structural limits and decrease the cost of energy, the production of larger rotors will require accurate estimation of life-time load levels which requires detailed flow conditions of the installation site.

Solving the Navier-Stokes equations to provide the necessary flow information is extremely costly for many test cases. Due to their simplicity and low computational cost, basic wake models (such as Jensen (1983)) are often employed in wind farm siting. These basic models have been proven to accurately estimate velocity deficits on average Peña *et al.* (2015). However, they are limited in terms of providing information about the unsteady effects and the resultant turbine loads. As a result, more sophisticated wake models which allow one to mimic the turbulence together with both added fluctuations from rotors and the wake deficit, (i.e. Dynamic Wake Meandering model, see Larsen *et al.* (2007)) are employed for aero-servo-elastic simulations to estimate life-time fatigue under specified conditions. To be able to further develop these models and also increase their accuracy for specific cases, it is necessary to employ CFD solvers which can simulate the desired atmospheric conditions of turbines and provide higher fidelity information directly from the governing physics equations.

1.1 Overview of different CFD techniques

There are various methods which can be applied to time march with the Navier-Stokes equations. These methods are selected by the user depending on the application type, availability of CFD software and computing power. For wind farm ABL studies, we can divide major choices into three groups: turbulence modeling, spatial discretization and wind turbine representation.

1.1.1 Turbulence modeling

With today's computing power, it is not possible to conduct a direct numerical simulation (DNS) of the ABL due to the number of grid points required to capture the smallest turbulence scales. However, by the usage of turbulence models, we can reach averaged solutions with Reynolds averaged Navier-Stokes (RANS) or large eddy simulation (LES) modeling approaches. In both RANS and LES, the common method is to model the shear effects of unresolved turbulence structures and re-introduce them into the momentum equations as an artificial viscosity, which does not require grid sizes in the order of the smallest turbulent scales in ABL. The conceptual difference in these two models is that, RANS computations return to an ensemble averaged flow field, which is steady, whereas LES is an unsteady technique in which a spatial filter is applied to the Navier-Stokes equations so that the energy containing large scales are resolved and the effect of the small scales are modeled. In comparison with RANS, LES computations are rather costly and so require massive parallelizations and high performance computing (HPC) clusters. Furthermore, to avoid the cost of LES, but at the same time obtain unsteady information, in some cases RANS is applied in an unsteady manner (uRANS), where the time scale of the averaged motion and the turbulence structures are separated in order to capture unsteady behavior. Although it can be argued to represent uRANS and LES in the same wavenumber space, in Fig. 1.1 an illustration of the resolved and modeled scales is made for interpretation purposes.

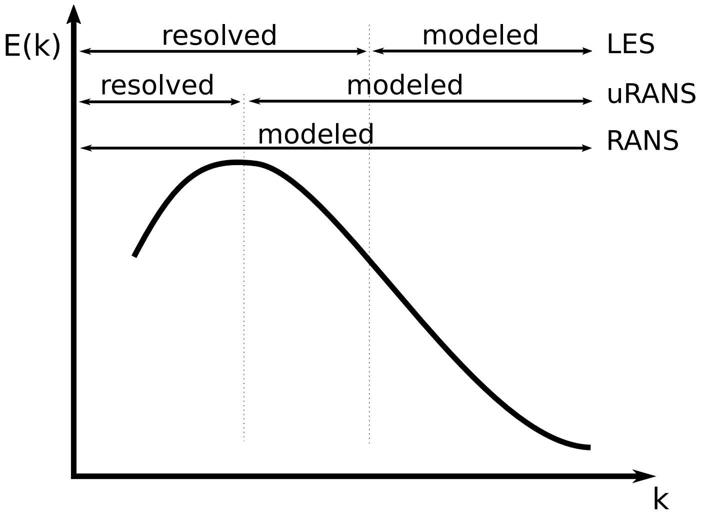

Figure 1.1: Illustration of the resolved scales for RANS and LES

In wind turbine ABL applications, RANS is preferred for industrial purposes due to the smaller computational cost. However, as noted in various studies RANS results show considerable variation depending on the turbulence closure model used (see i.e. Simisiroglou *et al.* (2016)), and they do not provide unsteady information. Thus, in order to obtain unsteady information with fine temporal resolutions, LES computations are needed.

1.1.2 Spatial discretization

There are different types of CFD discretization techniques that can be employed to resolve the equations in discrete space. The most common types can be listed as finite volume (FV), finite difference (FD), finite elements (FE) and spectral methods (SM). Although all of these types eventually solve the same equations, there are conceptual differences between them which require special attention of the user. Both FD and FV methods use discrete approximations to the field values at given points whereas FE and SM use a polynomial basis. Furthermore, unlike the others, the FV method solves the equations for a given cell rather than a node point, which is physically preferred in some cases. As equations are solved on control volumes, and momentum fluxes are taken at the faces, conservation properties are obtained at cell level.

The SM are often preferred for the cases where high accuracy and energy conservation properties are needed. Due to the efficient FFT (fast-fourier-transform) algorithms Fourier series are often employed in boundary layer LES codes (Akbar *et al.* (2016); Calaf *et al.* (2010); Moeng (1984); Stevens *et al.* (2014)). In addition, for isotropic turbulence studies the usage of Galerkin-Fourier approximation is also very beneficial. In wavenumber space, pressure equation becomes a simple multiplication (see Canuto *et al.* (2007) c3.3,p.99). This not only allows pressure equation to be solved directly and achieves divergence-free at a machine accuracy level, but also decreases the cost of the pressure equation which is commonly considered as the bottle neck of the CFD solvers.

1.1.3 Wind turbine representation

In CFD computations, wind turbine rotors can be represented in various ways in the domain. The first, and perhaps the most obvious one is to resolve the rotor geometry using body-conformal meshes. However, in order to capture accurate blade surface pressure distribution in a fully resolved (FR) LES case, a very fine grid resolution around the blades is required.

To over come the problem, actuator methods such as the actuator disk method (ADM), the actuator line method (ALM) or the actuator surface method (ASM) can be employed. By using actuator methods, turbine rotors can be represented in the CFD domain by means of distributed body forces, which are obtained by a blade-element approach. With the ADM, the forces are distributed on the surface of a disk where a porous disk is introduced and a tip correction is employed to account for the finite number of blades (see Sørensen & Kock (1995)). In recent years, the model has been implemented in LES codes and is used by many researchers for wind farm-ABL computations and validated under various flow cases (Mikkelsen (2003); Réthoré *et al.* (2014); Akbar *et al.* (2016)). With the ALM, instead of representing the turbine as a porous disk, the forces are obtained from individual lines which represent blades, and projected to the CFD domain (Sørensen & Shen (2002)). This methodology allows one to capture the tip vortices as well as individual unsteady loading changes due to local flow variations around the blades. Furthermore, to avoid the limitations of line-loadings, the ASM was developed. In this method, the forces are distributed on the blade surface by considering the pressure distributions that would occur on airfoils (Shen *et al.*

(2009)). In the work of Troldborg *et al.* (2015), ADM, ALM and FR wind turbine rotor representations are compared and has been concluded that with turbulent inflow, wake characteristics predicted by these three methods are in good agreement.

1.2 Contribution of this thesis

This thesis contributes to the numerical simulations of wind farms research in two main parts. In the first part, a new CFD solver is coded from scratch, parallelized and validated. In the second, research is focused on ALM, where a new technique is developed to improve the ALM results. Motivations for this work are stated in the following sections.

1.2.1 Development a new pseudo-spectral solver

DTU Wind Energy Department inholds the EllipSys3D multi-block finite-volume solver Michelsen (1992); Sørensen (1995) which is extensively used for wind turbine research by the department. However, using a pseudo-spectral solver instead of a finite-volume code can be advantageous in some cases due to the energy conservation and high-resolution characteristics of the spectral discretization. To gain further knowledge of pseudo-spectral solvers, examine their efficiency and be able to compare against EllipSys3D, it was decided to develop a new pseudo-spectral solver with this project.

To show the advantage of a spectral representation a simple 1D test case is presented here with different spatial schemes, and the resulting field values and energy properties are compared. An advection-diffusion equation,

$$\frac{\partial u}{\partial t} + u\frac{\partial u}{\partial x} = \nu\frac{\partial^2 u}{\partial x^2}, \tag{1.1}$$

is employed with a diffusion coefficient of $\nu = 0.01$. The velocity initialization is made by

$$u(x) = sin(x/2)^{10}, \qquad x \in [0, 2\pi), \tag{1.2}$$

and periodic boundary conditions are used. The schemes compared in this test are the second-order central difference scheme (*CD2*), forth-order central difference combined with a quadratic interpolation (*QUICK*), and a *Fourier* approximation. In addition, to avoid aliasing errors in spectral space from the non-linear product, a dealiasing operation is applied to the non-linear term in the Fourier case which is then represented with *Fourier**. For each case, number of grid points of $N = 24, 32, 48, 96$ are used together with a time step of $\Delta t = 5 \times 10^{-4}$ s with an explicit Euler time integration scheme. Additionally, a dealiased Fourier method with $N = 2048$ is employed to obtain a reference solution which is then considered as 'exact' for this purpose. In Fig.1.2, the resulting velocity fields at $t = 3$s and total energy change in time relative to the exact solution are compared.

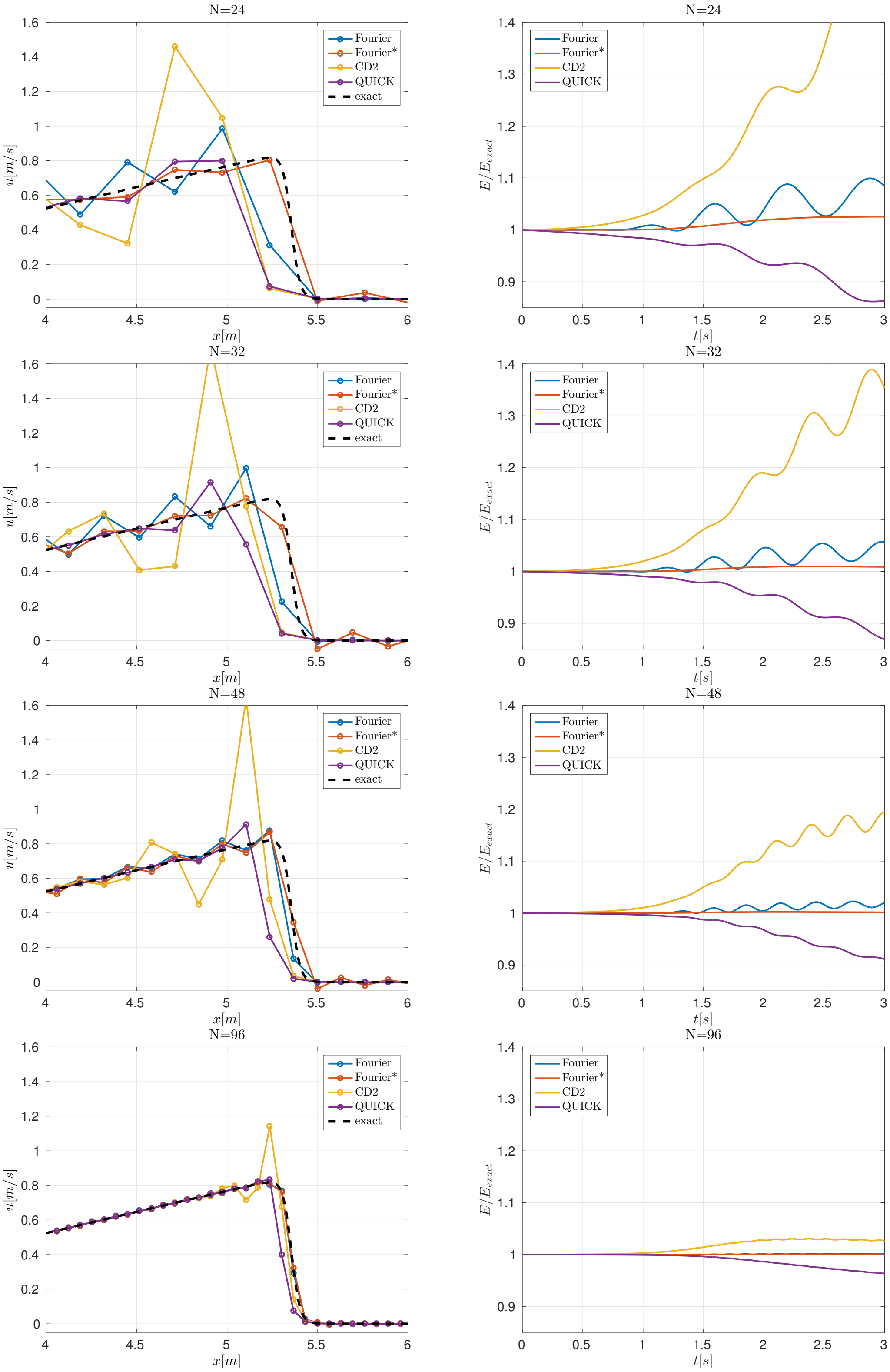

Figure 1.2: Comparison of velocity profiles at $t = 3$ s (left), and relative energy change in time(right) from different discretization schemes with varying grid resolutions.

In the coarsest case, only dealiased Fourier could capture the position of the maximum velocity. With the same resolution, both aliased Fourier and CD2 overestimate the energy in the system, whereas the QUICK scheme shows more dissipation. Also, the dealiased Fourier results with a slight overestimate of the energy. By increasing the grid resolution, all of schemes converge towards the exact solution both in the velocity field and total energy change plots. However, even with the $N = 96$ case, the QUICK scheme over-dissipates and CD2 still shows a slight overestimation of the total energy, which is comparable to the overestimation seen with the dealiased Fourier with $N = 24$. It is easy to conclude from this simple test case that the Fourier series is advantageous relative to the finite-difference schemes with identical resolution settings.

For ABL-wind farm simulations, the downside of using the Fourier series is that the approximation requires periodicity in the domain, which is not the case due to the existence of wind turbine wakes. To overcome this, a special procedure at the end of the physical domain is required, which introduces additional computing cost. In this application, ground parallel axes are treated with the Fourier series with a special treatment at the outlet domain, which is detailed in chapter II. Whereas for the vertical axis, due to the existence of the ground, it is not possible to mimic the periodicity thus the Fourier series can not be used in the same way.

Therefore, finite difference schemes are often the default choice for the vertical axis. To achieve high resolution characteristics as in ground parallel axes with the Fourier series, compact finite difference schemes could be considered in the vertical. In Lele (1992), the resolution characteristics of these schemes are presented and, as noted, they are superior against explicit FD schemes. However, it is mentioned in Morinishi *et al.* (1998) that conservation properties of the high-order schemes may cause instabilities in low-dissipation codes for high-Reynolds flows. Thus, in our implementation a second-order central finite-difference scheme is employed on the vertical axis.

1.2.2 Improvement of the ALM

Although the methodology of ALM is rather straight forward, some complications arise due to the numerics. As mentioned before, actuator methods require a volume force projection which in the ALM case project the line forces onto the CFD domain and smooth out the singularity that is added in order to avoid oscillations. The projection function is often a 3D Gaussian with a width ϵ, which is a variable parameter. In various studies, the effect of the projection width is reported. Troldborg (2008) suggested that fixing the size of the projection width as twice the grid resolution ($\epsilon = 2\Delta$) is a good balance between avoiding oscillations and accurately predicting the blade loadings. In the application of Jha *et al.* (2013), they reported that $\epsilon = 2\Delta$ required a blended dissipative scheme to avoid oscillations. In both of these works, a 10% blend of dissipative finite difference schemes were used together with 90% central schemes. On these grounds, it would not be incorrect to mention that $\epsilon = 2\Delta$ would produce oscillations in a spectral code, considering its energy conservation properties. Furthermore, Jha *et al.* (2013) also reported that a constant ϵ parameter causes blade tip loadings to be over-predicted. Physically, projection width can be thought of as a parameter that represents the thickness of the blade and thus should be linked to the chord length of the corresponding section. In the work by Shives & Crawford (2013), the requirement for ϵ and grid resolution is investigated with a wing and concluded that the projection width should be in the order of $\epsilon = 1/4c$, with c being the chord length, and the ϵ value should equal or be larger than the 4Δ. However, this criteria requires a much finer grid resolution than the resolutions that are currently being applied on ALM simulations. In addition, Jha *et al.* (2014) introduced a new methodology to vary the projection width throughout the span of the turbine blade in order to achieve better loading distributions around the tip without using a very fine CFD resolution around the blades. Although their methodology seems to be the most effective in loading estimates with *coarse* grids, their application does not solve the actual cause of the problem and requires case specific tuning.

ALM is designed to avoid the burden of using body-conformal meshes, and still be able to provide accurate information to/from individual blades of the wind turbine. However, these studies show that the method produces grid-resolution-dependent results. In ABL computations, researchers often select a grid size based on the size of the smalles scales that are of interest. However, ALM places a constraint on this which adds unnecessary computational cost. The issue is investigated in detail in this thesis and a new correction has been technique is developed with the goal of producing grid-independent results.

1.3 Current trend in HPC units

In the development section of this thesis, the trend in current HPC units is also taken into consideration. As noted in Slotnick *et al.* (2014), it is currently difficult to predict the future route of the HPC hardware due to an expected paradigm shift in the technology. However, recent trends give a clue to the near future for the computing units that are relied in HPC platforms. As shown in Fig. 1.3, in the last decade, single core performance has hit a barrier and clock speeds have remained steady. Further, as the transistor count has increased, the number of cores per socket has also increased. For the near future, it would be reasonable to assume the same trend to continue with more energy efficient units as well as increased heterogeneous hardware architectures in HPC facilities.

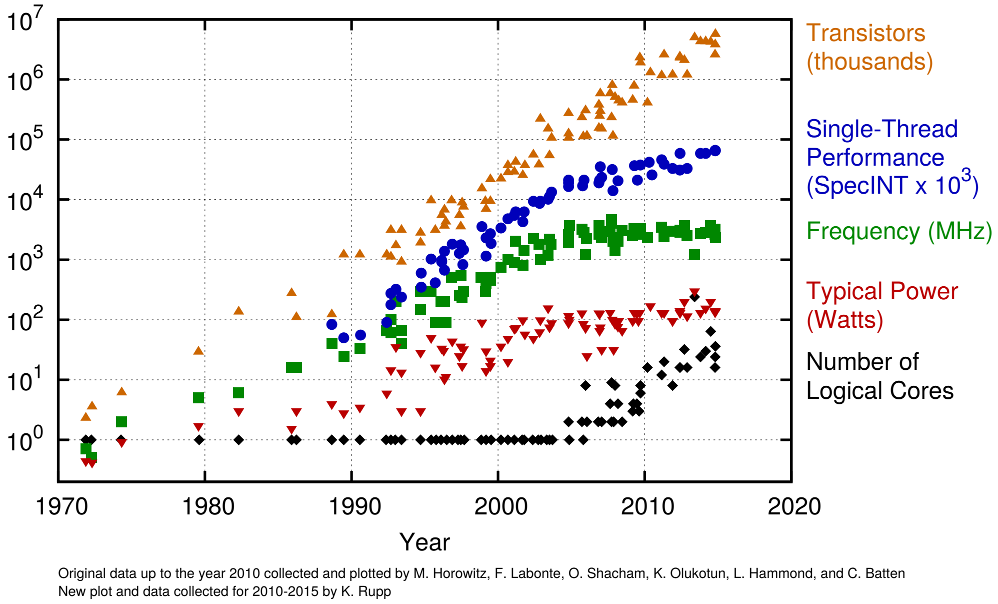

Original data up to the year 2010 collected and plotted by M. Horowitz, F. Labonte, O. Shacham, K. Olukotun, L. Hammond, and C. Batten
New plot and data collected for 2010-2015 by K. Rupp

Figure 1.3: 40 years of microprocessor trend data

As there is a tendency for an increased number of cores per socket, new CFD software developments are expected to exploit this by using parallelization algorithms that take into account the communication speed differences in the hardware. Furthermore, with the addition of many-core hardwares, parts of the computation can be partially outsourced to these many-core accelerators in heterogeneous HPC units. In the current application, parallelization of the new solver is made in two stages which allows the user to take advantage of the rapid in-socket communication.

1.4 Outline of the thesis

In this thesis, first a new pseudo-spectral Navier-Stokes solver is developed. Details are presented in chapter II, and verification of the code with different simulation cases are shown. In chapter III, the issues with ALM are further discussed and a correction strategy to avoid the overestimation of the tip loadings is introduced. The results are validated by a wing application in uniform inflow LES cases compared with lifting line computations. In chapter IV, the introduced correction is first evaluated under different conditions to investigate the dependencies (i.e. varying grid spacing). Furthermore, a rotor implementation of the correction is made and results are presented for NREL 5MW and Phase VI turbines, in both uniform and turbulent inflow conditions. Discussion, conclusions and future developments are explored in the final chapter.

Chapter 2

Development of a Pseudo-spectral Flow Solver

In this chapter the development of a highly scalable pseudo-spectral CFD solver is explained in detail. First, the DNS solver is presented where the temporal and spatial discretizations are explained in detail. Then additional models needed to perform wind farm applications are introduced and their implementations in the core solver is presented.

2.1 Governing Equations

The motion of the fluid is represented by Navier-Stokes equations. In cartesian coordinates, with primitive variables, the incompressible form of the equations can be written as

$$\frac{\partial u_i}{\partial t} = -\frac{\partial (u_i u_j)}{\partial x_j} - \frac{1}{\rho}\frac{\partial p}{\partial x_i} + \nu \frac{\partial^2 u_i}{\partial x_j} \tag{2.1}$$

$$\frac{\partial u_i}{\partial x_i} = 0 \tag{2.2}$$

which are the momentum and the continuity equations respectively. $u_i (i = 1, 2, 3)$ are the velocity components corresponding to u, v and w in the coordinate system of horizontal streamwise $x_1 = x$ direction, lateral $x_2 = y$ direction and vertical $x_3 = z$ direction. In momentum equations, the first term on the right hand side represents the convection, second is the pressure gradient, and the last term is the molecular diffusion.

In this system of equations, there are four unknowns which are the three velocity components and the pressure variable with four given equations. However, the last equation, the continuity, does not include a pressure variable inside, therefore a connection is needed between the continuity equation and the pressure variable. For this purpose, one can enforce a divergence free constraint from continuity equation on the momentum equations and derive a pressure equation, where pressure becomes a dummy variable to enforce the continuity.

Assuming that the initial condition of the velocity field is divergence free, it is required to have $\frac{\partial u_i}{\partial t}$ to also be divergence free in order to satisfy the continuity in the next time step.

$$\frac{\partial}{\partial x_i}\left(\frac{\partial u_i}{\partial t}\right) = 0 \tag{2.3}$$

By replacing $\frac{\partial u_i}{\partial t}$ with the right-hand-side (RHS) of the momentum equations as

$$\frac{\partial}{\partial x_i}\left(-C - \frac{\partial p}{\partial x_i} + D\right) = 0, \tag{2.4}$$

and isolating the pressure term, and equation for the pressure is obtained (see Ferziger & Perić (2002) Sec.7.3.3).

$$\frac{\partial}{\partial x_i}\left(\frac{\partial p}{\partial x_i}\right) = \frac{\partial}{\partial x_i}(-C + D) \tag{2.5}$$

Here, the C and D terms represent the convective and the diffusive parts respectively. By introducing a time stepping scheme such as explicit Euler and de-coupling the pressure from the system with an introduction of an intermediate time step, time step can be divided into two parts as

$$\begin{aligned} u_i^* &= \Delta t(-C_i^n + D_i^n) + u_i^n, \\ u_i^{n+1} &= u_i^* - \Delta t(\nabla p^{n+1}), \end{aligned} \tag{2.6}$$

where the upper index n represents the current time, $*$ is an intermediate step and $n+1$ is the next time step and Δt is the time step size. The intermediate velocity, u_i^*, does not satisfy the continuity equation and requires a pressure field that would project the flow field to a divergence free flow field. To obtain this pressure, Eq. 2.5 can be solved on the discrete form as

$$\Delta p^{n+1} = \frac{1}{\Delta t}\nabla \cdot [\Delta t(-C_i^n + D_i^n)]. \tag{2.7}$$

It must be noted that, in Eq. 2.7 the Laplace sign represents a divergence of a gradient operator, which must be treated in the correct order in the computation. Although in continuous space these two operators commit and product is a Laplace operator, this is not the case in a discrete sense and the violation of this operator causes a divergence field.

This methodology is referred as the *fractional-step method* (Armfield & Street (2002); Canuto *et al.* (2007) Sect 7.2) where the main idea behind is simply to split velocity and the dummy pressure with a loose coupling.

2.2 Temporal discretization

It is common to treat different parts of the momentum equation with various temporal schemes (see Canuto *et al.* (2007) Sect 7.2). To avoid stability problems at low Reynolds numbers, there is a need to treat diffusive terms with an implicit method. On the other hand, non-linear convective terms are often treated explicitly due to computational complexity, either with a multi-stage method such as an explicit Runge-Kutta (RK) (see Sullivan & Patton (2008); Meyers & Meneveau (2010)) or with an Adams-Bashforth (AB) type multi-step method(see Moeng (1984); Porté-Agel *et al.* (2000)).

Regardless of the order of the used temporal schemes, the dominant temporal error is produced from the fractional-step methodology due to the loose coupling between velocity and pressure. It is known that simple splitting, where the intermediate velocity is calculated without any pressure terms, produces first-order accuracy in time. Nevertheless, as noted in Armfield & Street (2002), with the usage of the pressure from the previous time step, as shown in 2.8, second-order accuracy on velocity is recovered.

$$u_i^* = \Delta t(-C_i^n - \frac{\partial p^n}{\partial x_i} + D_i^n) + u_i^n \tag{2.8}$$

In our code, convective terms are treated with a second order AB method due to its simplicity in computation and a second order Crank-Nicolson (CN) scheme is employed for the diffusive terms. The resulting time discretization for intermediate velocity is shown below.

$$u_i^* = \left[\left(\frac{3}{2} C_i^n - \frac{3}{2} C_i^{n-1} \right) - \frac{\partial p^n}{\partial x_i} + \left(\frac{1}{2} D_i^n + \frac{1}{2} D_i^* \right) + f_i^n \right] \Delta t + u_i^n \tag{2.9}$$

This is similar to the discretization presented in Canuto *et al.* (2007) Sect 7.2 where a second-order backward-differencing-scheme is used to discretize the diffusive terms instead.

The aimed application area of this new CFD code is wind farms and ABL studies where Reynolds numbers are extremely high and molecular diffusion term in momentum equation becomes ineffective. Nonetheless, for completeness the molecular diffusion term is kept inside the code with a switch in the setup file for further cancellation to avoid unnecessary computation costs of the implicit CN scheme.

2.3 Spatial discretization

A velocity domain which is periodic in the $[0, 2\pi)$ interval can be represented with the Fourier series as

$$u^N(x,t) = \sum_{k=-N/2}^{N/2-1} \hat{u}_k(t) e^{ikx}, \tag{2.10}$$

where N represents the number of discrete points used in the axis x, k is the Fourier wavenumber and $\hat{u}_k(t)$ is the amplitude of the k^{th} wave at the time t, which can be obtained by employing an FFT. The main goal of this project was to develop a high order solver that uses spectral discretization in space, which eventually becomes advantageous due to the efficient FFTs available. In atmospheric flows, as mentioned before, ground parallel (streamwise and spanwise) axes are often treated with periodicity thus it is straight forward to use the Fourier series for spatial discretization on these axes. Further, a second order finite difference scheme is employed for the vertical axis due to the ground boundary condition. In addition to the discretization schemes used, the ground parallel velocities (u and v) and pressure points are shifted half a grid point on the vertical axis, which not only becomes practical when applying boundary conditions, but also strongly couples the pressure and the vertical velocity (w) at the point due to the central difference scheme applied. The schematic of the grid is given in Fig. 2.1.

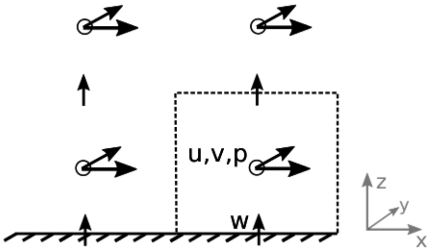

Figure 2.1: Discretization of variables u, v, w, p

Since the diffusion terms are discretized in time with a CN scheme, we can rewrite the Eq.2.9 by applying the discrete derivative operators for the diffusive terms and construct the left-hand-side (LHS) operator of the semi-implicit system as shown below.

$$\left[1-\frac{\nu}{2}\big(-k_x^2-k_y^2+D^2_{z(FD2)}\big)\right]\hat{u}^*_{i(k_x,k_y)} = \left[\left(\frac{3}{2}\hat{C}_i^n-\frac{3}{2}\hat{C}_i^{n-1}\right)_{(k_x,k_y)} - ik_{x_i}\hat{p}^n_{(k_x,k_y)} + \frac{\nu}{2}\big(-k_x^2-k_y^2+D^2_{z(FD2)}\big)\hat{u}^n_{(k_x,k_y)}\right]\Delta t + \hat{u}^n_{(k_x,k_y)} \qquad i=1,2 \quad (2.11)$$

$$\left[1-\frac{\nu}{2}\big(-k_x^2-k_y^2+D^2_{z(FD2)}\big)\right]\hat{u}^*_{i(k_x,k_y)} = \left[\left(\frac{3}{2}\hat{C}_i^n-\frac{3}{2}\hat{C}_i^{n-1}\right)_{(k_x,k_y)} - D_{grad_z}\hat{p}^n_{(k_x,k_y)} + \frac{\nu}{2}\big(-k_x^2-k_y^2+D^2_{z(FD2)}\big)\hat{u}^n_{(k_x,k_y)}\right]\Delta t + \hat{u}^n_{(k_x,k_y)} \qquad i=3 \quad (2.12)$$

Here, $\hat{u}_i$ represents the velocity field transferred to the Fourier space in x and y axes where k_x and k_y are the corresponding wavenumbers and $D^2_{z(FD2)}$ is the second derivative operator from the finite difference scheme, which is a tri-diagonal band matrix for the second order approximation. As shown in Eq.2.12, it should be noted that the pressure term on the right hand side becomes $-D_{grad_z}\hat{p}^n_{(k_x,k_y)}$ for the vertical momentum equation.

From the computational point of view, one of the main advantages of using the Fourier series in two axes is that the three dimensional implicit system for the intermediate velocity, or the pressure equation, can be solved by using individual 1D operations. Since communication is not needed between these 1D operations, computation at this stage can be parallelized without a communication overhead. Specifically, the derivative operations on Fourier axes work on diagonals thus the solution for the equation system becomes a contiguous memory operation with a simple tri-diag matrix solver (so called *TDMA* or *Thomas Algorithm*, see Ferziger & Perić (2002) Sect 5.2.3) that consists of a forward and a backward loop. As an example, LHS matrix of the pressure equation is illustrated in Eq. 2.13.

$$\left[\begin{bmatrix} -k_x^2-k_y^2 & & & \\ & -k_x^2-k_y^2 & & \\ & & -k_x^2-k_y^2 & \\ & & & \cdots \end{bmatrix} + \begin{bmatrix} \frac{-1}{\Delta z} & \frac{1}{\Delta z} & & & \\ & \frac{-1}{\Delta z} & \frac{1}{\Delta z} & & \\ & & \frac{-1}{\Delta z} & \frac{1}{\Delta z} & \\ & & & \ddots & \ddots \end{bmatrix} \begin{bmatrix} 0 & & & \\ \frac{-1}{\Delta z} & \frac{1}{\Delta z} & & \\ & \frac{-1}{\Delta z} & \frac{1}{\Delta z} & \\ & & \ddots & \ddots \end{bmatrix} \right] \tag{2.13}$$

As seen above, for each Fourier amplitude the equation system ties the variables only in the vertical axis. In this way the pressure equation Eq. 2.7 can be solved for every Fourier mode separately.

The RHS of the pressure equation is the divergence of the intermediate velocity field (or the divergence of the velocity update since u^n was already divergence free), whereas the LHS is the divergence of a gradient operation of the unknown pressure field as shown below in Eq.2.14.

$$\Big[(-k_x^2 - k_y^2) + \big(D_{div_z} D_{grad_z}\big)\Big]\hat{p}^{n+1}_{(k_x,k_y)} = \\ \frac{1}{\Delta t}\left(\, ik_x \hat{u}^*_{(k_x,k_y)} ik_y \hat{v}^*_{(k_x,k_y)} + D_{div_z} \hat{w}^*_{(k_x,k_y)}\,\right) \tag{2.14}$$

It should be noted that, the finite difference divergence and gradient operators, D_{div_z} and D_{grad_z}, are cell-centered derivative operations since the pressure grid is half a grid space shifted on the vertical axis (relative to the grid points of the vertical velocity), and these operators are not exactly the same since their input and output grids are different.

2.4 Boundary conditions

For streamwise and spanwise domain boundaries, periodicity (which is the default due to the nature of the Fourier series) is used for both velocities and pressure. For wind farm applications, a fringe technique is employed to avoid farm wakes becoming the inflow conditions. This technique will be explained further.

The top and the bottom boundary conditions are case specific and switched depending on the simulation type. For channel flow DNS simulations, Dirichlet boundary conditions are employed for the velocities at the bottom and the top walls. The application of the boundary condition is enforced on the value for the bottom boundary condition of the wall normal velocity w. However, for the top boundary of w, and the bottom and the top boundary of ground parallel velocities, the values are imposed by stuffing the boundary conditions inside the derivative matrices since there are no grid points available at these locations.

For wall modeled LES channel flow cases, boundary conditions for the wall normal velocity w are kept the same and applied in the same way as in the DNS setup. For ground parallel velocities, Dirichlet conditions are replaced by slip boundary conditions since the walls are modeled with a defined wall shear stress which will be detailed in further. In the case of an open-top simulation, such as a wind farm application, boundary conditions are the same as LES channel flow but without an imposed top wall shear stress. For the pressure field, Neumann condition is used at the bottom and the top boundaries, and periodic conditions are used at the inlet and the outlet for all the mentioned flow cases.

From the user's perspective, to keep things simple, these conditions are switched automatically by switching the flow type in the setup file (where the turbulence and wall models are also switched accordingly).

2.5 Aliasing errors

For Δx grid spacing, the shortest wave length that can be resolved with the Fourier series is $2\Delta x$. However, due to the non-linear interactions in convective terms, wave lengths shorter than $2\Delta x$ appear which become misrepresented in the grid system and lead to aliasing errors. Orszag (1971) showed that by filtering the top one-third of the waves after the operation, which corresponds to wave lengths in between $2\Delta x$ and $3\Delta x$, these contaminated waves could be removed.

The non-linear operation takes place in real space. To avoid aliasing errors, the terms are padded with zeros to a finer grid in Fourier space before the operation takes place. The padded grid is $3/2$ times finer than the actual grid, which returns to the actual grid after a $1/3$ filtering operation. In long simulations, it is observed that accumulated errors due to aliased convective terms led to incorrect results or blew up the simulations due to the accumulated energy at the high wave numbers. Thus, in the latest version of the code, it is hard coded that the non-linear operation in convective terms are always de-aliased. The the non-linear operation takes place as

$$\left(\frac{\partial(\hat{u}_j\hat{u}_i)}{\partial x_j}\right)^p \to \mathcal{F}\left[\frac{\partial}{\partial x_j}\left(\mathcal{F}^{-1}(\hat{u}_j^p)\ \mathcal{F}^{-1}(\hat{u}_i^p)\right)\right],$$

where superscript p represents a 3/2 padded variable in Fourier space and $\mathcal{F}$ and $\mathcal{F}^{-1}$ are Fourier and inverse Fourier transforms respectively. Next, last third of the waves are removed from $\left(\frac{\partial(\hat{u}_j\hat{u}_i)}{\partial x_j}\right)^p$ to obtain a fully dealiased term.

2.6 Turbulence model

In a typical wind farm simulation, Reynolds numbers reach over millions where the difference between the smallest and largest length scale becomes unacceptable for a DNS application due to today's computing capabilities. It is common knowledge that the main part of the energy in the flow is contained in large scale eddies, which is our main interest. However, solving large scale eddies alone would not be enough because the energy dissipation mechanism is around the Kolmogorov length scale (which can be thought as the smallest scale in a turbulent flow), and the meshes used for farm simulations are too coarse to capture these small length scales. To be able to allow our system to resolve large scale eddies alone and be in balance in terms of energy, we have to add a model that absorbs energy at larger scales, by mimicking the energy transfer rate to smaller scales that would have occurred if the grid was fine enough to resolve the smallest scales that the flow would have.

The effect of the small scales is modeled with a turbulence model and the large scale motion, which is resolvable with the employed grid and is simulated by using the filtered momentum equations:

$$\frac{\partial \overline{u_i}}{\partial t} = -\frac{\partial \overline{u_j u_i}}{\partial x_j} - \frac{1}{\rho}\frac{\partial \overline{p}}{\partial x_i} + \nu \frac{\partial^2 \overline{u_i}}{\partial x_j^2}. \tag{2.15}$$

The first filtered product on the right hand side in the Eq. 2.15, is the filtered non-linear convective term. It must be noted that this term is different from ($\overline{u_j}\ \overline{u_i}$) and is not computable because the unfiltered u_i is not a product of the equation system anymore. The difference of these terms is referred as *residual-stress tensor* (Pope (2000) Sect

13.3), which is defined as

$$\tau_{ij} \equiv \overline{u_j u_i} - \overline{u_j}\ \overline{u_i} \tag{2.16}$$

By combining Eq. 2.15 and Eq. 2.16, filtered momentum equations can be reformed with filtered variables as

$$\frac{\partial \bar{u}_i}{\partial t} = -\frac{\partial(\bar{u}_j \bar{u}_i)}{\partial x_j} - \frac{\partial \overline{p}}{\partial x_i} + \nu \frac{\partial^2 \bar{u}_i}{\partial x_j^2} - \frac{\partial \tau_{ij}}{\partial x_j}. \tag{2.17}$$

The deviatoric part of the stress tensor is parameterized as

$$\tau_{ij} - \frac{1}{3}\delta_{ij}\tau_{kk} = -2\nu_{SGS} S_{ij} \tag{2.18}$$

where ν_{SGS} is the eddy viscosity, and S_{ij} is the resolved strain rate tensor, given as

$$S_{ij} = \frac{1}{2}\left(\frac{\partial \bar{u}_i}{\partial x_j} + \frac{\partial \bar{u}_j}{\partial x_i}\right). \tag{2.19}$$

In the current version of the code, Smagorinsky model (Smagorinsky (1963)) is employed to compute eddy viscosity, which is given as

$$\nu_{SGS} = (C_S \Delta)^2 |S|, \tag{2.20}$$

where C_S is the Smagorinsky coefficient, the grid length $\Delta = (\Delta x \Delta y \Delta z)^{\frac{1}{3}}$, and $|S|$ is the characteristic filtered rate of strain defined as

$$|S| = (2 S_{ij} S_{ij})^{\frac{1}{2}}. \tag{2.21}$$

2.7 Wall model

To be able to capture the shear of the wall, one needs to have enough resolution close to the wall to resolve the viscous layer, which plays a key role in capturing and feeding the wall generated shear into the turbulent flow. To achieve this for an ABL flow, the required resolution has to be fine enough that a 10 by 10 grid would fit on the tip of your finest pencil. Considering a domain of tens of kilometers, such a grid is not feasible in the year of 2016. To overcome the problem, wall models are employed which provide a shortcut with some side effects.

Inside the constant stress layer, a logarithmic streamwise velocity profile can be assumed in an averaged manner. With this assumption, u^+, the normalized streamwise velocity, can be defined as

$$u^+ = \frac{\langle U(z) \rangle}{u_\tau} = \frac{1}{\kappa} \log \frac{z u_\tau}{\nu} + B, \tag{2.22}$$

where $\langle U \rangle(z)$ is the averaged velocity at the height z, κ is the von Karman constant, u_τ is the friction velocity defined as $u_\tau = \sqrt{\frac{\langle \tau_w \rangle}{\rho}}$ with $\langle \tau_w \rangle$ being the averaged wall stress, and B is a constant. By rearranging the terms, the system can be iteratively solved for τ_w (Grötzbach (1987), see also Piomelli *et al.* (1989)),

$$\langle \tau_w \rangle = \rho \left(\frac{\langle U \rangle(z) \kappa}{\log(Ey\sqrt{\frac{\tau_w}{\rho}}/\nu)} \right), \tag{2.23}$$

where the constant $E = 9$ ($B \simeq 5.3$) can be used for an hydraulic smooth wall. For rough walls, similar can be obtained by,

$$\langle \tau_w \rangle = \rho \left(\frac{\langle U \rangle(z) \kappa}{\log(\frac{z}{z_0})} \right), \tag{2.24}$$

with z_0 being the roughness height (Townsend (1976) Sect 5.5, Mason & Callen (1986)). In the current version of the code, both of these implementations exist.

As applied by Schumann (1975), from the averaged wall stress, unsteady local stresses can be obtained via

$$\tau_{w,13}(x, y, z = 0) = \frac{\langle \tau_w \rangle}{\langle U \rangle} u(x, y, dz/2), \tag{2.25}$$

and

$$\tau_{w,23}(x, y, z = 0) = \frac{\langle \tau_w \rangle}{\langle U \rangle} v(x, y, dz/2). \tag{2.26}$$

At this stage, local stresses can be fed into the momentum equations and the shear from the wall would be captured.

2.8 Actuator line model

In ALM, the turbine blades are represented as distributed body forces on a line that is assumed to the quarter-chord line of the blade. The illustration is shown in Fig.2.2 (left). To calculate the body forces, airfoil polar data is employed and angle of attack values are used as in the blade-element approach. First, velocities from the flow solver

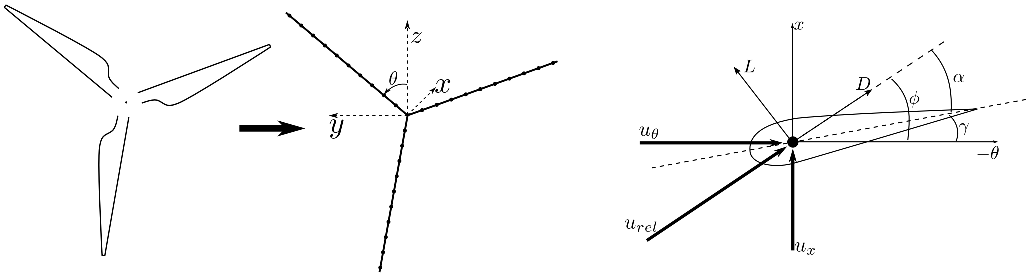

Figure 2.2: Illustration of the actuator line model (left), and local angles of a blade cross-section (right).

are interpolated to velocity values on the actuator line points as $u_{x(N,m)}, u_{y(N,m)}, u_{z(N,m)}$. The N and m represent the blade and actuator line point indices respectively. With known local velocities, the tangential velocity for each actuator line point is calculated by using the rotational speed ω, azimuthal position of the blade θ and the radial position r as

$$u_{\theta(N,m)} = w\ r_{(N,m)} - \big(v_{(N,m)}\ cos(\theta_N) + u_{z(N,m)}\ sin(\theta_N)\big)^{[1]}. \tag{2.27}$$

Then, the flow angle for each actuator line point is obtained as

$$\phi_{(N,m)} = \tan^{-1}(u_{x(N,m)}/u_{\theta(N,m)}), \tag{2.28}$$

which is then used together with the local twist and the pitch angle of the blade (γ) to obtain angle of attack values (α) for each actuator line point

$$\alpha_{(N,m)} = \phi_{(N,m)} - \gamma_{(N,m)}. \tag{2.29}$$

Next, the lift and drag forces for unit span are obtained by

$$f_{L(N,m)} = \frac{1}{2}\ \rho\ u^2_{rel(N,m)}\ c_{(N,m)}\ C_{L(N,m)}, \tag{2.30}$$

$$f_{D(N,m)} = \frac{1}{2}\ \rho\ u^2_{rel(N,m)}\ c_{(N,m)}\ C_{D(N,m)}, \tag{2.31}$$

where $u_{rel} = \sqrt{u_\theta^2 + u_x^2}$ is the relative velocity, c is the chord length and C_L and C_D are the local lift and the drag coefficients. At this stage, these forces are projected to

---

[1] For the sake of simplicity, the rotor plane is assumed to be perpendicular to the flow

tangential and normal components by using the local flow angles as

$$f_{\theta(N,m)} = f_{L(N,m)}\ \sin(\phi_{(N,m)}) - f_{D(N,m)}\ \cos(\phi_{(N,m)}), \tag{2.32}$$

$$f_{n(N,m)} = f_{L(N,m)}\ \cos(\phi_{(N,m)}) + f_{D(N,m)}\ \sin(\phi_{(N,m)}). \tag{2.33}$$

Then in grid coordinates these forces read

$$f_{x(N,m)} = -f_{n(N,m)}, \tag{2.34}$$

$$f_{y(N,m)} = -f_{\theta(N,m)}\ cos(\theta_N), \tag{2.35}$$

$$f_{z(N,m)} = f_{\theta(N,m)}\ sin(\theta_N). \tag{2.36}$$

Applying these forces directly to the closest CFD grid point would produce oscillations, thus a projection procedure is applied by using a 3D Gaussian weighting,

$$\eta_{(N,m,i,j,k)} = \frac{1}{\epsilon^3 \pi^{(3/2)}} exp\left(- \frac{d^2_{(N,m,i,j,k)}}{\epsilon^2} \right), \tag{2.37}$$

with η is the kernel and ϵ-parameter defines the size of this kernel. The distance d is determined individually for each grid-actuator line point couple as

$$d_{(N,m,i,j,k)} = \sqrt{(X_{(i,j,k)} - x_{(N,m)})^2 + (Y_{(i,j,k)} - y_{(N,m)})^2 + (Z_{(i,j,k)} - z_{(N,m)})^2}. \tag{2.38}$$

Here, the capital letters represent the grid coordinates where i, j, k represent the indices in CFD grid. Then with the known kernel, body forces f_b in momentum equations can be determined as

$$f_{b(i,j,k)} = \sum_N \sum_m \eta_{(N,m,i,j,k)} \begin{bmatrix} f_{x(N,m)} \\ f_{y(N,m)} \\ f_{z(N,m)} \end{bmatrix}. \tag{2.39}$$

2.9 Fringe region

As mentioned earlier, periodicity is a requirement for a function to be approximated by the Fourier series. For a wind farm simulation, however, it is not acceptable to have the wake of a wind farm becoming the inflow condition. Thus, a non-periodic inflow-outflow condition is needed. Spalart (1988) developed a way to enforce periodicity by modifying the equations solved, which allows to the recovery of the outflow with a fringe region to the required inflow condition before it reaches to the end of the periodic domain. This illustrated in Fig. 2.3. The flow inside the physical domain is untreated and the outflow from the physical domain is disturbed by a fringe function.

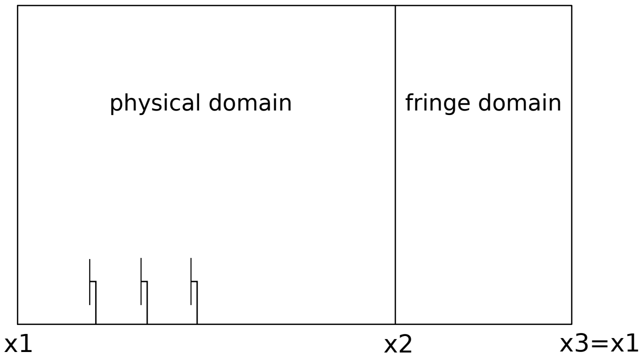

Figure 2.3: Illustration of the fringe region and the physical domain

In the fringe region, an additional forcing term, which is added to the momentum equations, is activated to recover the flow to the desired inflow condition. This additional forcing term is defined as

$$f_{i,fringe}(x, y, z) = \lambda(x)\big(u_{i,req.}(x, y, z) - u_i(x, y, z)\big), \tag{2.40}$$

where λ is the fringe function and $u_{i,req.}$ is the required velocity field. The fringe function λ is defined as

$$\lambda(x) = \lambda_{max}\left[S\left(\frac{x - x1}{d_{rise}}\right) - S\left(\frac{x - x3}{d_{fall}}\right)\right], \tag{2.41}$$

where λ_{max} is the parameter to control the strength of the damping,

$$S(x) = \begin{cases} 0, & \text{if } x \leq 0, \\ 1/[e^{\frac{1}{x-1}+\frac{1}{x}}], & \text{if } 0 < x < 1, \\ 1, & \text{if } x \geq 1, \end{cases} \tag{2.42}$$

and d_{rise}, d_{fall} are the parameters for the width of the increase and decrease regions of the fringe function.

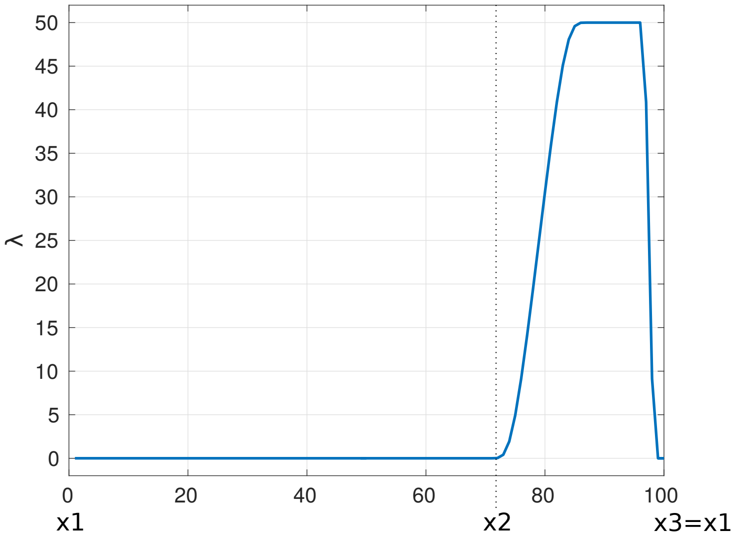

Figure 2.4: Example of the fringe function $\lambda(x)$ with $d_{rise} = 0.6FL$, $d_{fall} = 0.1FL$ and $\lambda_{max} = 50$

An example of fringe function $\lambda(x)$ is shown in Fig. 2.4. In this example the length of the fringe region (FL) is taken as 30% of the stream wise domain length for illustration purposes. In our simulations this value is taken in the order of $10 - 20\%$.

With this technique, $u_{i,req.}$ can be set to a constant value and the outflow will recover to the given velocity which would result in a uniform inflow. One can also prescribe a shear profile on the top of that. However, these would be with 0% turbulence intensity which would be far from reality for a wind farm operating in ABL. To be able to add turbulence, a pre-generated turbulence box can be fed in front of turbines, or a pre-cursor simulation is needed where $u_{i,req.}$ is taken for each grid point in every time step.

2.10 Parallelization

In order to conduct a detailed wind farm simulation where the wakes from the turbines are well resolved, tip vortex sizes, which are in the order of couple of meters, can be taken as the smallest length scale that needed to be captured by the employed grid. Considering an offshore wind farm that consists of 50 turbines, a conservative estimation of the domain size would be 5km × 2km × 500m. With a grid resolution of 2.5m, an equidistant domain would have 640 million grid points which would occupy 256gB of RAM memory for the current code. Although this may fit in a single top-end node, from computation's perspective, it is not feasible to run such a large simulation serially, thus parallelization is necessary.

The main goal here is to develop a parallel code that would run efficiently on the current cluster and at the same time be user/developer friendly. Due to the Fortran knowledge in our department, the coding language was selected to be Fortran 90. Further, to be able to keep parallelization simple to understand, a pure MPI implementation was made. The advantages of having a pure MPI implementation is that the communication routines can be hidden under the hood so that the resulting code becomes easy to understand. Also, having MPI alone gives more freedom, and the domain decomposition for the simulations become more controllable.

For a 1D Fourier transform, all the data has to be in one physical space. Thus it is not possible to divide the grid into cubes which would be the approach for a finite volume code. Instead, the domain is first sliced on the z-axis into parts which are parallel to ground. Next, each slice is divided into slabs on the y-axis. In this form(see the black surface in Fig. 2.5), a Fourier operation could be conducted on the x-axis. This is so called 2D domain decomposition Sullivan & Patton (2008).

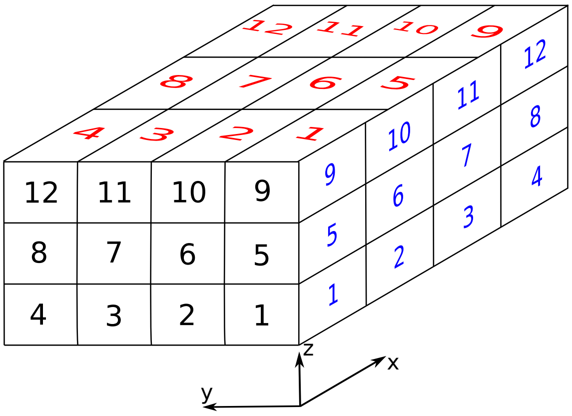

Figure 2.5: 2D domain decomposition and assigned CPU cores

To be able to handle Fourier transforms also on the y-axis, the same decomposition method is applied for the x-z (blue) surface. Further, in order to solve the pressure equation and intermediate velocity in the case of an implicit time stepper, the red decomposition with vertical slabs are used. In total, there are three different types of 2D domain decompositions used throughout a single time step. On these three decompositions, black,blue and red grids allow to loop over i, j and k respectively. As an example, the three slabs that CPU core number 1 would be assigned to handle are illustrated in Fig. 2.6.

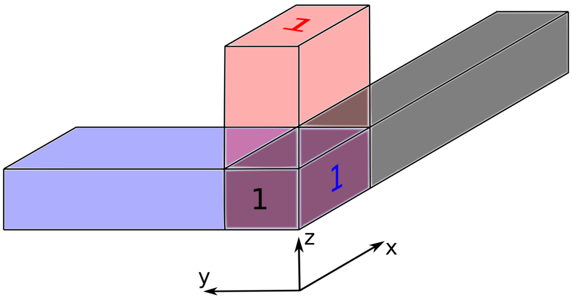

Figure 2.6: Domain parts that CPU-1 computes

Obviously, this system requires many all-to-all MPI communication calls which turns out to be the bottle neck of the scalability of the code.

At the time this code is developed, there are two clusters available namely *Gorm* and *Jess*. Both of these clusters have cc-Numa architecture where in *Gorm* each socket has 6 cores and each node has 2 sockets with 960 cores in total. *Jess* cluster consists of 10-core sockets and each node has 2 sockets with a total 20 cores per node with 6400 cores in total. To exploit the fact that the communication between neighboring cores inside a socket is faster than node to node communication, the adjacent cpu cores are forced to be in the same ground parallel slice in domain decomposition. Through a time step, the all-to-all communications in between black and blue grids are approximately 3 to 6 times more demanding than ones towards red grid due to the Fourier transforms and dealiased non-linear products. Thus keeping black-blue communication in a single socket or in a single node is an advantage that allows user to avoid using the relatively slower network connection in between nodes for the loaded all-to-all communication. To make these decompositions possible, the code uses an internal MPI mapper that forces the CPU cores to be assigned with the domains in a way that demanding data transfers happen as locally[1] as possible.

In the application, an MPI map and communicators are constructed and assigned with respect to required decomposition at the setup stage before the time steps start. These communicators were designed to reshape the arrays on the fly with respect to the destination slab color so that the most looped index is always positioned to be the fastest in memory space. In addition, the communicators used in the core solver[2] employ only non-blocking MPI calls which, in theory, overlaps the computation and communication to some extent.

2.10.1 Memory management

The parallel code uses a dynamic memory allocation system. Although this was not mandatory for our interests, it was implemented to be conservative on local memory consumption in nodes for further applications. There are contiguous physical memory spaces which are allocated at the initialization stage in each node. Before time steps start, pointers of different arrays get assigned to these physical memory spaces, which are then occupied by different arrays at different stages of the time step. Thus, it is not always possible to have every variable available at any given stage in a time step, yet this system allows the consumption of less memory which could be of interest in future GPU applications. Currently, an LES simulation consumes roughly $50\times(NxNyNz)\times 8Bytes$, which is approximately 400mBytes of memory per each million grid points. Further, to be able to keep things modular, the additional models used on the top of the core solver allocate their own memory in modules thus the memory space is isolated from the space that the core solver uses.

2.10.2 Scaling of the code

A DNS case was selected to check the scalability of the code. With two different grid settings, the code was run for approximately 100 time steps by using different number of nodes. Relative speedup based on a single node performance is obtained for different number of nodes and plotted in Fig. 2.7 and Fig. 2.8 for the *Gorm* and *Jess* clusters respectively. In *Gorm* cluster, by using 48 nodes ($\times 12cores$), it takes on average $0.058s$. and $0.45s$. per time step for $8.8m$ and $70m$ grid points respectively. In *Jess* cluster, by using 50 nodes ($\times 20cores$), in average it takes $0.036s$. and $0.27s$. per time step for $9.6m$

---

[1] if possible socket level, else node level

[2] LES solver incl. the SGS model

and $76m$ grid points respectively. In these two clusters, both the clock speed of the cores and avaliable cache size per core are similar. Thus, the performance of the code in two different enviroments are also similar. Nevertheless, due to the better network connection and less inter-node communication requirement per core in the *Jess* cluster, it is expected to have better scaling performance for the same number of cores in this environment.

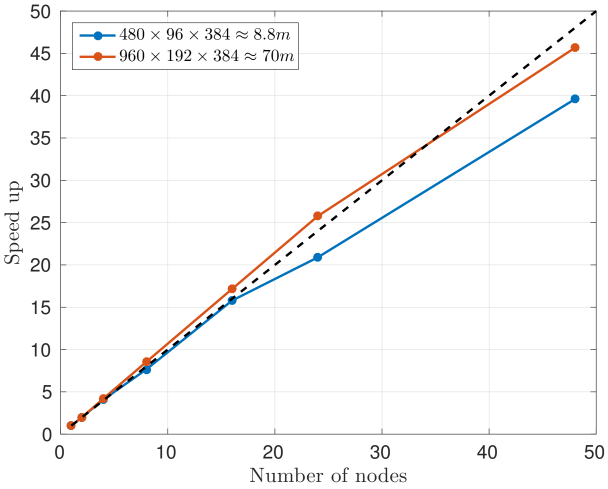

Figure 2.7: Speedup vs. number of nodes - Gorm cluster

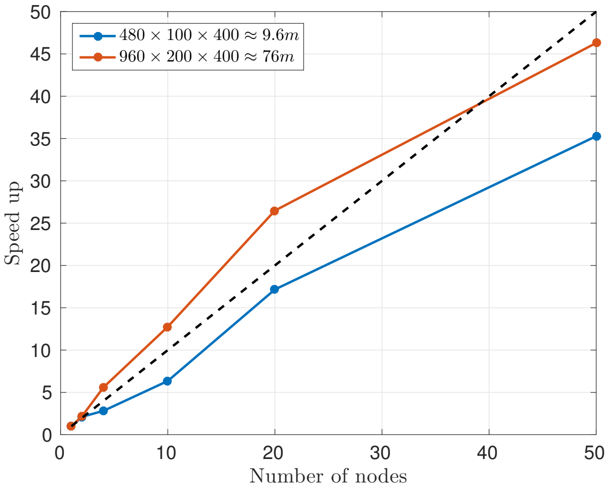

Figure 2.8: Speedup vs. number of nodes - Jess cluster

2.11 On-the-fly pre-cursor simulation

Feeding a random turbulence box in front of a wind turbine is scientifically questionable where the added turbulence may not be in balance with the actual production, nor could fully represent a boundary layer produced turbulence. Also, for a fringe length of 10%, a snapshot of 10% of the precursor 3D velocity domain is needed at every time step. Referring to the previous example with 640 million grid points, this would correspond to 64 million grid points of u,v,w velocity fields. Assuming that the velocity is 8m/s and CFL is fixed at 0.1 with grid resolution of 2.5m, Δt becomes 0.03125, which results in over 100,000 time steps for an hour of simulation time. For such a simulation to be fed by a saved pre-cursor domain snapshots, over 150tB of data storage is needed. Further, different roughness or wind speed simulations would require case specific pre-cursor simulations. Thus, in the current development it was decided to implement an on-the-fly pre-cursor simulation capability to feed the domain of interest via the fringe region. A similar application is presented in Stevens *et al.* (2014).

This additional solver works synchronously with the actual simulation, yet wind turbines and fringe region are removed in the pre-cursor simulation. By turning on the corresponding flag inside the user file, pre-cursor simulation can be switched on to feed the fringe region of the domain of interest on-the-fly at every time step. This methods allows us to avoid massive data storage and also I/O write/read calls to hard drives, which are more time consuming than a memory copy operation over the network memory.

In addition, to avoid network overhead in every time step, the CPUs assigned to execute the pre-cursor simulation are automatically forced via the MPI mapper that the adjacent CPU cores operate on the same decomposed domain piece. This approach allows faster communications from pre-cursor domain to domain of interest due to usage of the local communicators.

2.12 Verification

To verify the implementations in the core solver, a fully turbulent channel flow database by Moser *et al.* (1999) is used. In the new code, grid stretching is not used, which is out of interest in ABL simulations. Thus, to avoid excessive computations, a lower Reynolds number $Re_\tau := u^* h/\nu = 180$ (u^* is the friction velocity, h is the channel half height) is used. In our setup a domain size of $2\pi \times \pi \times 2$, which is the same as the database, and resolutions of $96 \times 48 \times 60$ ($\delta y+ = 5.6$) and $96 \times 48 \times 120$ ($\delta y+ = 3$) are used. The time step sizes used for our simulations correspond to $CFL = 0.1$.

Initialization of the velocity field is made with a streamwise velocity field that varies only on the vertical axis with a *sine* function. To start with a divergent free field, the rest of the velocities are initialized with zeros. Further, since an AB2 time step would require initialization of the convective terms from the previous time step, an explicit Euler time discretization is employed for the very first time step on convective terms.

Initially, a P-controlled pressure gradient is used to drive the flow and the bulk velocity is kept constant. Additionally, a random force field is employed for the first 100 time steps to trigger the turbulence. At the stage where the turbulence was fully developed, the pressure gradient is fixed to a constant value and mean profiles are recorded. To obtain a mean profile, spatial average on streamwise velocity is taken, which is then averaged over time.

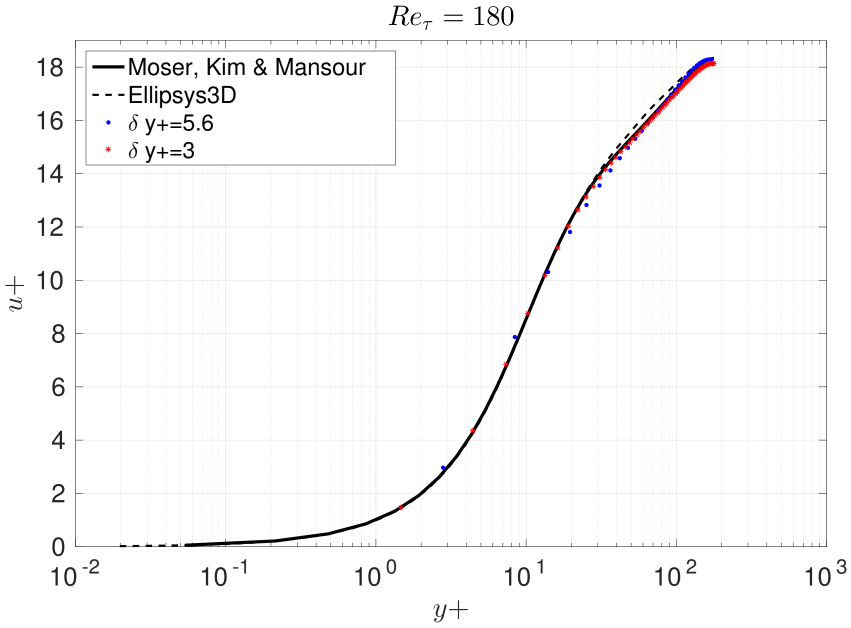

Figure 2.9: Mean velocity profile of the DNS test case at $Re_\tau = 180$

The mean velocity profiles of the simulations from the new code, database and an in-house finite volume code Ellipsys3D are shown in Fig. 2.9. Further, the mean stresses and the fluctuations are plotted against the database in Fig. 2.10 and Fig. 2.11.

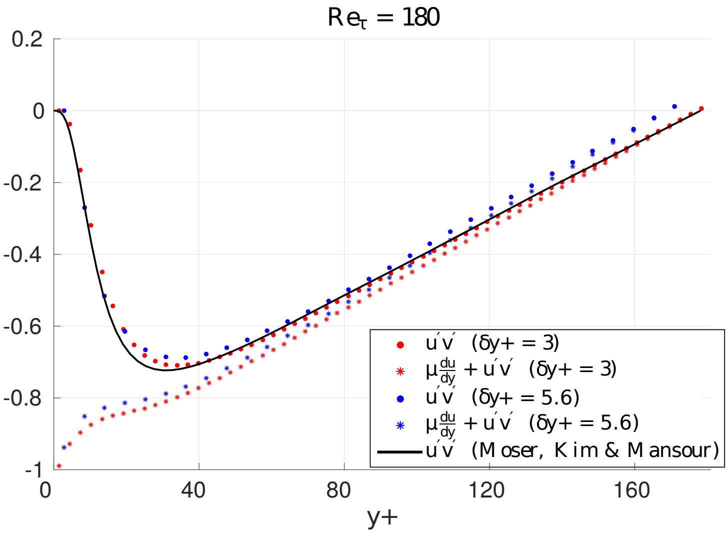

Figure 2.10: Mean shear profile of the DNS test case at $Re_\tau = 180$

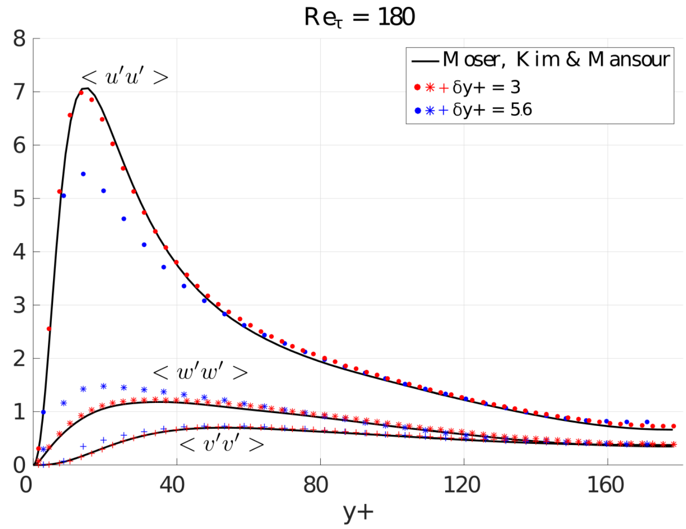

Figure 2.11: Mean fluctuation profiles of the DNS test case at $Re_\tau = 180$

The results indicate that the finer grid case, where the first grid point was located at $y+ = 1.5$, performs well. It can also be concluded that this resolution $(96 \times 48 \times 120)$

is the limit for such a case that a coarser setup (such as $\delta y+ = 5.6$ grid setup) does not represent fluctuations well enough, which then causes the mean shear profile to diverge and also affects the mean velocity.

Before verifying the implementation of the wind turbine model, the turbulence and the wall models are tested with a channel flow case at a higher Reynolds number. With the both models switched on, a turbulent channel flow simulation is conducted with a coarse resolution of $48 \times 24 \times 30$ which corresponds to $\delta y+ \approx 60$. The mean streamwise velocity values obtained with different Smagorinsky coefficients are plotted against a DNS benchmark from del Alamo *et al.* (2004). The DNS data is captured at $Re_\tau = 944$ and our LES simulations are performed at $Re_\tau = 1000$.

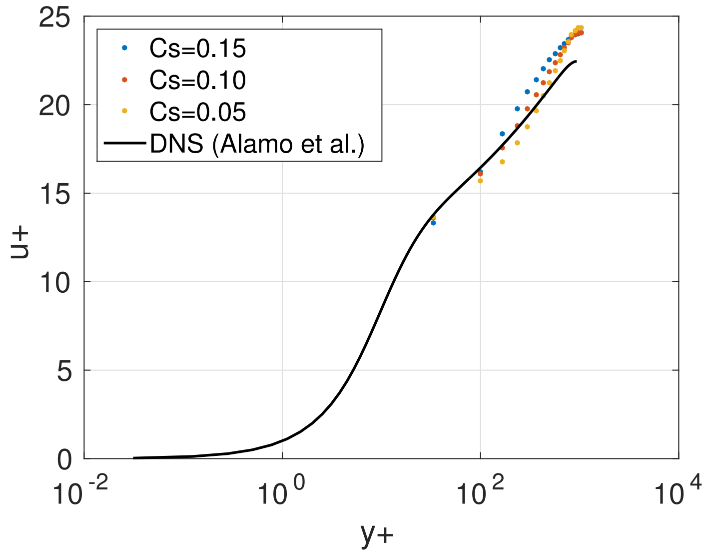

Figure 2.12: Comparison of mean streamwise velocity profile with varying Smagorinsky coefficients at $Re_\tau = 1000$

As seen in Fig. 2.12, it can be concluded that lower C_s values, which can be thought as lower eddy diffusion, result in an increased turbulent mixture that decreases the mean streamwise velocity due to transferred negative momentum from the wall.

In wind farm simulations, our main interest is currently based on mean hub height wind speed, where the flow will be driven with a pressure gradient linked to the magnitude of this velocity at hub level. Thus, although the mixing effect close to the wall changes drastically, usage of a simple SGS model is still acceptable for our current purpose.

For validation of the wind turbine model, normal force distribution is compared between CFD and BEM (Blade Element Momentum) methods. For this purpose, the NREL Phase VI rotor with the standard tip setting (see Hand *et al.* (2001)) is employed. Operating conditions of the rotor for the current test are given in Table 2.1.The polar data for this case was generated with an in-house viscous-inviscid interaction code, Q^3UIC (see Ramos-García *et al.* (2013)).

Rotor diameter	10.058 m
Root cut out	0.9 m
Rotational speed	7.50107 rad/s
Pitch angle	3°
Cone angle	0°
Wind speed	7 m/s

Table 2.1: Operation conditions for NREL Phase VI rotor

For this test, a CFD grid of 480 × 160 × 320 is employed for a domain size of $120 \times 40 \times 40m$. The projection width, ϵ, is taken as 3Δ which corresponds to $0.75m$. The resulting normal and tangential loading distributions are plotted against BEM computations in Fig. 2.13.

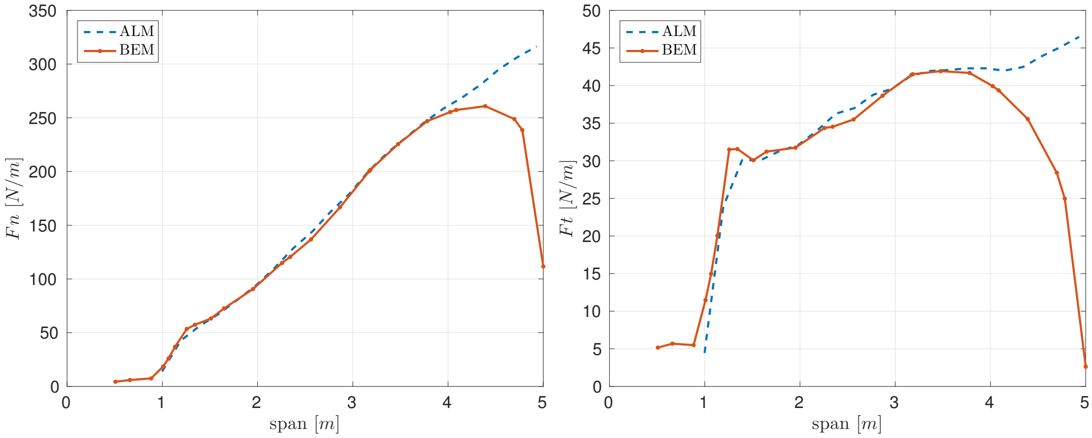

Figure 2.13: Comparison of the loading distributions obtained by BEM and ALM computations for NREL Phase VI rotor operating at 7 m/s uniform inflow.

It can be seen from the plots that the inner parts of the blade are in good agreement with the BEM results, however at the tip region the overestimate of the loadings exist. This issue will be investigated in further detail in the following chapter.

Chapter 3

Improved Actuator Line Modeling

Over-prediction of the wind turbine blade tip loadings with ALM is common knowledge, yet to date there has not been a reliable or a physical model developed to overcome the issue. There are two main underlying problems in ALM. First, due to the usage of force projection, vortices are generated with relatively large viscous core sizes that result in underestimation of the axial induction on the rotor plane, which leads to overestimation of the blade loads. Second, modeling wind turbine blades using information from a line instead of a surface, prevents capturing the effect of the wake induction change through the chord line. This results an overestimate of tip loading for flat tips, which leads to overestimating the total loading.

Part of the cause behind the over-prediction is enlightened by Shives & Crawford (2013), where the viscous cores of the trailing vortices were investigated and the linkage between the Gaussian projection parameter, discretization and accuracy was made. The authors suggested resolution parameters as well as the projection coefficient that would accurately capture the aerodynamic performance of an elliptic wing. However, the required resolution applied for ALM would be overkill for a wind farm application. Another work that addresses the issue is from Jha *et al.* (2014), where a new methodology is introduced in which the Gaussian projection parameter throughout the span is altered. This approach clearly improves the predictions. However, due to the introduced free parameters, their approach requires turbine specific tuning and does not actually solve the underlying problem in the ALM that smaller vortex cores are needed which result in instabilities with a fixed grid size.

In this chapter, these issues will be addressed in detail and a new correction will be introduced to overcome the aforementioned vortex core problem. Additionally, the recently introduced decambering correction technique by Sørensen *et al.* (2016) will be explained and implemented under the ALM framework and the results will be presented.

Throughout this chapter, the issues encountered in ALM computations and their effects are detailed at first. Then, the effects are handled under two separate titles. For each of these effects, a modeling approach is presented and validated by using two different planar wings.

3.1 Definition of the problems

3.1.1 Viscous core effects

In order to investigate the ALM in detail and simplify the problem, a planar wing ALM is implemented under the new LES framework. A rectangular wing ALM simulation is compared against a lifting-line computation and discrepancies in the circulation distribution are investigated. For CFD computations, a domain of 50×30×20m is employed with a fringe region length of 7.5m as illustrated in Fig. 3.1.

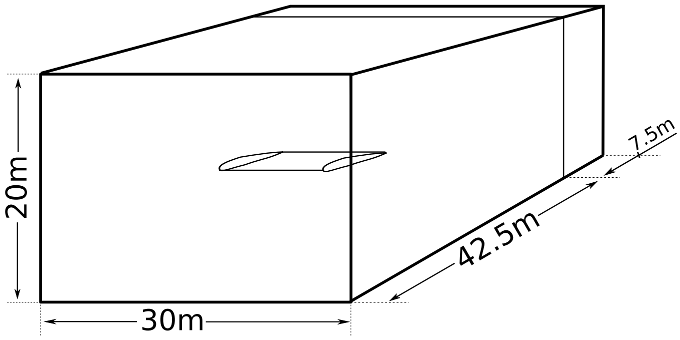

Figure 3.1: Illustration of the CFD domain and rectangular wing

The planar wing, with a constant chord of 1 meter and span of 10 meters is located at the center of the physical domain. The inlet velocity is fixed to be uniform $8m/s$ with the fringe forcing, and the initialization is made with a uniform $8m/s$ flow field. The geometrical angle of attack for the wing is 5° and inviscid polar curves are used from the NACA0012 profile for both CFD and lifting-line computations.

The circulation distributions are plotted in Fig.3.2 for different Gaussian projection parameters together with the lifting-line computation of the same wing. Due to the symmetry, only the half-span of the wing is plotted.

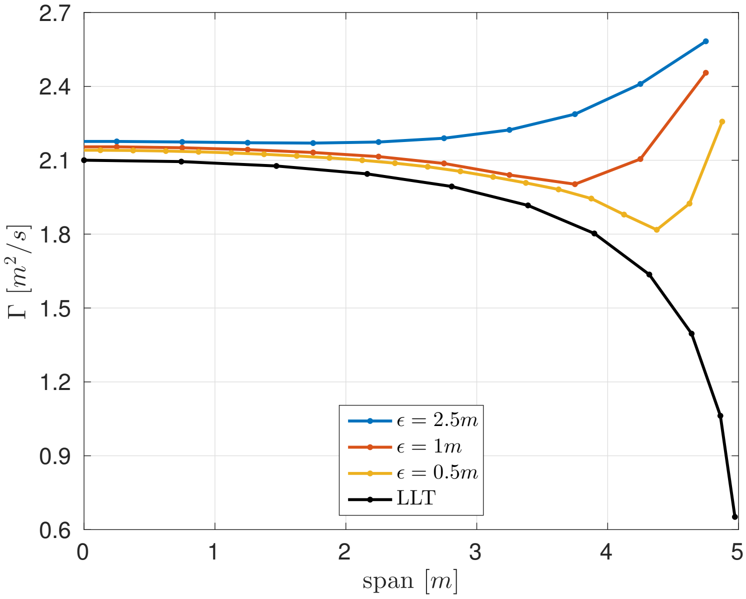

Figure 3.2: Comparison of circulation distribution for rectangular wing

It is observed that, the smaller the projection width ϵ becomes, the more the ALM results converge to the lifting-line circulation distribution. Additionally, the overestimation at the tip decreases with a decreasing ϵ value.

Due to the constant chord and zero twist throughout the span, the only parameter that affects the circulation is the local angle of attack α, which is found as

$$\alpha_{(j)} = \alpha_{geo} - \tan^{-1}(w_{i(j)}/U_\infty), \tag{3.1}$$

where α_{geo} is the geometric angle of attack of the wing, U_∞ is the free stream velocity, w_i is the local vertical velocity at the quarter-chord point of each segment and j is the segment number. Considering that the bound vorticity is defined at the quarter-chord point, where the self induction is zero, w_i consists only of the induction from the trailed wake vortices. With these in mind, it can be concluded from the plot that induction increases with decreasing ϵ parameter, in spite of the decrease in the bound circulation, which constitutes to weaker trailing vortices at the tip. This behavior gives a clue regarding the dependency of the viscous core of the vortices on the defined ϵ parameter.

To gain insight, a line vortex is generated with a predefined constant force that corresponds to the lift from an infinite wing at a geometric angle of attack of 5°, under $8m/s$ uniform inflow. The induction change w_i with respect to the distance to the center of the vortex $r[\Delta]$ is plotted in Fig. 3.3 for different ϵ values. To avoid the trailing vortices, an infinite wing is created in the CFD domain, the length of the vortex line is defined as the spanwise length of the whole domain.

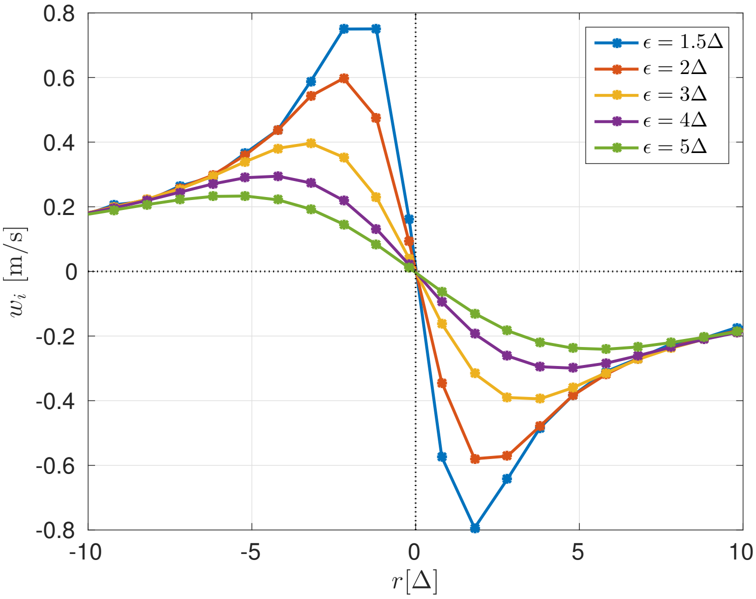

Figure 3.3: Inductions from the vortex line generated with different ϵ values.

The x-axis of the figure is made dimensionless with grid size Δ, which is kept constant for all the various ϵ cases. As seen from the figure, it is clear that ϵ parameter is linked to the core size of the generated vortex. On these grounds, it can be claimed that the increased ϵ would decrease induction close to the tip region since the tip vortices would not be able to generate the correct induction due to the viscous core effects, which then leads to an over-predicted angle of attack. The logical solution to the matter is to use a lower ϵ parameter. However, the problem that the researchers face is the fact that a lower ϵ value causes local instabilities on the CFD grid. To illustrate, some oscillations from the previously shown line vortex are plotted in Fig. 3.4 with respect to varying ϵ parameter.

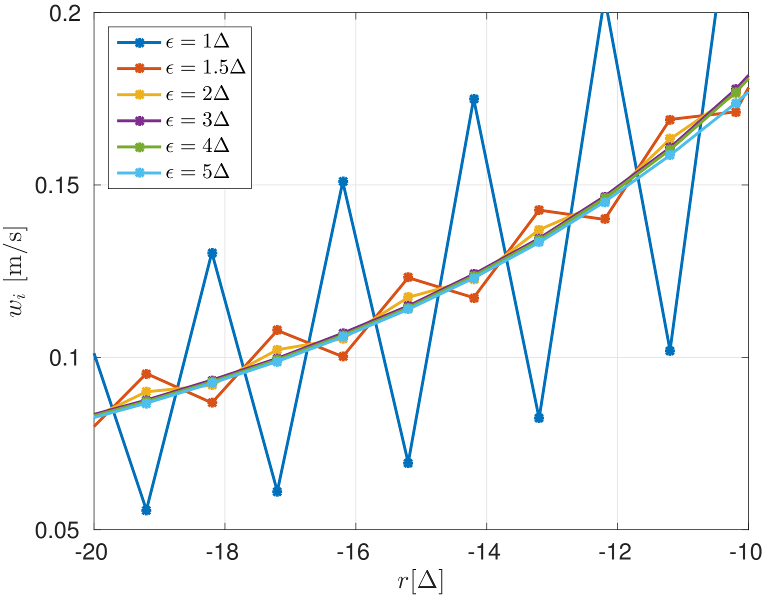

Figure 3.4: Visible oscillations for different ϵ parameters

To dampen these oscillations, researchers often employ dissipative differentiation/interpolation schemes or apply manual filtering operations in wavenumber space, which becomes mandatory in order to use low ϵ/Δ values.

3.1.2 Decambering effects

Other than numerical isues that cause large vortex cores and alter the induction levels at the tips, there is a physical phenomenon that can not be captured by blade-element like models due to the usage of the 2D polar data on 3D flow fields. Polar curves for airfoils are obtained from wind tunnel experiments or 2D CFD computations. In both sources, the definition of the angle of attack is made as the geometric angle between the chord line and the incoming velocity vector. To account for the wake effects in 3D applications, inductions are calculated from the trailed vortices and combined inside the relative velocity vector, which is then used to define the angle of attack. To calculate inductions, the quarter-chord point is often used because it is known to be a good estimate for the aerodynamic center of the airfoils. For the same reason, the bound vorticity is also defined at this point. Thus self induction at this point is zero. The underlying assumption made to connect these two angle of attack definitions is that the angle of attack is constant throughout the chord line. This is often not the case for 3D applications because the induction from wake vortices change in the chord-line depending on the position from which it is computed. The illustration of induction change for an airfoil that is used in a 3D wing is made in Fig. 3.5.

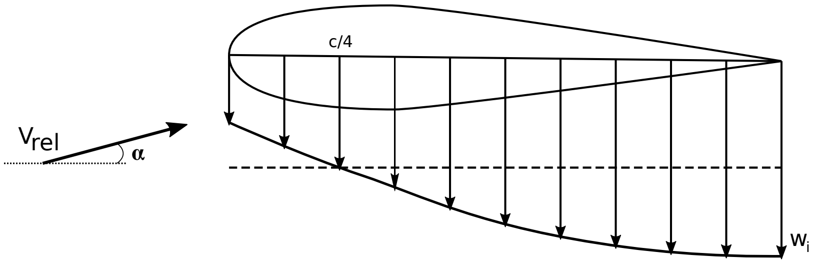

Figure 3.5: Induction change on an airfoil section

As shown in Fig. 3.5, the induction from the wake increases further downstream on the chord line. Thus, it is questionable to assume a constant angle of attack for such an airfoil segment. This induction change is negligible for the inner parts of a wing due to the weak trailing vortices. However, the change is known to be strong close to the tip region where the local trailing vortices are much stronger, especially for flat tips.

3.2 Correction methodologies

3.2.1 Viscous core correction

As the problem is introduced in Sect. 3.1.1, it is expected from a correction to account for the deficiency of the wake induction due to the introduced viscous vortex cores. To account for the difference, a viscous core model is defined to link the vortex core size to ϵ value analytically. It is found that the *Lamb-Oseen* vortex model, which is shown below, gives a similar induction profile as from a vortex that is generated from a defined body force in an ALM computation. Induction from a *Lamb-Oseen* type vortex line is defined as

$$w_i = \frac{\Gamma}{2\pi r}\left(1 - exp\left(\frac{-r^2}{r_{vc}^2}\right)\right), \tag{3.2}$$

where Γ is the vorticity, r is the distance to the induction point from the center of the vortex and r_{vc} is the viscous core radius (Lamb (1932)). From this expression it is readily seen that the first term corresponds to the inviscid part of the induction and the second term accounts for the influence of the viscous core. An interesting observation of this study is that, using $r_{vc} = \epsilon$, we obtain the exact same induction as in the CFD computation. This behavior is shown in Fig. 3.6 for different ϵ values.

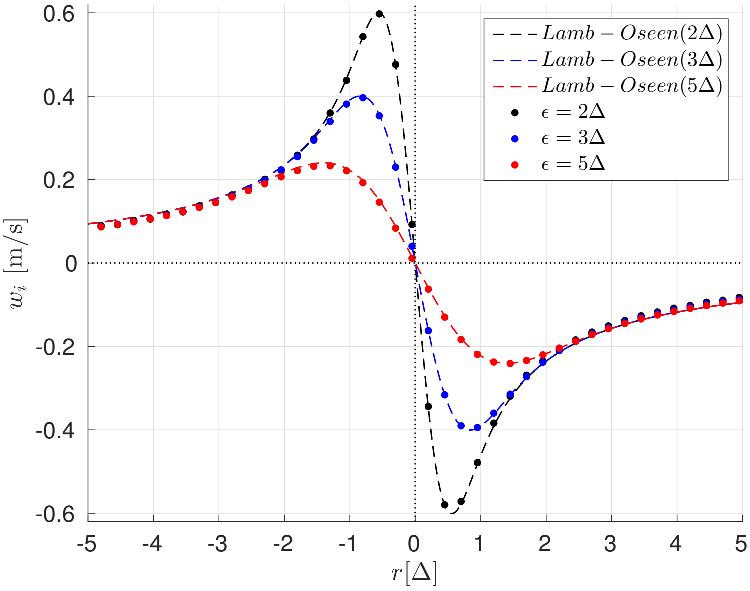

Figure 3.6: Comparing analytical viscous vortex model with the computed inductions from the CFD computation.

With this information, we can make an analytical estimate of the missing induction as a result of having an artificial viscous core. In Fig. 3.7 the induction with *Biot-Savart* law, which assumes zero vortex core, and the viscous vortex induction with $\epsilon = 3\Delta$ is plotted. The difference between these two inductions (see the swept area in the figure) represents the missing induction in an ALM simulation with a given ϵ parameter.

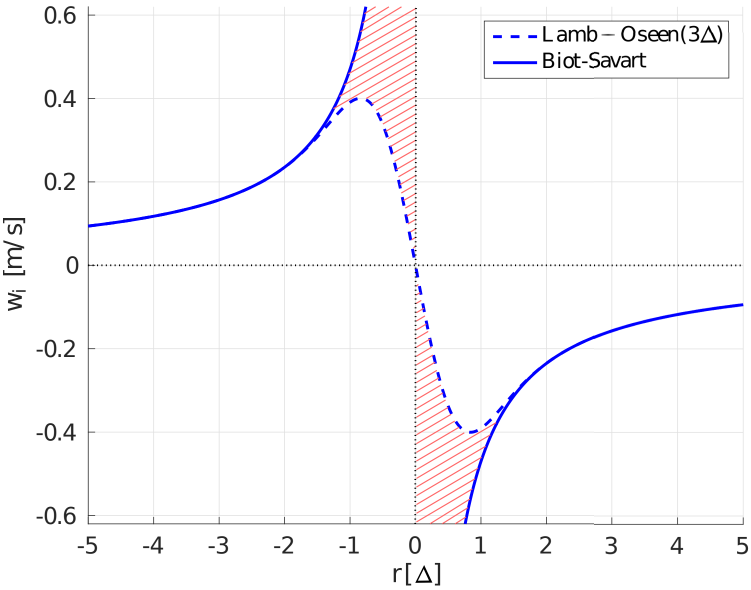

Figure 3.7: Illustration of the viscous correction on induction for $\epsilon = 3\Delta$

An analytical formula can be obtained by subtracting the *Lamb-Oseen* vortex induction from a pure *Biot-Savart* induction,

$$w_{corr} = \frac{\Gamma}{2\pi r} - \frac{\Gamma}{2\pi r}\left(1 - exp\left(\frac{-r^2}{\epsilon^2}\right)\right). \tag{3.3}$$

In Eq. 3.3, w_{corr} represents the missing induction a distance of r away from the generated vortex center. The resulting function for different ϵ values is plotted below.

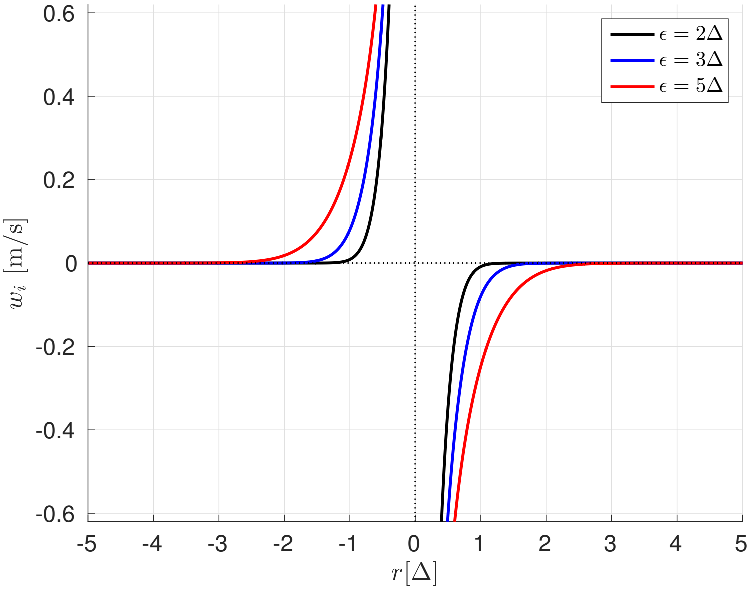

Figure 3.8: The missing induction versus the distance from the vortex core that is generated with force projection with given ϵ parameter.

At this stage, one can correct the induction from a vortex that is generated by a projected force in a CFD computation, and obtain to the induction that would have occurred with no viscous core effects.

3.2.2 Decambering correction

As briefly explained in Section 3.1.2, decambering is an artifact of linking 2D airfoil data to 3D with a single point measurement. Referring back to Fig. 3.5, the additional induction $\Delta w_i = w_i - w_{i,c/4}$ causes curved streamlines on the airfoil segment. To model this effect the curvature of these streamlines can be transferred to the chord line as camber of the airfoil segment and thin airfoil theory can be used to calculate the resulting lift change. The name decambering stands for the negative cambering that is used to model this phenomena. The illustration of this negative cambering is shown in Fig. 3.9.

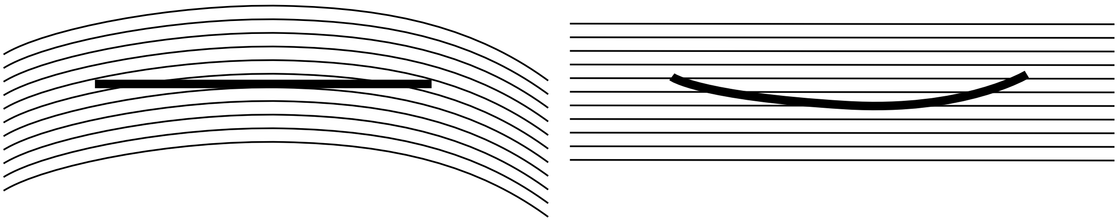

Figure 3.9: Curved streamlines due to the additional induction (left), and the same effect as generated by a negative cambered chord line (right).

To define the additional induction, the Biot-Savart law can be used with defined wake vortices. For a wing application, these vortices are line vortices that trail from the quarter-chord point and extend to downstream-infinity (see Fig. **??**). For rotors, a helical wake (see Fig. 4.6), which also trails from the quarter-chord line, is employed. The strength of these trailing vortices is defined from the corresponding bound vortex. From thin airfoil theory, the effect of decambering can be calculated by using the formula for calculating the zero-lift angle that is used for cambered airfoils (see Katz & Plotkin (2001) Sect.5.4),

$$\alpha_{L0} = -\frac{1}{\pi}\int_{0}^{\pi} \frac{d\eta}{dx}(cos\theta - 1)d\theta. \tag{3.4}$$

The α_{L0} is the angle of attack that would generate a zero lift for a given chord line, where the chord line is defined with a local slope of $d\eta/dx$. The integral can be computed with a trapezoidal sum by defining control points with a cosine distribution over the chord line as shown in Fig. 3.10.

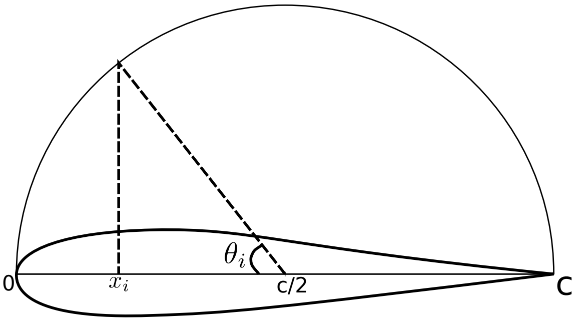

Figure 3.10: Cosine distribution of the control points on airfoil chord line.

The value of $d\eta/dx$ at the control point i is equal to the additional streamline curvature at the location in the opposite direction. Thus, from the local inductions and relative velocity, the local slope of the chord line can be estimated as

$$\left.\frac{d\eta}{dx}\right|_i = \frac{w_i - w_{i,c/4}}{u_{rel} cos\alpha}. \tag{3.5}$$

Due to the low angles of attack, the effect of the additional induction on the relative velocity is neglected in the Eq. 3.5. By using this definition, the integral can be rewritten discretely as

$$\alpha_{L0} = -\frac{1}{\pi}\Delta\theta \sum_{i=1}^{N} \frac{(w_i - w_{i,c/4})(cos\theta_i - 1)}{u_{rel} cos\alpha}, \tag{3.6}$$

with N being the number of discreet control points on the chord line and $\Delta\theta$ is the angular distance in between these points. With α_{L0} for each airfoil section, the local angle of attack values can be corrected as $\alpha_{new} = \alpha - \alpha_{L0}$, and interpolated polar data can be updated. Since this update changes the bound circulation, the procedure has to be applied iteratively. In this work, the decambering correction is patched on top of the viscous core correction and converged bound circulations are obtained for every time step.

3.3 Modeling and validation

3.3.1 Viscous core correction

The correction is meant to be applied at the angle of attack calculation stage, where the total additional induction from the wake system w_{corr} is added to the local relative velocity and angle of attack value is altered. To apply the correction, the location of the wake vortices and their strengths have to be defined in advance as these are required by the Eq. 3.3. For a planar wing application, wake vortices can be assumed to form a straight vortex sheet which is parallel to the flow and trail from the quarter-chord line of the wing (see the Fig.3.11). Then, for each actuator line point, the total correction

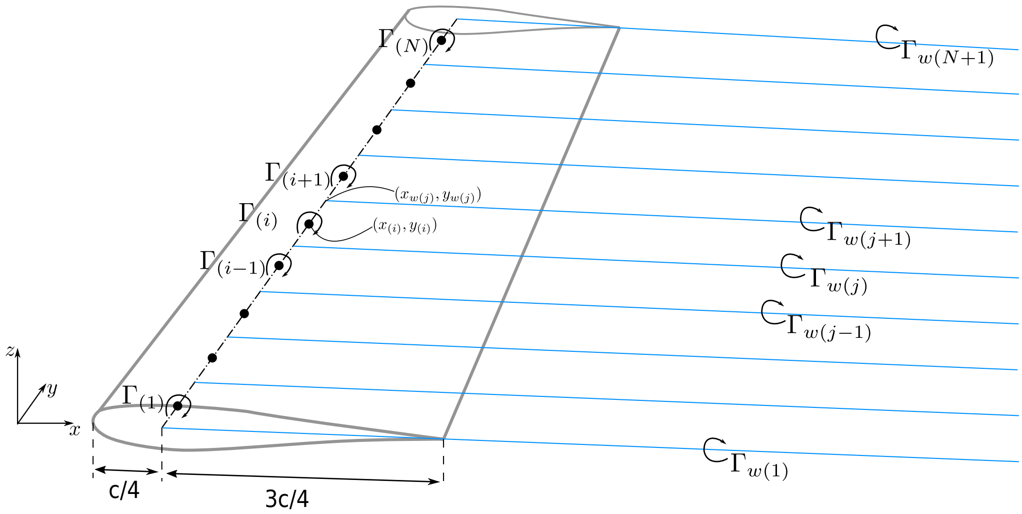

Figure 3.11: Illustration of a vortex system of a planar wing

from the viscous cores of the wake vortices can be calculated as

$$w_{corr(i)} = \sum_{j=1}^{N+1} \frac{\Gamma_{w(j)}}{4\pi r_{(i,j)}} exp\left(\frac{-r^2_{(i,j)}}{\epsilon^2}\right). \tag{3.7}$$

N here is the total number of actuator line points on and Γ_w represents the circulation strength in the wake vortices, while the magnitudes are equal to the difference between the two neighboring bound circulations where the wake vortex trails,

$$\Gamma_{w(j)} = \Gamma_{(j)} - \Gamma_{(j-1)}. \tag{3.8}$$

For the tip vortices, the magnitudes are equal to the bound circulations which are closest to the tips. In this system the strength of a bound circulation is a function of the corresponding chord c, relative velocity u_{rel} and the lift coefficient C_L,

$$\Gamma_{(i)} = \frac{1}{2}\, c_{(i)}\, C_{L(i)}\, u_{rel(i)}. \tag{3.9}$$

In Eq.3.7, the r variable is defined individually for each trail-actuator line point couple. The definition in the given coordinate system [1] (see Fig.3.11) can be written as

$$r_{(i,j)} = y_{(i)} - y_{w(j)}. \tag{3.10}$$

---

[1] Note that span of the wing is aligned with the y axis for the simplicity.

With the known total induction correction, angle of attack values on each actuator line point can be corrected by simply accounting the additional induction,

$$\alpha_{(i)} = \alpha_g - tan^{-1}\left(\frac{-u_{z(i)} + w_{corr(i)}}{u_{rel(i)}}\right). \tag{3.11}$$

In Eq. 3.11 α_g represents the geometrical angle of attack of the wing, u_{rel} and u_z are the relative and the vertical velocity components, respectively. An illustration of the induction correction for a single vortex line is shown in Fig. 3.12. In this figure, the dashed blue line represents the underestimated induction from the tip vortex in the CFD computation, which causes over estimated tip loadings. The thick blue line is the induction that would occur in a LLT case. Hence, the red swept area is the induction correction which correct the angle of attack values at the region. The consequence of modifying the values of angle of attack, bound vorticity and, hence, the strengths of the wake vortices change. Therefore, the correction requires an iterative procedure in each time step of the CFD computation.

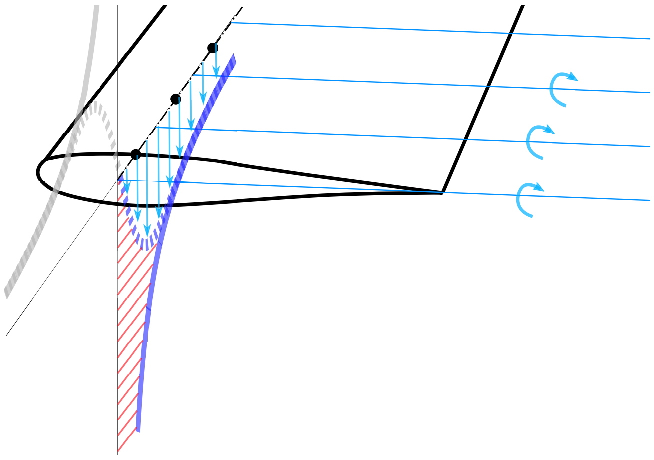

Figure 3.12: Illustration of the induction correction for the tip vortex

For the test case, two different rectangular (constant chord of 1 m) wings with aspect ratios AR=6 and AR=10 are used. A CFD grid resolution of 100 × 60 × 80, that corresponds to 0.5 m on span-wise and stream-wise, and 0.25 m on vertical direction is used. The domain size was 50 × 30 × 20 m as reported before in Fig. 3.1. The projection parameter ϵ is taken as 1 m which corresponds to 2Δ for this grid setting. The circulation distributions with, and without, the correction for both wings are compared in Fig. 3.13. The computations with the correction are represented as ALM* whereas

LLT and ALM correspond to the lifting-line technique and actuator-line method as used before.

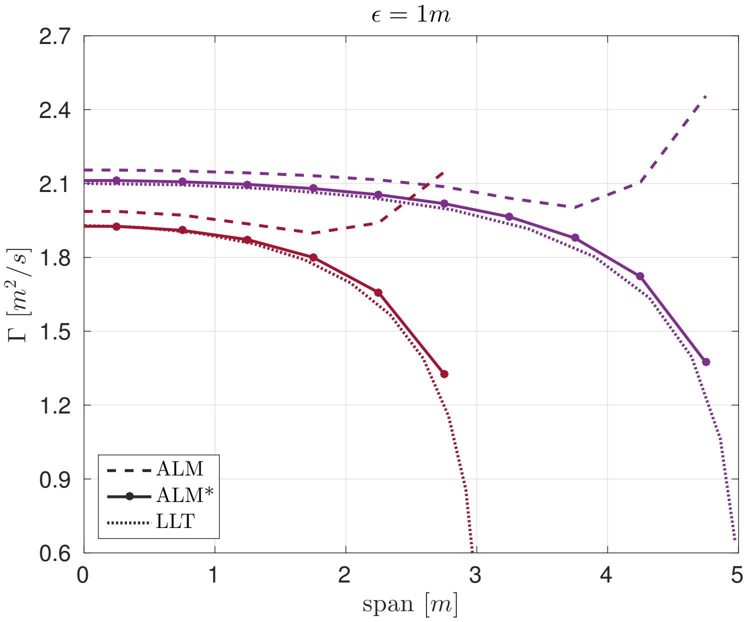

Figure 3.13: Comparison of the calculated circulation distribution with the new correction.

It is seen from the plot that the correction greatly improves the results at the tip region. At the mid-span region, the correction decreases the loading and the maximum circulation is closer to LLT computations for both cases.

3.3.2 Decambering correction

In this section, the application of the decambering correction for a planar wing is presented. Since LLT is not capable of capturing decambering effects, results are compared against an in-house viscous inviscid interaction code MIRAS (Ramos-García *et al.* (2013)) that resolves the whole blade geometry. In Fig. 3.14, both LLT and MIRAS results are shown to emphasize the change. Furthermore, the comparisons are made using two different ϵ values, where for $\epsilon = 2.5$ m, a CFD grid resolution that corresponds to 20 grid points per wing span, and for $\epsilon = 0.75$ m, a CFD grid resolution that corresponds to 40 grid points per wing span is used. The actuator line computations with viscous core and decambering corrections are represented by ALM**, whereas only viscous core applied actuator line computations are again shown with ALM*.

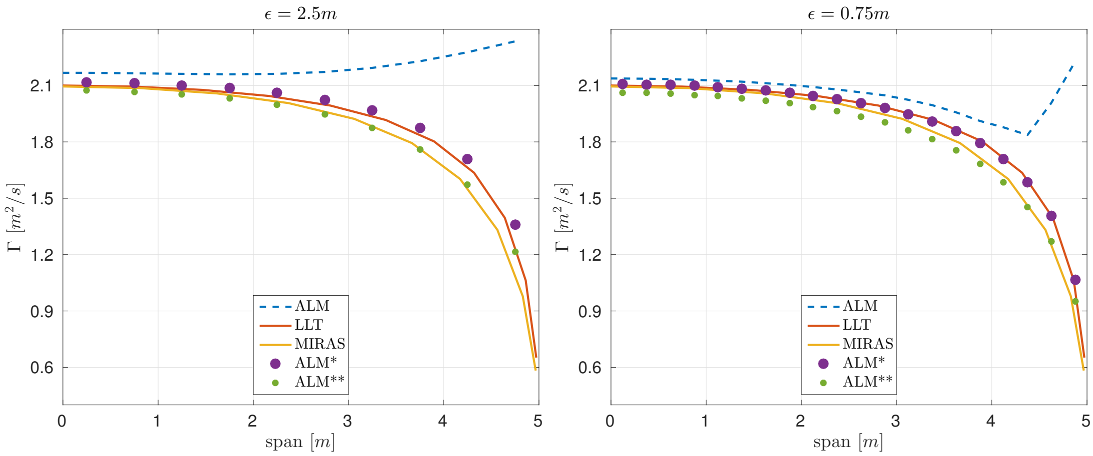

Figure 3.14: Computed circulation distributions for AR=10 wing by using decambering correcition applied on the top of ALM* method.

As seen from the figure, the decambering correction captures the effect of angle of attack change in both figures, whereas LLT and ALM* overestimate the circulation around the tip regions. It is also noted that the decambering correction decreases the loading, also in the mid-regions of the span for $\epsilon = 0.75$ m case, which then results in a slight underestimate of the loadings at the region.

Chapter 4

Parameter Study and Rotor Applications

Prandtl's lifting-line theory underlies the actuator line methodology. In the theory, the bound vorticity from the lifting surface is continuous and inviscid, which then constitutes a continuous wake vortex sheet. The well known lifting-line technique is simplified application of this theory where continuous vorticity is replaced with discrete vortices and their inductions are computed on discrete points in between trailed wake vortices. The ALM, on the other hand, lies somewhere in between these two where Navier-Stokes equations are solved to represent a continuous flow field, and discrete bound vortices (from each lifting element) are translated to a continuous-like vortex-line by a projection function (see Fig.4.1).

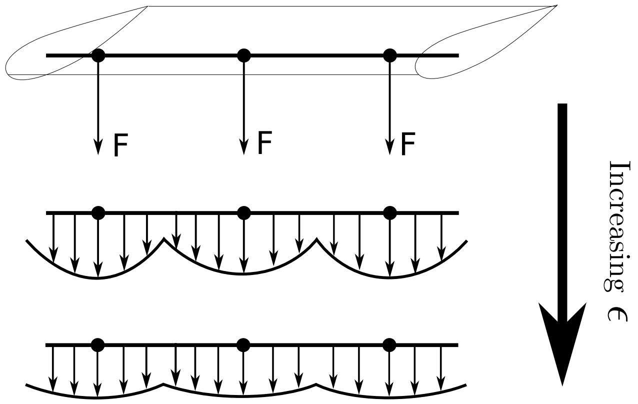

Figure 4.1: Illustration of a loading distribution with increased projection width.

Despite the similarity, the projection application in ALM forms vortices with viscous cores, which cause the method to diverge from Prandtl's theory. With the application of the correction introduced in the previous chapter, the side-effects of the viscous cores can be removed but the correction requires assumptions with an analogy to the discrete lifting-line technique.

In this chapter, to further validate the model, we will apply it to turbine rotors and investigate the variations in the results due to the assumptions made. Additionally, the model will be tested by using different parameters under both uniform and turbulent flow conditions.

4.1 Parameter study on planar wings

4.1.1 Varying ϵ parameter

In this section different ϵ values are tested for AR=10 rectangular wings and the results are reported in detail. The CFD grid resolution used for $\epsilon = 2.5$ m case was $100\times60\times80$, which corresponds to 20 grid points per span length for $AR = 10$ wing with $\epsilon/\Delta = 5$, and for $\epsilon = 0.5$ m case the resolution is doubled to keep ϵ/Δ value at a minimum of 2. The same domain as shown in Fig. 3.1 was used. The circulation distributions for half-span are shown in Fig. 4.2 and Fig. 4.3 for $AR = 6$ and $AR = 10$ respectively.

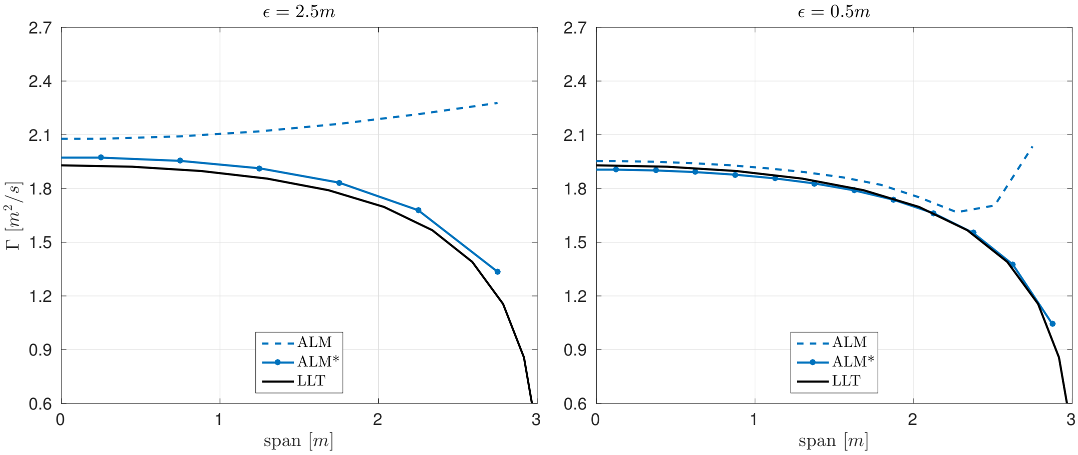

Figure 4.2: Comparison of circulation distributions with different projection width by using rectangular wing with AR=6 and $\epsilon = 2.5$ m (left), $\epsilon = 0.5$ m (right).

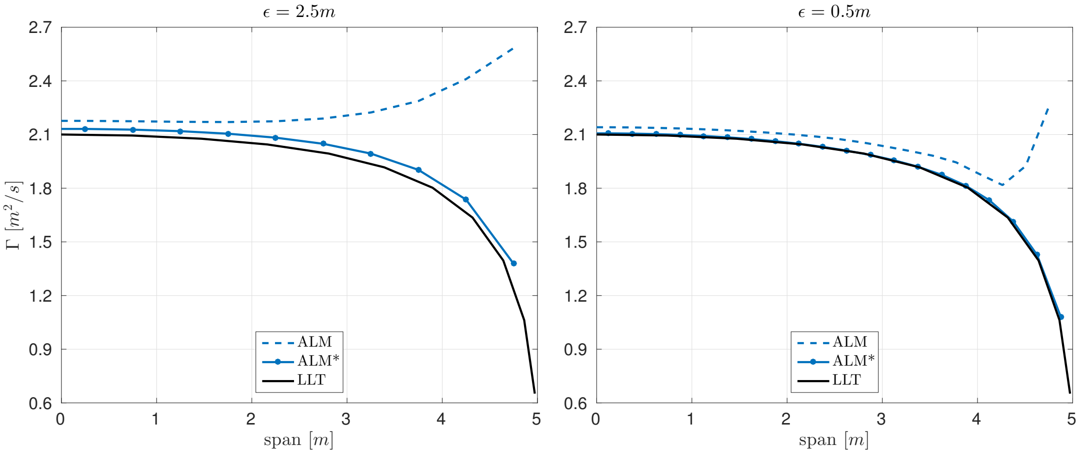

Figure 4.3: Comparison of circulation distributions with different projection width by using rectangular wing with AR=10 and $\epsilon = 2.5$ m (left), $\epsilon = 0.5$ m (right).

It can be seen from the figures that in both cases, and for both ϵ values, the circulation at the tip regions with correction are much closer to LLT results. Further, for $\epsilon = 2.5$ m $= 5\Delta$ a slight overestimate of the loading is visible for both wings, and a very small underestimate of the maximum loading for $\epsilon = 0.5$ m $= 2\Delta$ case with $AR = 6$ wing is visible.

4.1.2 Varying actuator line resolution

From the flow solver's perspective, as soon as the force distribution is smooth, the results would not change with finer actuator resolution since the total force will always be the same. However, it is important to make sure that the introduced correction is consistent in itself with finer or coarser actuator meshes, which defines the number of the trailing vortices and the circulation distribution in the imaginary wake that is used to apply the correction.

To confirm this, 2 test cases were generated for constant ϵ values of 1.25 m and 0.5 m with the given CFD grid of $200 \times 120 \times 160$ for streamwise, spanwise and vertical direction, respectively. Within this setup, the actuator resolution is varied with and without the correction and circulation distributions are compared against lifting-line computations for the rectangular wing with an aspect ratio of 10. The results are shown below in Fig. 4.4. In the plots, da value represents the distance between actuator points, which are equidistantly distributed on the actuator line.

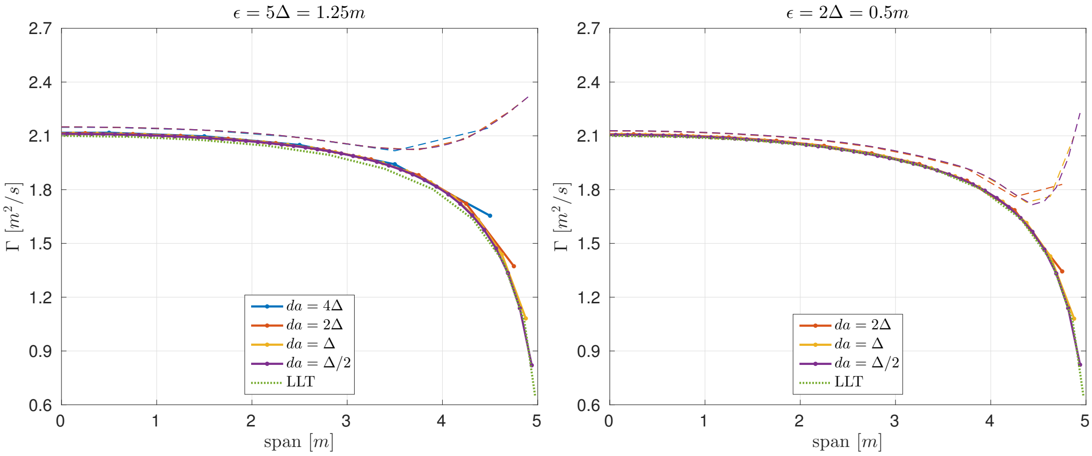

Figure 4.4: Comparison of circulation distributions with different actuator resolution parameters by using rectangular wing with AR=10 and $\epsilon = 1.25$ m (left), $\epsilon = 0.5$ m (right).

For $\epsilon = 1.25$ m case, there are four different da cases tested, whereas $\epsilon = 0.5$ m case became unstable with the coarsest actuator grid setting. As a consequence, only three cases were tested. Computations without the correction are represented with dashed lines for all cases with the same colors as the correction applied counterparts.

It can be concluded that the correction is consistent with different actuator spacing and that the results are in agreement in both cases.

4.1.3 Varying CFD grid resolution

To test the effect of the CFD grid resolution on the correction, a test case was made with a fixed ϵ parameter. The actuator spacing da was linked to the grid size as $da = \Delta$. For three different CFD resolutions, resulting circulation distribution is compared against lifting-line computations for the rectangular wing with the aspect ratio 10. The results without the correction are also plotted. The grid settings used in this study were $400 \times 240 \times 320$, $200 \times 120 \times 160$, and $100 \times 60 \times 80$, which correspond to maximum grid distance Δ being 0.125 m, 0.25 m and 0.5 m respectively. Thus, for $\epsilon = 1$ m, the minimum ϵ/Δ value used was 2.

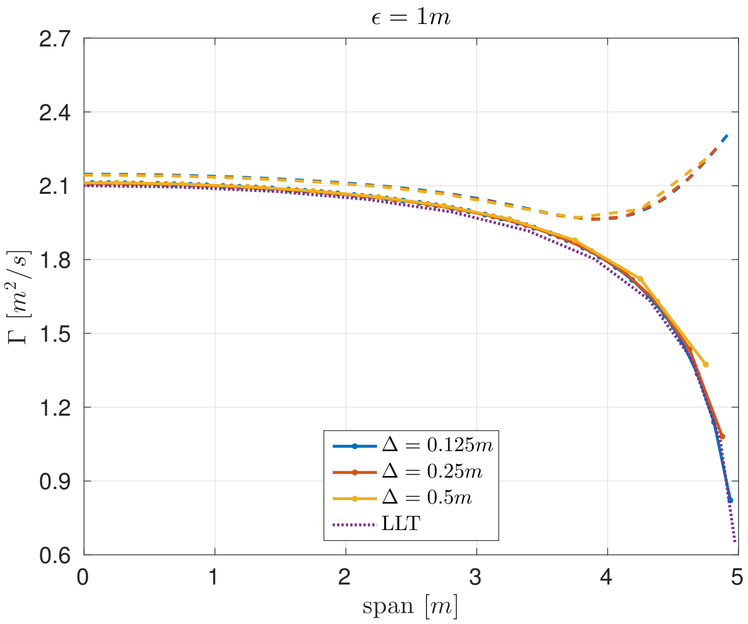

Figure 4.5: Comparison of circulation distributions with different CFD grid resolutions by using AR=10 wing.

From Fig. 4.5, it can be concluded that for a constant ϵ value, the results are consistent within each other and the correction is independent of the CFD grid resolution.

4.2 Viscous core correction - rotor application

To apply the viscous correction for a wind turbine rotor, the position of the discrete line vortices inside the wake is needed. As used in the previous section, to generate the wake, trailing vortices are prescribed starting from the quarter-chord line. Unlike a planar wing, these vortices follow a downstream helical shape with the predefined constant helical pitch. The illustration of the wake is shown below in Fig. 4.6 (left). To define the helical pitch, an assumption of linear increase towards the tip is made for averaged axial induction factor (a^*), which are then used together with rotational speed and free stream velocity to define the local value of the helical pitch for each trailed vortex line. In Fig. 4.7, a comparison of this linear assumption and blade-element-momentum (BEM) calculations of a^* value is shown for NREL Phase VI and NREL 5MW turbines. It must be noted that, the azimuthal averaged a^* is the factor that defines the helical pitch. To compare our linear assumption, a^* values are computed from the converged BEM results by disregarding the Prandtl's tip correction. In this section, given a^*

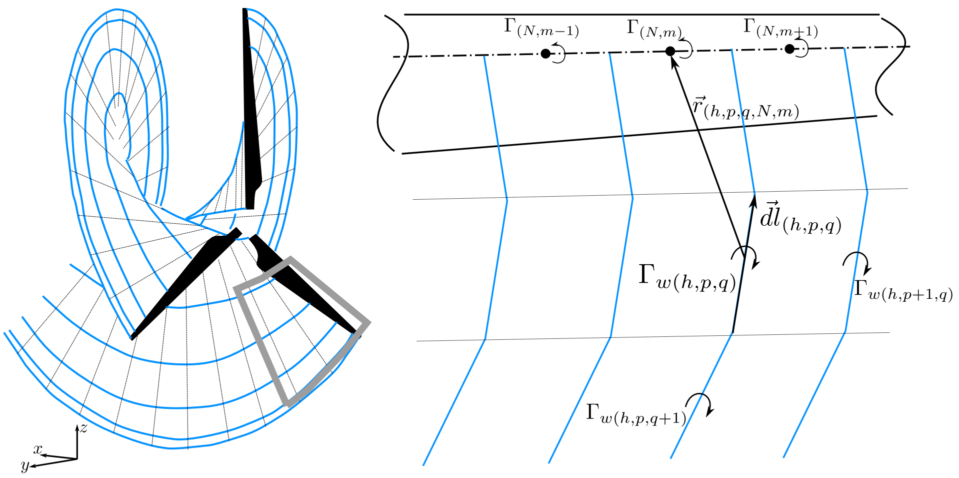

Figure 4.6: Illustration of the helical wake released from a wind turbine rotor(left), a close-up illustration of the wake formation of the single blade(right).

distribution is used for all simulated cases.

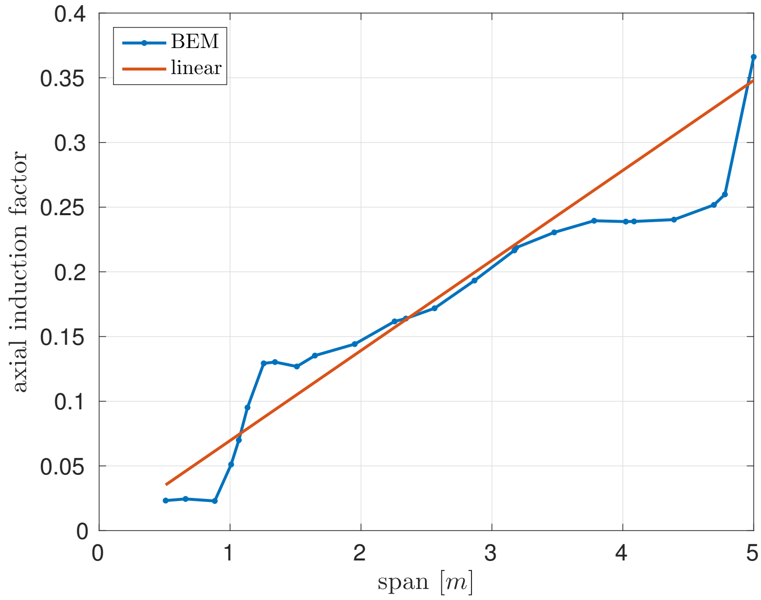

Figure 4.7: Comparison of the linearly increased axial induction factor against BEM computations for NREL Phase VI turbine operating at $7m/s$

The correction is applied exactly the same as in planar wing case that in each time step an iterative core correction was conducted for each blade and control point, and circulation distribution in the wake is updated respectively. Due to the three-dimensional formation of the wake, it is necessary to define the discrete vortex lines and calculate the induction correction in three-dimensional space accordingly. By using the vector notation, the induction correction from a vortex line can be calculated as

$$\begin{bmatrix} w_{xcorr} \\ w_{ycorr} \\ w_{zcorr} \end{bmatrix} = \frac{\Gamma}{4\pi} \frac{\vec{dl} \times \vec{r}}{|\vec{r}|^3} \left(exp \frac{-|\vec{r}|^2}{\epsilon^2} \right), \tag{4.1}$$

where $\vec{dl}$ is the the vector which represents the direction and the length of the vortex line, $\vec{r}$ is the vector from the center of the vortex line to the induction calculation point (see Fig. 4.6 (right)). Then for each actuator line point the total induction correction can be calculated by summing all the corrections from the wake system as

$$\begin{bmatrix} w_{xcorr} \\ w_{ycorr} \\ w_{zcorr} \end{bmatrix}_{(N,m)} = \sum_h \sum_p \sum_q \frac{\Gamma_{w(h,p,q)}}{4\pi} \frac{\vec{dl}_{(h,p,q)} \times \vec{r}_{(h,p,q,N,m)}}{|\vec{r}_{(h,p,q,N,m)}|^3} \left(exp \frac{-|\vec{r}_{(h,p,q,N,m)}|^2}{\epsilon^2} \right). \tag{4.2}$$

Here, the indices h,p and q represent the blade number, span position and the azimuthal position respectively for the wake vortices, and N and m represent the blade number and span position for actuator line points (see Fig.4.6 (right)). The circulation strengths are calculated similar to the planar case as

$$\Gamma_{(N,m)} = \frac{1}{2}\, c_{(N,m)}\, C_{L(N,m)}\, u_{rel(N,m)}, \tag{4.3}$$

and

$$\Gamma_{w(h,p,q)} = \Gamma_{(p-1,q)} - \Gamma_{(p,q)}. \tag{4.4}$$

With the calculated total induction correction for each actuator line point, the flow angle can be corrected as

$$\phi_{(N,m)} = tan^{-1} \left(\frac{u_{x(N,m)} + w_{xcorr(N,m)}}{u_{\theta(N,m)} + w_{\theta corr(N,m)}} \right), \tag{4.5}$$

where

$$w_{\theta corr(N,m)} = w_{ycorr(N,m)}\, cos(\theta_N) + w_{zcorr(N,m)}\, sin(\theta_N). \tag{4.6}$$

Next, the new angle of attack values can be computed locally by the Eq.2.29.

Initially, two different turbines with different tip shapes are used to test the correction. The first turbine used is NREL Phase VI, with a rotor diameter of 10.058 m with the standard tip setting. The chord distribution is shown in Fig. 4.8. Due to the two-bladed rotor design, and relatively large chord lengths at the tip region, this particular turbine is expected to produce strong tip vortices.

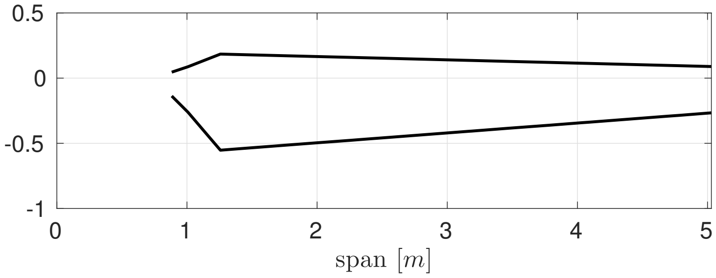

Figure 4.8: Chord distrbution of the NREL Phase VI blade.

The second turbine used is the 3-bladed NREL 5MW, which has a $126m$ rotor diameter. The chord distribution for this rotor is shown in Fig. 4.9. In comparison with Phase VI rotor, the NREL 5MW has a relatively sharp tip, therefore it is expected to have a loading distribution which gradually decreases towards the tip of the blade due to the small chord lengths around the tip region.

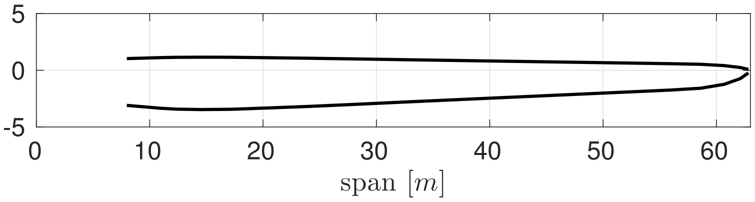

Figure 4.9: Chord distribution of the NREL 5MW blade.

For the test cases, a CFD domain of $12D \times 4D \times 4D$ with a resolution of $480 \times 160 \times 320$ is used for both turbines, and the turbines are positioned at the center of the domain at $2D$ downstream distance. To check the domain blockage effects, a domain size of $18D \times 6D \times 6D$ is also employed but no visible loading changes were seen. The operation conditions that are used for computations are given in Table 4.1.

	PHASE VI	**5MW**
Rotor diameter	10.058 m	126 m
Root cut out	0.9 m	5 m
Rotational speed	7.50107 rad/s	0.9584 rad/s
Pitch angle	3°	0°
Cone angle	0°	0°
Wind speed	7 m/s	8 m/s

Table 4.1: Operation conditions for NREL Phase VI and 5MW rotors

The Gaussian projection width for this study is taken as $\epsilon = 3\Delta$, which corresponds to 0.75 m and 9.45 m for Phase VI and 5MW cases respectively. The normal and tangential loading comparisons are plotted in Fig. 4.10 for Phase VI rotor and Fig. 4.11 for 5MW rotor. The correction applied ALM computations are shown as ALM^*.

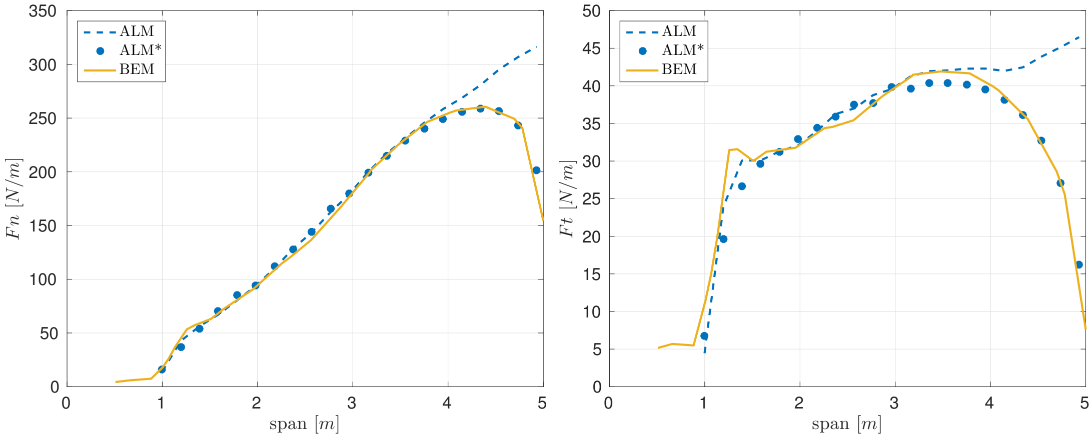

Figure 4.10: Comparison of normal and tangential loadings from ALM with and without the correction, and BEM computations for NREL Phase VI turbine.

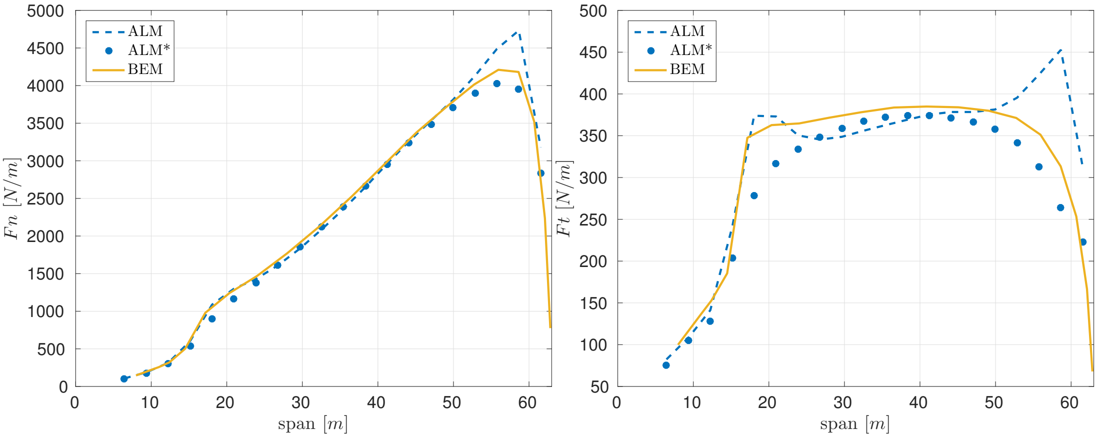

Figure 4.11: Comparison of normal and tangential loadings from ALM with and without the correction, and BEM computations for NREL 5MW turbine.

It can be concluded from the figures that with the application of the correction, there is a great improvement for both normal and tangential tip loadings, for both turbines.

4.3 Parameter study on NREL 5MW and Phase VI rotors - uniform inflow

4.3.1 Varying ϵ parameter

As mentioned before, ϵ parameter is used to avoid oscillations in the flow. As shown in the previous sections, very low ϵ values produce visible unphysical oscillations thus it is good practice to use a higher ϵ value. In this section, the effect of the ϵ parameter on loading distribution is explored. For this purpose, NREL Phase VI and 5MW turbines used at previously given operating conditions. The CFD grid employed has a resolution that corresponds to approximately 20 grid-points per blade for both turbine cases.

Three different ϵ values are used for both turbines and in total 12 simulations are conducted for this study. The comparisons of the loading distributions through the blade spans are shown in Fig. 4.12 for NREL Phase VI and Fig. 4.13 for NREL 5MW rotors with operating conditions used in the previous case. The ALM computations without a correction are represented with dashed lines and corresponding correction applied cases are represented with dots with the same color types.

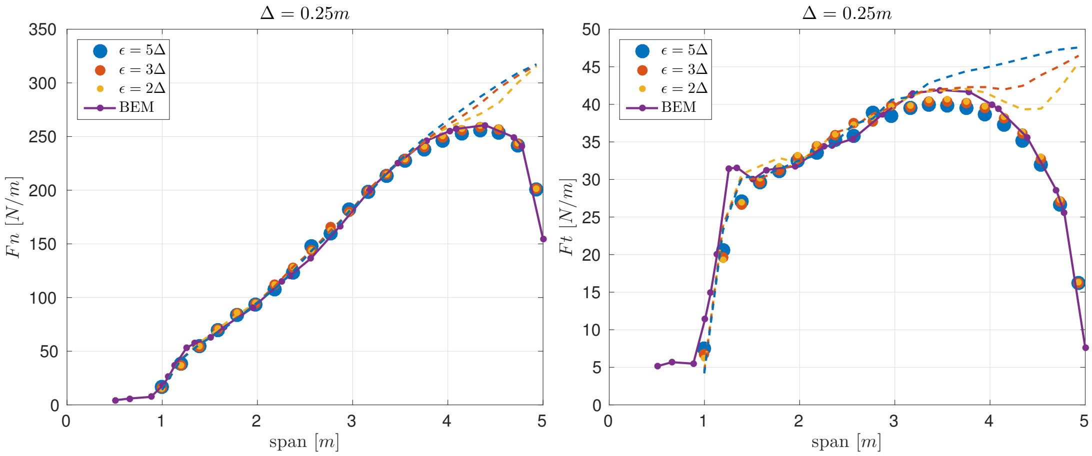

Figure 4.12: Comparison of normal and tangential loadings from ALM with and without the correction, and BEM computations for NREL Phase VI turbine with varying ϵ parameter.

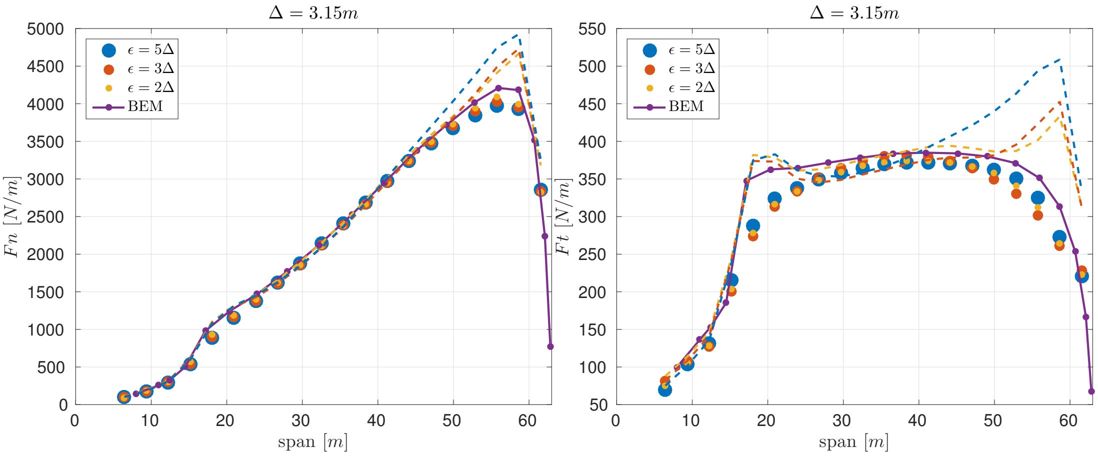

Figure 4.13: Comparison of normal and tangential loadings from ALM with and without the correction, and BEM computations for NREL 5MW turbine with varying ϵ parameter.

As seen from the plots, ALM computations without a correction overshoot the normal loadings art the tip region even with $\epsilon = 2\Delta$ and for the tangential loading, a very high estimate is visible at the tip region with increased ϵ value, especially for 5MW rotor. The correction applied ALM computations show consistent tip loads for normal loading distributions for the Phase VI rotor, and distribution of the tangential loadings are improved at the tip region. Also, for the 5MW rotor, normal loadings are improved at the tip region and the results show slight convergence towards BEM results with decreased ϵ value. The tangential loadings, on the other hand, $\epsilon = 2\Delta$ case is the closest to the BEM computations and, in all three cases, correction greatly improves the tip over-shoot for tangential loadings.

It can be concluded that the new correction corrects the excessive tip loadings. Additionally, an applied correction with a lower ϵ parameter produces better results for the 5MW rotor blade.

4.3.2 Varying actuator line resolution

The correction assumes distinct vortex lines inside the wake and corrects for the missing induction for each. However, in reality as well as in CFD simulations, the wake is a continuous vortex sheet that reconstruction with distinct line vortices might not be physically correct for such coarse grids that we employ. Varying actuator grid spacing directly influences the number of the bound vortex points thus the virtual trailing vortices that are used for the correction, regardless of the background CFD grid resolution. As used in lifting-line technique, it is reasonable to increase the bound vorticity and trailing vortices and the results will be consistent. However, since the correction is applied as a correction for the missing part of the induction from the vortices inside the wake, it is assumed that the CFD grid is capable of constituting the defined vortices in the correction.

In this section, different actuator resolutions are tested with a constant projection width, $\epsilon = 5\Delta$, and the resulting normal and tangential loadings are shown for the Phase VI rotor in Fig. 4.14 and the 5MW rotor in Fig. 4.15. For this work, a CFD grid that corresponds to 20 grid points per rotor blade is used in both cases. The actuator spacing, da, is taken as 2Δ, Δ and 0.5Δ, where Δ is the maximum CFD grid spacing in the domain.

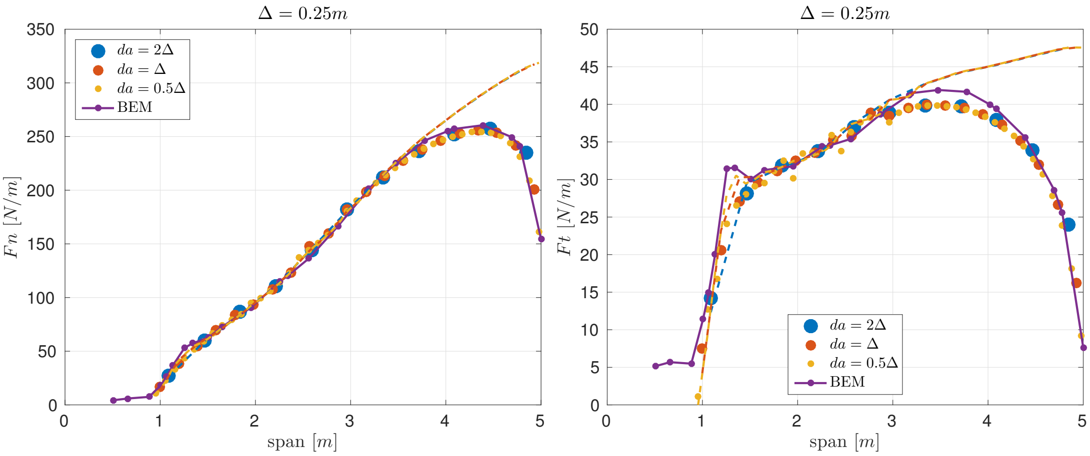

Figure 4.14: Comparison of normal and tangential loadings from ALM with and without the correction, and BEM computations for NREL Phase VI turbine with varying actuator spacing, *da*, parameter.

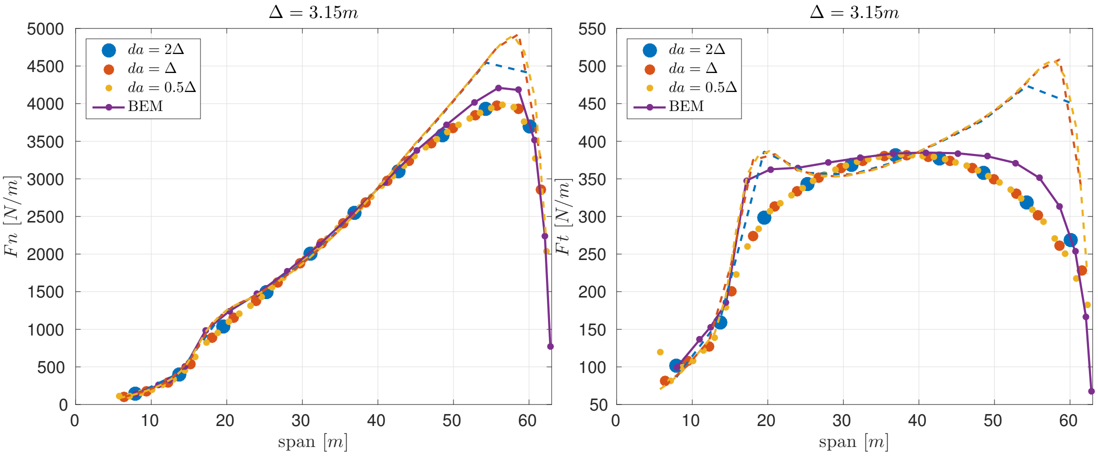

Figure 4.15: Comparison of normal and tangential loadings from ALM with and without the correction, and BEM computations for NREL 5MW turbine with varying actuator spacing, *da*, parameter.

It can be concluded from the figures that both of the results, with and without the correction, are consistent in itself. However, there is a visible oscillation in tangential loading distribution of the Phase VI turbine for actuator grid spacing $da = 0.5\Delta$.

4.3.3 Varying CFD grid resolution

To test the effect of the CFD grid resolution, simulations were conducted with coarse and fine CFD grids by keeping the projection width constant. The actuator spacing used in this study is taken as equal to the grid size Δ. Three different resolutions that correspond to 10, 20 and 30 points per blade for both rotors were tested. The results are shown in Fig. 4.16 and Fig. 4.17 for the Phase VI and the 5MW rotors, respectively.

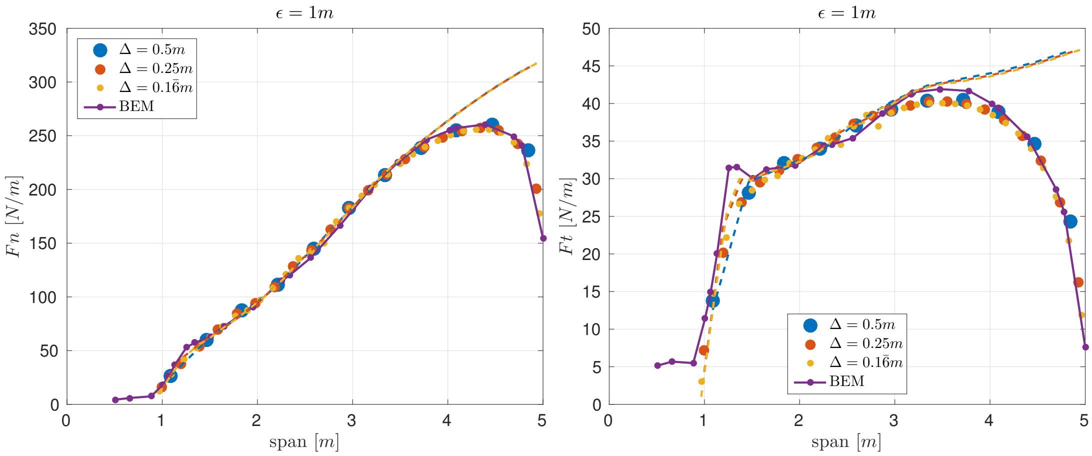

Figure 4.16: Comparison of normal and tangential loadings from ALM with and without the correction, and BEM computations for NREL Phase VI turbine with varying CFD grid resolution.

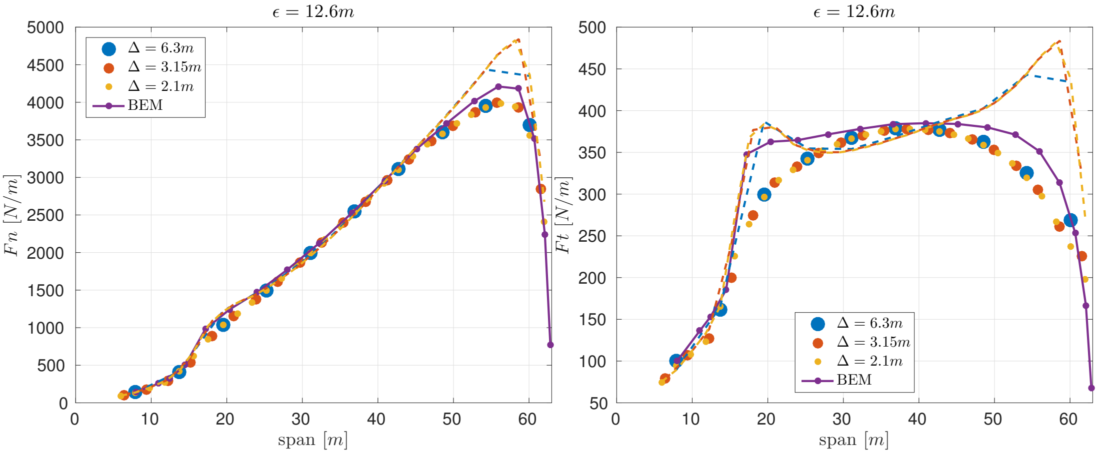

Figure 4.17: Comparison of normal and tangential loadings from ALM with and without the correction, and BEM computations for NREL 5MW turbine with varying CFD grid resolution.

It can be concluded that the results are CFD grid independent for a constant ϵ parameter. However, there is visible oscillation for tangential loading distribution for the Phase VI turbine with the finest resolution, which corresponds to relatively large $\epsilon/\Delta = 6$.

4.3.4 Varying the helical pitch

As explained in previous sections, the position of the wake vortices are needed to apply the correction. In this part of the work, a helical wake sheet with a constant pitch is used for the wake vortices. To define the helical pitch, an azimuthal averaged axial induction factor is employed with the incoming wind speed and rotational speed of the rotor. Remember that the assumption made here is that the azimuthal averaged axial induction factor increases linearly towards the tip. Further, the results are expected to change by changing the offset or the slope of this linear increase. To define the magnitude of this effect, three different linear axial induction factor distributions are used to generate the wake that is used for the correction, and results are compared against each other and BEM computations. For this study, the CFD grid employed corresponds to 20 grid points per blade and the projection width used is $\epsilon = 3\Delta = 0.75$ m and $\epsilon = 3\Delta = 9.45$ m for the Phase VI and 5MW rotors, respectively.

In Fig. 4.18 below, different distributions of averaged axial induction factors are shown and plotted against the corresponding turbine's averaged axial induction factors from BEM computations. Until this point, the distribution (b) was used for all the simulations.

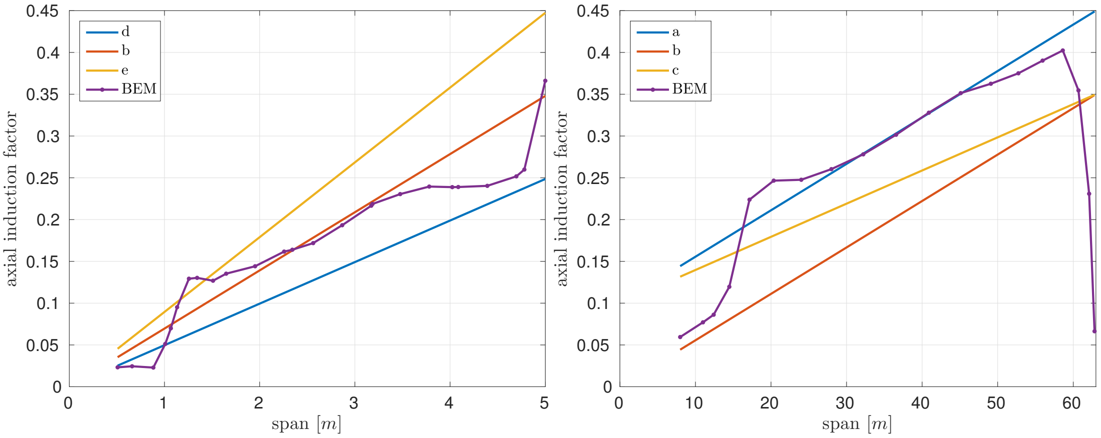

Figure 4.18: Comparison of averaged axial induction distributions over the span that are used in this study for the Phase VI rotor(Left), and the 5MW rotor(right).

The distributions (d),(b) and (e) are used for the Phase VI rotor for both normal and tangential loadings with the wake defined by using these distributions plotted against the BEM computations in Fig. 4.19.

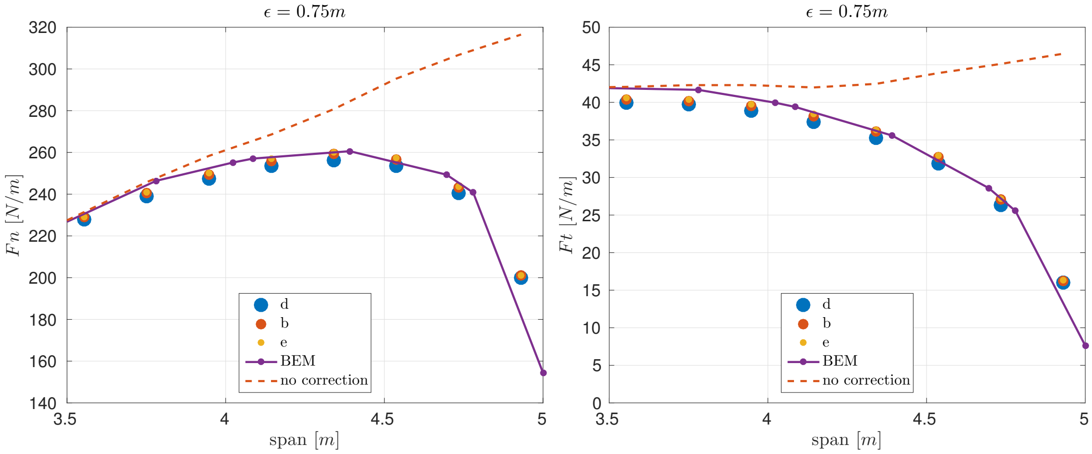

Figure 4.19: Comparison of normal and tangential loadings from ALM with and without the correction, and BEM computations for NREL Phase VI turbine with varying CFD grid resolution.

It can be seen from the figure that the correction does not show significant difference by changing the averaged induction factor, and both normal and tangential loadings are very close to the BEM computations at the tip region. Further, a similar case study was conducted for the 5MW rotor and comparisons are shown in Fig. 4.20.

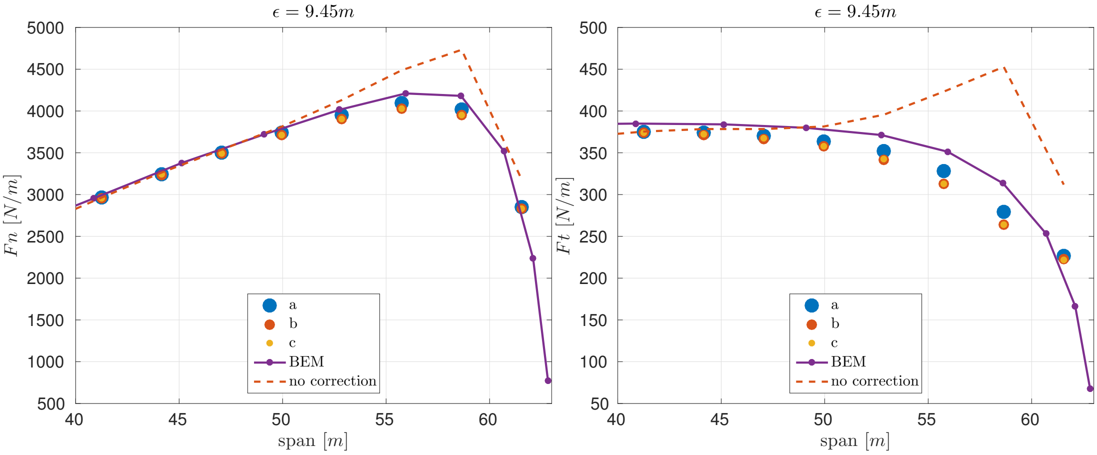

Figure 4.20: Comparison of normal and tangential loadings from ALM with and without the correction, and BEM computations for NREL Phase VI turbine with varying CFD grid resolution.

It can be said that the correction on 5MW rotor is slightly more sensitive to the averaged axial induction value. However, it should be noted that the setting (a), which is the closest to the BEM-computed axial induction values, gives the closest results to the BEM loadings.

It can be concluded from this section that there is a slight importance in the pitch of the helical wake. For further studies, one can also obtain the azimuthal averaged axial induction factor from CFD computation and vary the parameter on the fly for local flow and operating conditions.

4.4 Decambering correction - rotor application

In this section, comparisons for decambering correction, which is applied on the top of the viscous core correction, are presented for both NREL 5MW and Phase VI rotors. Two different CFD grid configurations, which correspond to 10 and 20 grid points per blade, are used for both rotors. As used in the wing case, MIRAS computations are again used here for comparisons. In Fig. 4.21 and Fig. 4.22 normal and tangential loading comparisons are shown for Phase VI and 5MW rotors respectively. In the figures, results from computations with both viscous core correction and decambering correction are represented as ALM^{**}, whereas computations with only the viscous core correction are shown as ALM^{*}. Additionally results from the measurement campaign of the NREL Phase VI turbine is included in the plots.

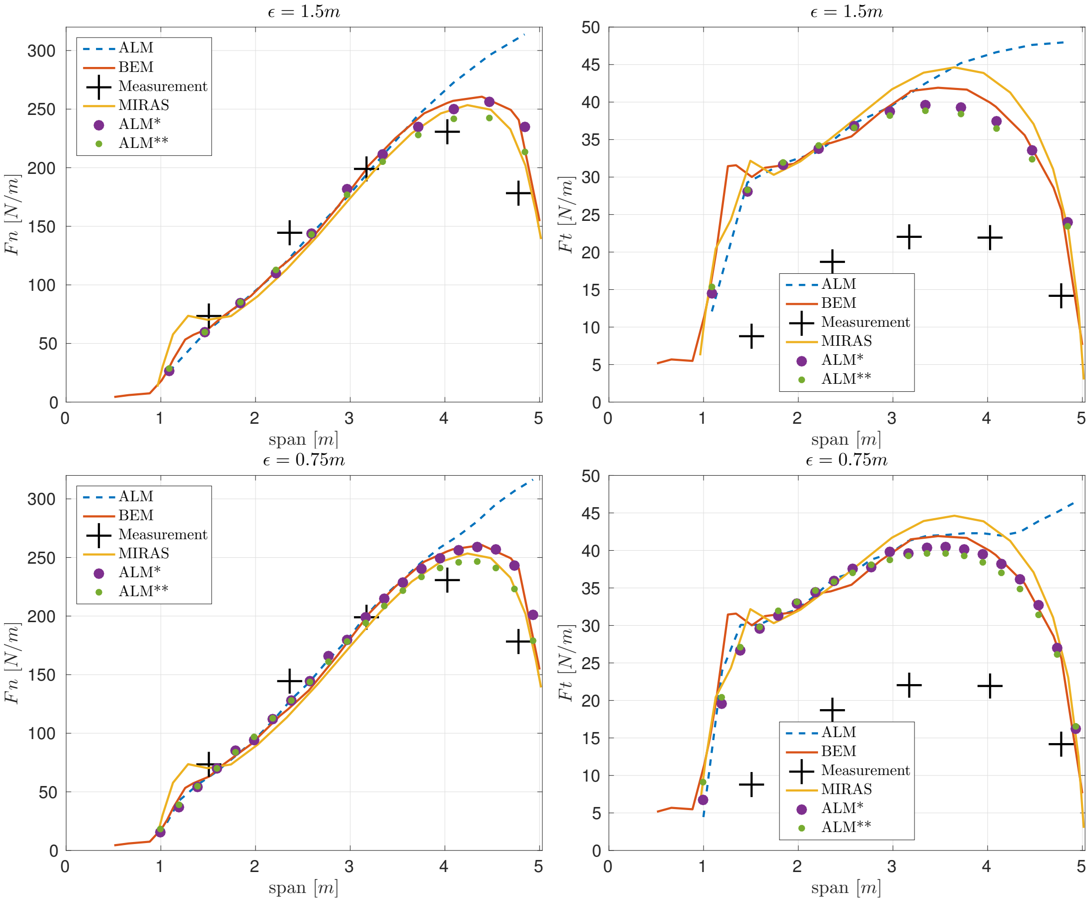

Figure 4.21: Comparison of normal and tangential loadings for NREL Phase VI rotor with applied decambering correction on the top of ALM* method.

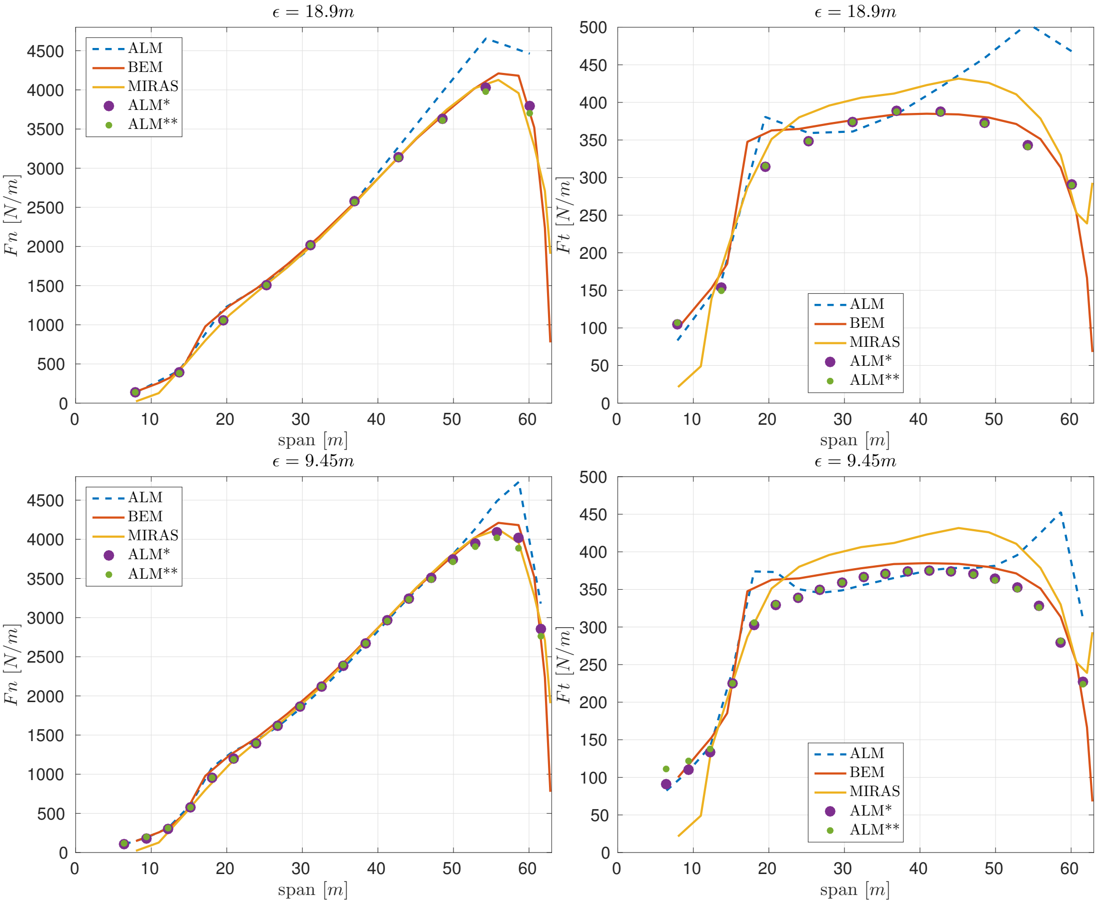

Figure 4.22: Comparison of normal and tangential loadings for NREL 5MW rotor with applied decambering correction on the top of ALM* method.

From the NREL Phase VI figures above, it is observed that even though the normal loading distributions agree with measurements, there is a significant discrepancy in between tangential loading computations and measurements. This can be due to the airfoil lift and drag curves used for the computations. Nevertheless both viscous core and decambering corrections are used to overcome the numerical error at the tip, therefore the discrepancy is considered as out of the scope of this thesis.

It is also observed that both normal and tangential loading distributions of the NREL 5MW rotor does not show significant changes with applied decambering correction. For the Phase VI rotor, due to the blade profile, some drop in the normal loadings occur around the tip region as expected. It can be concluded from the figures that, for the NREL 5MW rotor, decambering correction is not needed. Nevertheless, for the Phase

VI rotor, considering MIRAS normal loadings as more realistic, it can be said that there is an improvement in normal loadings with the applied correction.

For tangential loadings, MIRAS computations show relatively large loadings in comparison with BEM results, though, the normal loadings are matched. This suggests a clue that the drag coefficients from 2D polar data which is used both for actuator line and BEM computations might not be in line with the ones that are produced in MIRAS computations. Further, at the tip region of the NREL 5MW blade, there is a tangential loading jump in MIRAS computations, while this jump does not exist in normal loadings. Since normal loading is based mainly on the lift force and tangential loading is a combination of the lift and drag, it can be said that there is a sudden drag drop at the tip region in MIRAS, which is questionable.

4.5 Parameter study on NREL 5MW rotor - turbulent inflow

As discussed in previous pages, viscous core correction as applied here, relies on assumptions that may fail in a turbulent state. First, it is accepted that the discrete solution of Navier-Stokes equations represents a continuous wake vortex sheet. Second, with the analogy to the lifting-line technique it is assumed that the prescribed discrete wake vortices would represent the exact induction (at actuator line points) from the continuous wake vortex sheet, which then allowed us to remove the viscous core effects. Third, due to the simplifications made, the defined discrete vortex lines in the wake are assumed to trail downstream with a constant helical pitch and constitute a constant circulation strength with disregarded vortex roll-up effect. In the previous sections, it is concluded that these assumptions hold to the extent that the calculated loadings are acceptably consistent within each other in different conditions. However, a slight sensitivity was also observed in the results by using different helical pitch lengths for the NREL 5MW turbine.

On these grounds, it is reasonable to argue that the method may produce inconsistent results and require a better prescription of the discrete wake vortices in turbulent flow, where both the constant circulation strength and the constant helical pitch assumptions are strictly invalid due to the unsteadiness of the flow conditions. To enlighten this issue, the NREL 5MW rotor is subjected to a fully developed boundary layer inflow and the results obtained are presented in the following sections. The section is divided into two parts where in the first part the variations of the results are presented from the turbine's perspective, and in the second, the changes in the flow field and wake recovery are investigated.

4.5.1 Details of the simulation cases

The domain used in this study is of the size of $[L_x \ L_y \ L_z] = 1512 \times 504 \times 480$ m, with x, y and z being the streamwise, spanwise and vertical axes respectively. The streamwise length of the domain corresponds to $12D$, with $D = 126$ m being the rotor diameter. Two different CFD grid resolutions, $[N_x \ N_y \ N_z] = 240 \times 80 \times 160$ and $480 \times 160 \times 320$ are employed for this work. The physical time duration of the simulations are fixed at $600s + t_0$, with t_0 being the time it takes the turbine wake to reach to the start of the fringe region. A time step limitation is applied for all the cases where Δt is set to a smaller value then the time it takes for the tip of the turbine blade to travel a length of Δz (the grid spacing on the vertical axis). The rotor operating conditions of the NREL 5MW turbine is used as in the previous chapter (see Table 4.1). The rotor center is positioned at $z = 90$ m height and 2D downstream from the inlet, considering the horizontal periodicity, is the distance from the end of the fringe region that has a length of 0.15×1512 m. This setup results in just over $8D$ of useful domain length for the turbine wake to develop. The flow initialization is made with a snapshot from a precursor simulation, which is also employed in the background to synchronously feed the inflow of the physical domain via the fringe region. In the precursor domain, a P-controller is employed on the streamwise pressure derivative to drive the flow which is based on the spatially averaged velocity at the hub height, and the physical domain is driven only with the fringe forcing. For both precursor and physical domain simulations, the same solver settings are used. The visualization of the flow field for u, v and w velocity fields are shown in Fig. A.1, A.2 and A.3 respectively.

The development of the boundary layer is obtained by using the higher resolution domain with a roughness height of $0.1m$. The initialization of the both grid settings for both physical and precursor domains are done with the same last snapshot obtained from the developed boundary layer simulation. To initialize the coarse grid simulations, velocity interpolations from fine to coarse grid are done with second order and spectral interpolations on vertical and ground parallel axes, respectively. For $600s$ of simulation duration, streamwise and lateral averaged velocity $\bar{U}(z)$, and turbulence intensity $TI(z) = \frac{\sqrt{1/3(\overline{u(z)'^2}+\overline{v(z)'^2}+\overline{w(z)'^2})}}{\bar{U}(z)}$ are calculated from the precursor domain and shown in Fig. 4.23.

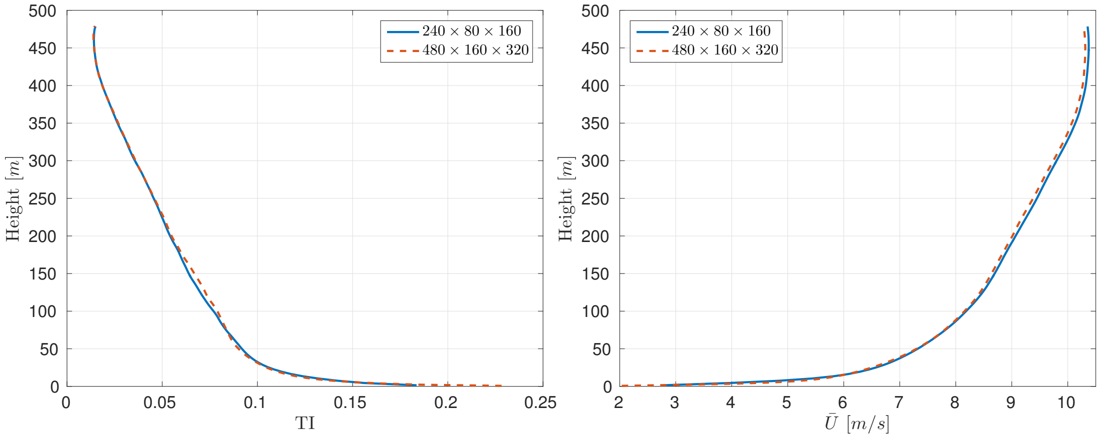

Figure 4.23: Turbluence intensity(left) and mean velocity(right) distributions with height.

To apply the viscous core correction, an average axial induction factor has to be picked to define the constant helical pitch for the discrete wake vortices. As applied with BEM methodology in the previous chapter (see Fig. 4.18), the averaged axial induction at rotor plane is obtained from the CFD simulations, as given in Eq. 4.7. It must be noted that to take the shear effect into account, the axial induction factor is calculated relative to the averaged hub velocity, $\overline{U_{hub}}$.

$$\overline{a(z)^*} = \frac{\overline{U_{hub}} - \overline{U(z)}}{\overline{U_{hub}}} \tag{4.7}$$

For different ϵ parameters and grid resolutions the average obtained axial induction values are plotted against height in Fig. 4.24.

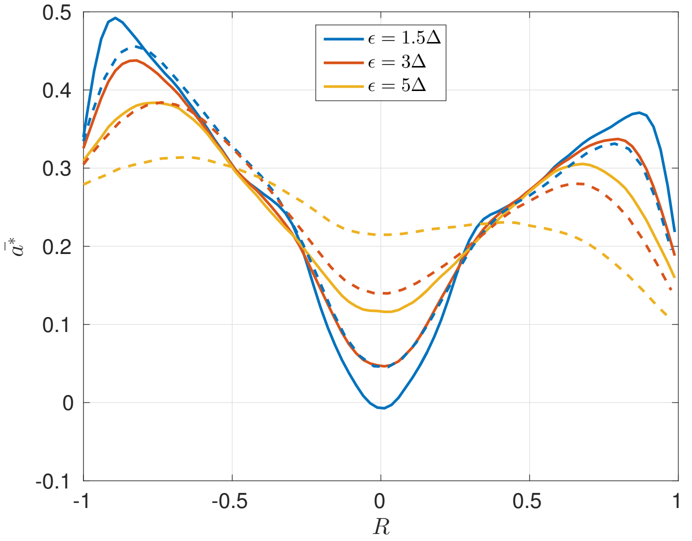

Figure 4.24: Averaged axial induction relative to the hub height velocity. $\Delta = 3.15m$(solid lines), $\Delta = 6.3m$(dashed lines)

Due to the shear effects, the resulting value at the negative R (lower height) region are relatively larger, as expected. Furthermore, there is a visible trend towards higher induction at the tip region with decreased ϵ parameter. From the BEM results, a similar distribution was obtained as presented in the previous chapter. On these grounds, a linear distribution of the averaged axial induction factor is selected to define the constant helical pitch, where the values are picked as $\bar{a}^* = 0.45$ at the tip and $\bar{a}^* = 0.1$ at the root. This results in the distribution type (a) in Fig.4.18.

In the following sections, changes in the rotor loadings and flow field based on varying projection width and grid resolution are presented. The results shown here are 600s averaged values under given flow conditions.

4.5.2 Turbine perspective

The aim in this section is to report the variations observed in the blade loadings while changing the projection width and the CFD grid resolution. First, the blade loading changes by changing ϵ parameter is shown with different grid settings. Further, by keeping the ϵ at a constant, CFD grid size is modified and results are compared. In the plots presented throughout this section, line types are used to differentiate ALM from correction applied ALM computations. The dashed line type is used for the non corrected ALM and dot-lines are used for the correction applied ALM computations. Additionally, same color coding is used for both dots and dashed lines which share the same value for the parameter that is being varied in the corresponding plot.

4.5.2.1 Blade loading change with respect to varying ϵ parameter

The $600s$ averaged blade normal and tangential loading distributions are plotted in Fig. 4.25 and in Fig. 4.26 for $240 \times 80 \times 160$ and $480 \times 160 \times 320$ CFD grid resolutions respectively. For both grids, actuator spacing is set to Δ value, which is the grid size on both the x and y axes.

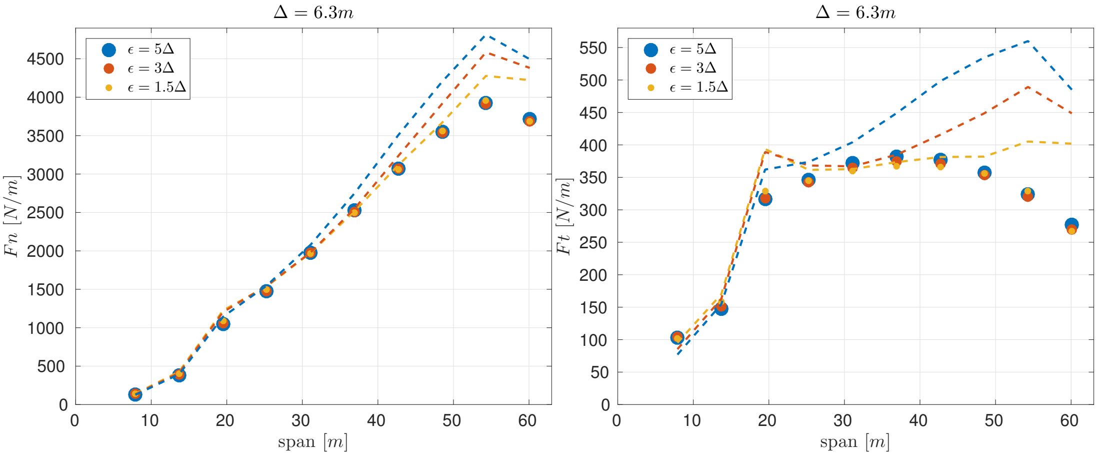

Figure 4.25: Time averaged normal(left) and tangential(right) loading distributions for NREL 5MW turbine blade operating in turbulent and shear flow in domain $[N_x\ N_y\ N_z] = 240{\times}80{\times}160$.

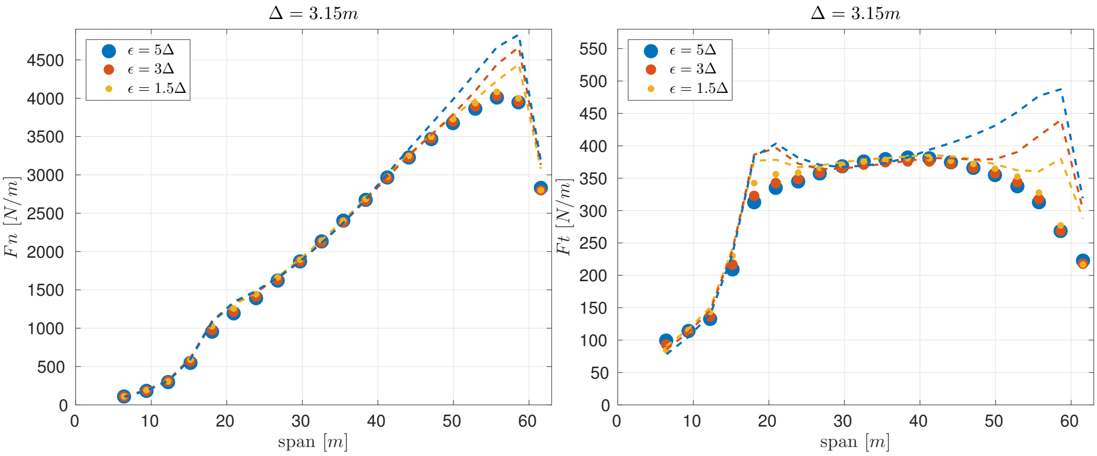

Figure 4.26: Time averaged normal(left) and tangential(right) loading distributions for NREL 5MW turbine blade operating in turbulent and shear flow in domain $[N_x\ N_y\ N_z] = 480 \times 160 \times 320$.

For both grids, in comparison with the ALM results, it can be seen that the correction applied results are relatively consistent within each other. The largest variation is observed in the tangential loadings for the finer grid setting where a change in the order of 4% and 8% are visible around the root and the tip regions respectively.

4.5.2.2 Blade loading change with respect to varying CFD resolution

It was observed from the comparisons made in the previous chapter that while keeping the projection width constant, varying CFD resolution does not result in variation of the loading distribution (see Fig. 4.16 and Fig. 4.17). To investigate this under current conditions, the turbine is subjected to the similar inflow with forces being projected by using the same ϵ size under two different CFD grid resolutions. The resulting $600s$ averaged normal and tangential loading distributions are presented in Fig. 4.27.

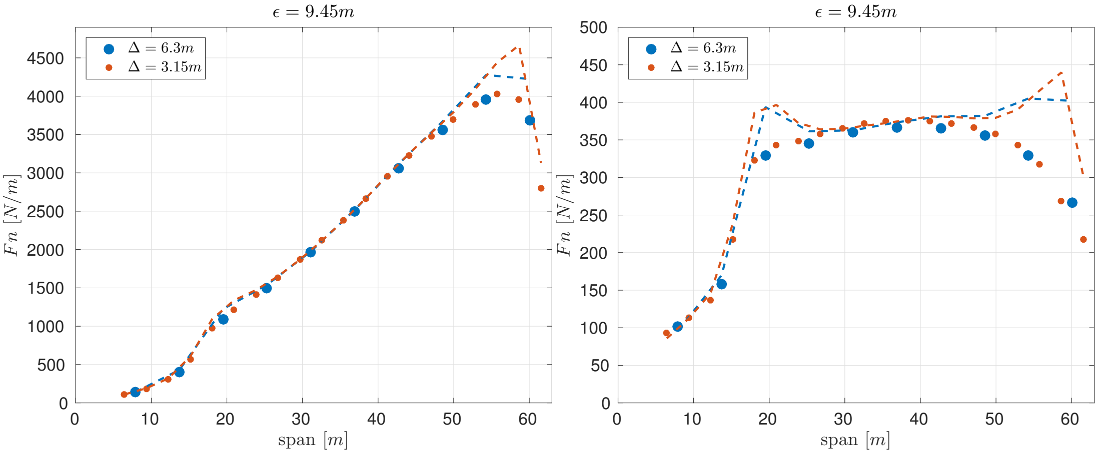

Figure 4.27: Time averaged normal(left) and tangential(right) loading distributions for NREL 5MW turbine blade operating in turbulent and shear flow in domain $[N_x\ N_y\ N_z] = 480 \times 160 \times 320$.

First, its is clear from the comparisons that the ALM without correction results in the same load levels for both normal and tangential loadings at the inner regions of the blade. It can be concluded that neither the averaged axial induction nor the mean velocity is affected by the grid resolution. Further, it can be observed that both at the tip and inner regions of the blade, the normal loading distributions obtained from the ALM with correction computations are similar. However, for the tangential loadings, coarser grid simulation with correction results in slightly lower load levels at the inner blade regions, whereas results from ALM without correction does not show any variations at the same region.

4.5.2.3 Total power and thrust change with respect to varying ϵ parameter and CFD resolution

In this part, rotor performance by means of total power and thrust is evaluated for the simulation cases that are used in this chapter, and presented in the Table 4.2. In the table, number of actuator points used per blade length (also the number of cfd grid points per blade) is represented by $nrPnts/b.$, the projection width with units of grid length is shown as ϵ^*, the vcc parameter represents the viscous core correction and $cpuCost$ is relative units of cpu time required to obtain the corresponding results. Furthermore, the evaluated loading distribution in each row refer to the corresponding figure in the $dataFig.$ column.

$nrPnts/b.$	$\Delta[m]$	$\epsilon^*[\Delta]$	ϵ[m]	vcc	cpuCost	P[MW]	T[kN]	data Fig.
10	6.3	5	31.5	-	1	2.33	395	4.25
10	6.3	3	18.9	-	1	2.07	377	4.25
10	6.3	1.5	9.45	-	1	1.89	364	4.25,4.27
20	3.15	5	15.75	-	16	2.00	371	4.26
20	3.15	3	9.45	-	16	1.88	362	4.26,4.27
20	3.15	1.5	4.725	-	16	1.83	359	4.26
10	6.3	5	31.5	✓	1	1.70	345	4.25
10	6.3	3	18.9	✓	1	1.68	345	4.25
10	6.3	1.5	9.45	✓	1	1.68	346	4.25,4.27
20	3.15	5	15.75	✓	16	1.70	346	4.26
20	3.15	3	9.45	✓	16	1.70	347	4.26,4.27
20	3.15	1.5	4.725	✓	16	1.74	351	4.26

Table 4.2: Total power and thrust values for different simulation cases

It can be seen from the table that the correction applied ALM computations result in fairly consistent total thrust and power values. In addition, the correction applied results are lower than all of the ALM method computations for both the total power and thrust.

4.5.3 Flow field perspective

In this section, the change in wake recovery and the effect on the three velocity components inside the wake are investigated by varying the projection width and the CFD grid resolution. In the plots presented throughout this section, a dashed line type is used for the non-corrected ALM and solid line type is used for the correction applied ALM computations. Additionally, as used previously, the same color profile is used for the lines that share the same value for the parameter that is being varied in the corresponding plot.

4.5.3.1 Wake deficit change with respect to varying ϵ parameter

First, the averaged relative velocity is obtained as $U_{avg}/U_0 = \frac{1}{D}\int\limits_{-R}^{R} \overline{U(z)/U'(z)}dz$, where $U(z)$ represents the streamwise velocity at height z and $U'(z)$ is the velocity at the same spatial point and time but without a turbine. Furthermore, the overline is used to represent an averaging operation in time. The resulting averaged relative velocity is plotted in Fig. 4.28 with respect to downstream distance from the hub.

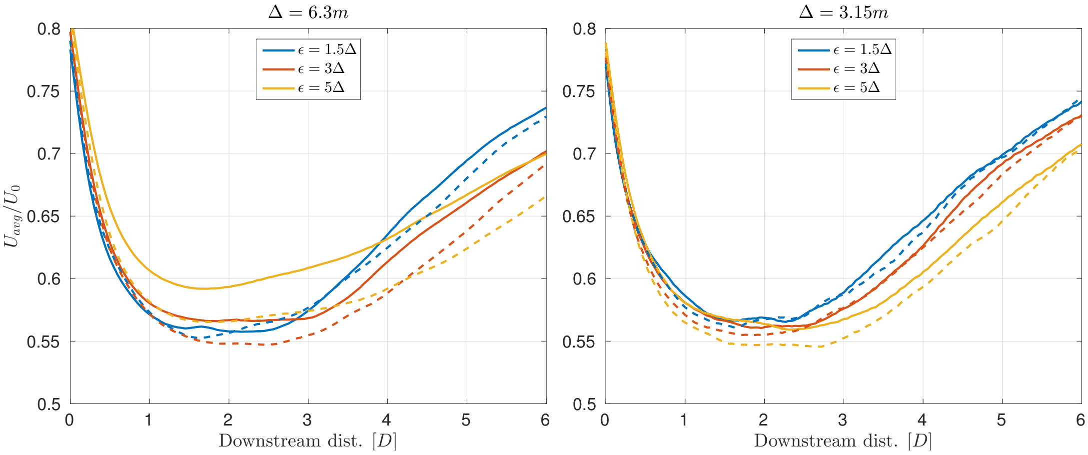

Figure 4.28: Averaged relative velocity versus downstream distance from the hub by using different projection and CFD grid resolutions ($[N_x\ N_y\ N_z] = 240 \times 80 \times 160$(left), $480 \times 160 \times 320$(right)).

It can be seen from the figure that there is a trend of a faster velocity recovery with decreased ϵ parameter. In both cases, applied correction also results in a faster recovery and the effect is relatively stronger in the coarser grid. Generally speaking, it is observable that the resulting recovery is dependent on the used projection width. Nevertheless, by comparing two figures, it can be seen that projection width of $\epsilon = 9.45m$ cases result with similar recovery speeds.

In order to have a more detailed comparison, velocity deficit as a function of height at different downstream distances are plotted in Fig. 4.29 and Fig. 4.30 for coarser and finer CFD grid settings respectively.

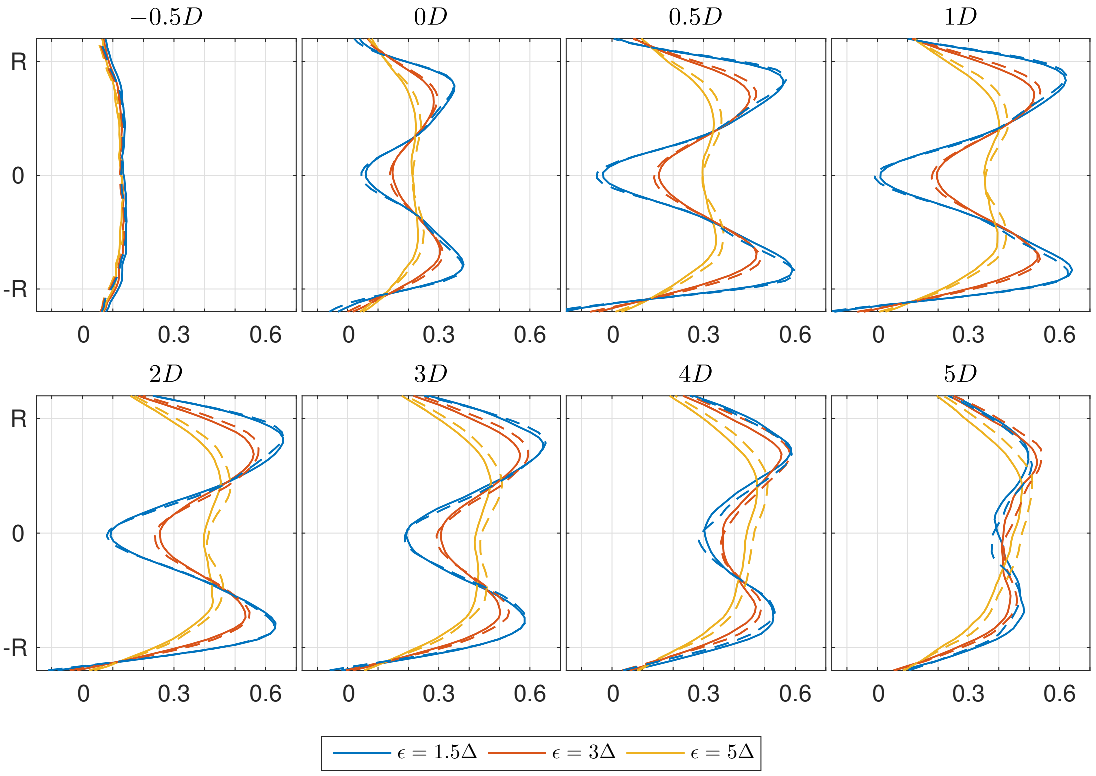

Figure 4.29: Velocity deficit as a function of height with different ϵ parameters plotted at different downstream distances from the hub position for the CFD grid resolution of $[N_x\ N_y\ N_z] = 240 \times 80 \times 160$.

From the figures, it is observed that the near wake velocity profile is very dependent on ϵ parameter. In the near wake, smaller ϵ values cause the induction to dramatically increase close to the outer region of the wake and to decrease around the center regions. Furthermore, the effect of the viscous core correction is relatively small in comparison with the observed change by varying the ϵ parameter. Nevertheless, with low ϵ values, there is a slight smoothening effect at the near wake due to the correction. Additionally, for the $\epsilon = 5\Delta$ case with the coarse grid, there is considerable difference that still exists at the $5D$ downstream position, which is also visible in Fig. 4.28.

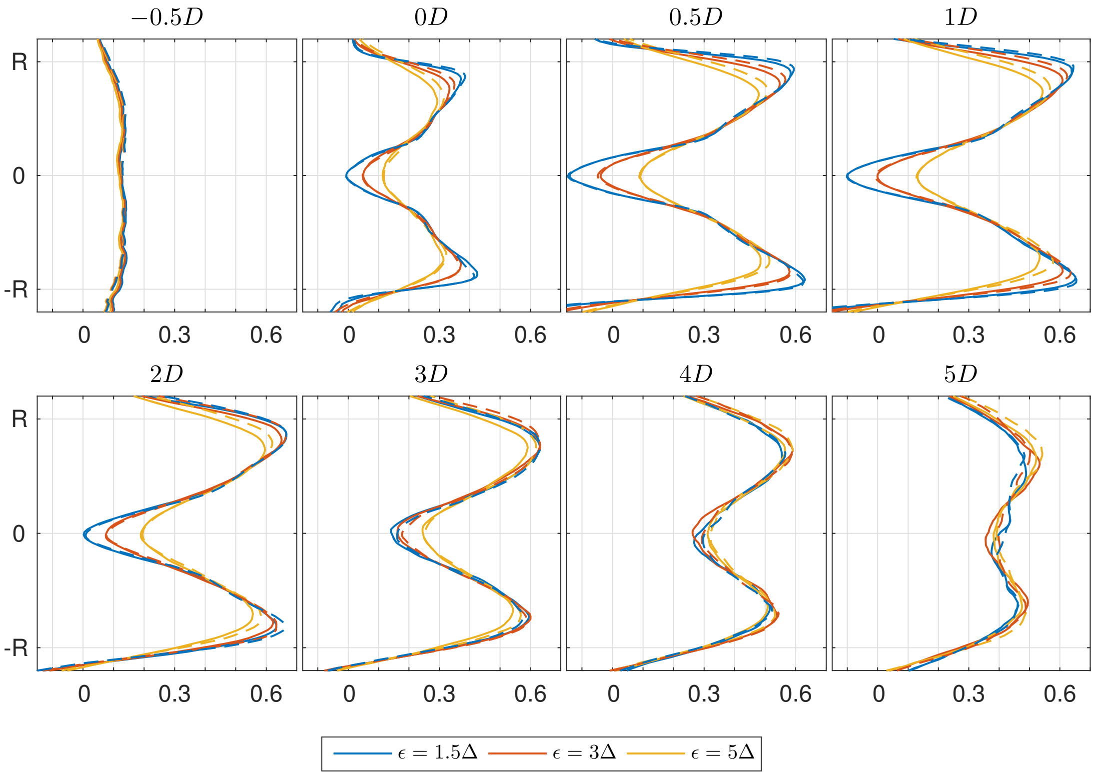

Figure 4.30: Velocity deficit as a function of height with different ϵ parameters plotted at different downstream distances from the hub position for the CFD grid resolution of $[N_x \ N_y \ N_z] = 480 \times 160 \times 320$.

4.5.3.2 Wake deficit change with respect to varying CFD grid resolution

In this part of the study, the same projection width $\epsilon = 9.45$ m is used under two different CFD grid resolutions and wake deficits obtained at various downstream distances are compared. The given projection width corresponds to $\epsilon = 1.5\Delta$ and $\epsilon = 3\Delta$ for the coarser and the finer grid settings respectively.

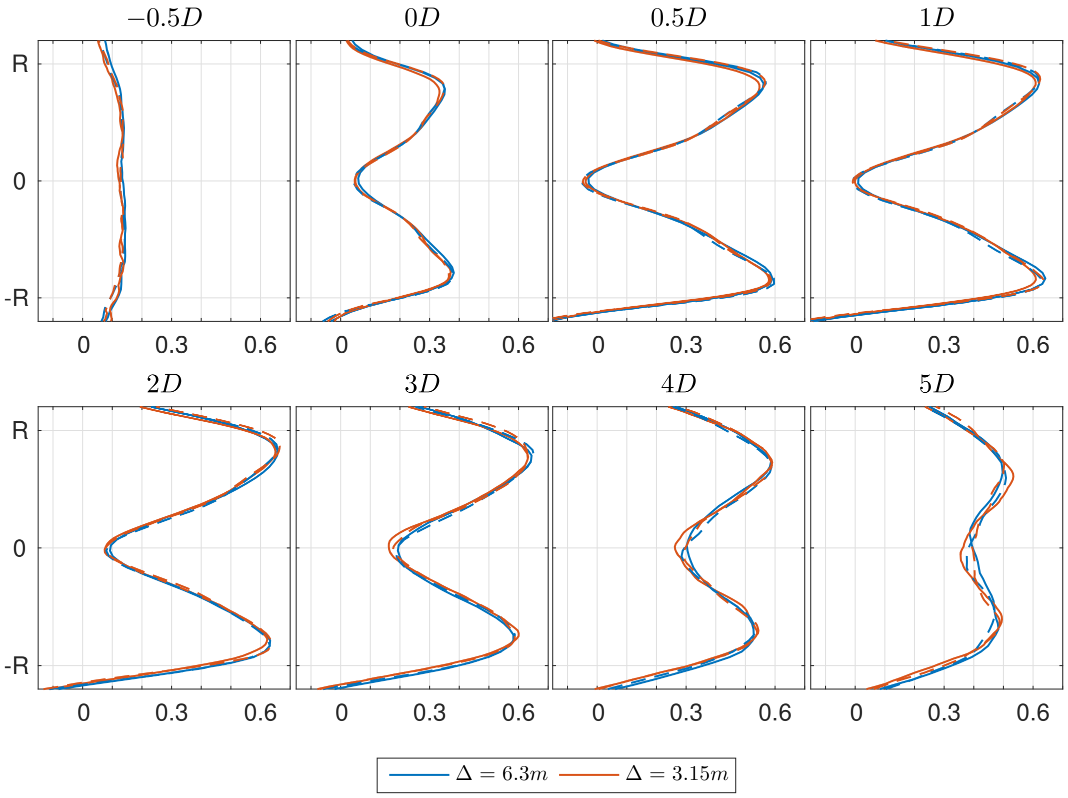

Figure 4.31: Velocity deficit as a function of height with two different CFD grid resolutions plotted at different downstream distances from the hub position for $\epsilon = 9.45$ m.

In the previous tests, it was seen that CFD grid resolution change did not cause the results to vary. A similar result can be seen in Fig. 4.28, that the same projection width results in the same wake recovery rate at different downstream and radial position in the wake, especially in the near wake region.

4.5.3.3 Effect of the correction on 3-velocity components inside the turbine wake

To obtain an intuitive understanding of the effect from the viscous core correction, the 600s time averaged change on velocities inside the near wake region is plotted in rotor parallel slices in Fig. 4.32. The colorbar represents the velocity difference as $U_{ALM^*} - U_{ALM}$ in units of $[m/s]$, where U_{ALM^*} represents the velocity obtained from the correction applied ALM computation and U_{ALM} is the velocity from ALM computation without the correction. For the comparison, the $\epsilon = 3\Delta$ case with the coarser CFD grid is used to have a relatively strong effect with respect to the random behavior from the background turbulence.

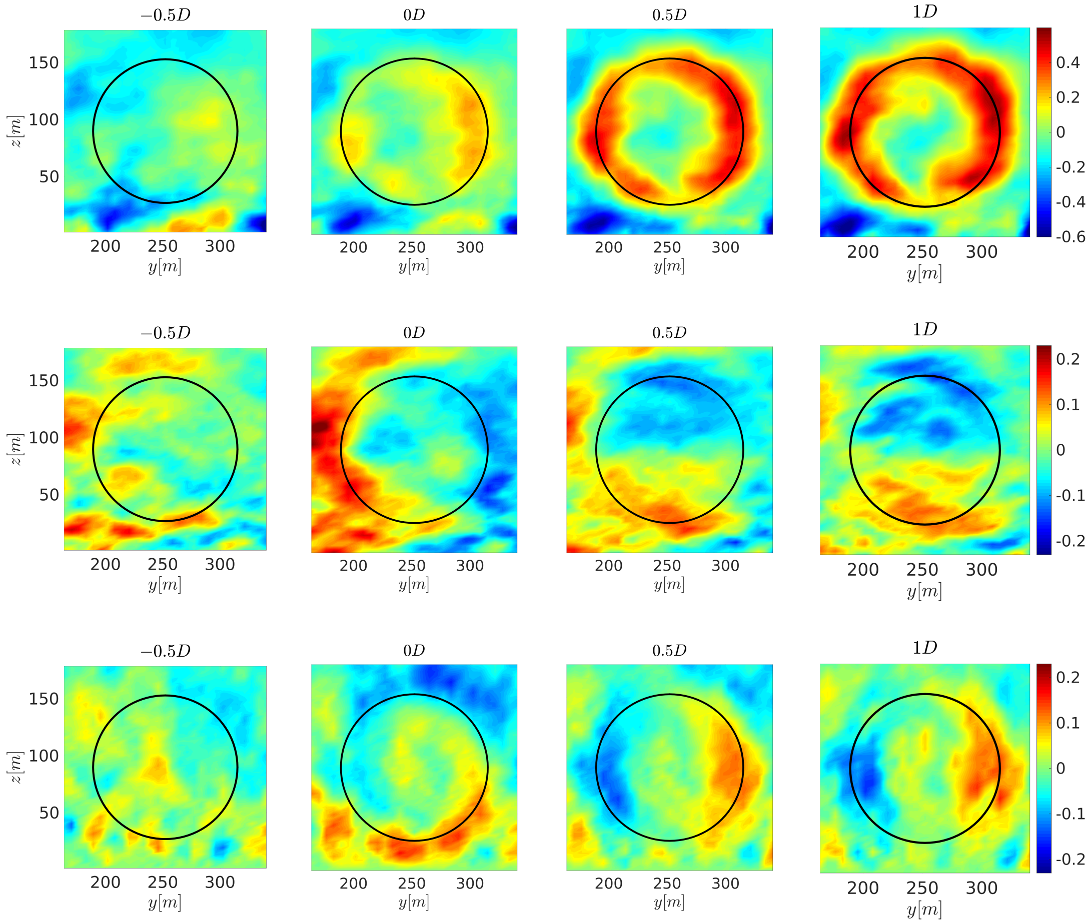

Figure 4.32: Time averaged difference in velocity between corrected and normal ALM. Δu(top), Δv(middle) and Δw(bottom) velocities at different downstream distances relative to the position of the turbine hub. The black circle represents the rotor area projection on to the corresponding slice.

The largest change is seen on streamwise velocity in 1D downstream distance. The slices in further downstream positions are not plotted here since the effect was less and less visible further downstream. At the outer region of the wake there is a considerable increase on u velocity. This can be explained by the fact that, due to reduced normal loadings at the tip region, the convecting tip vortex is weaker, then in the near wake induction is less. Further, from both v and w velocities, it can be seen that at the rotor plane ($0D$) slices, correction applied wake expands less which is also in-line with increased streamwise velocity (due to the conservation of mass). In further downstream for v and w velocities, there is an added rotation effect to the wake which is visible. However, the rotation velocity is relatively small.

Chapter 5

Discussion, conclusion and future work

Two milestones have been achieved in this project. The first one is the development of a new pseudo-spectral flow solver which is currently avaliable in the DTU Wind Energy's git repository. The second is the investigation of the ALM for wind turbine forcing in CFD simulations, which resulted in a new correction methodology that greatly improves blade loads. The new technique is currently available for use in the new code and will be implemented in the EllipSys3D flow solver in the near future.

In the development part of this thesis, a new highly-parallel pseudo-spectral flow solver has been developed. The new code is designed to be portable, user/developer friendly, and it does not depend on any external library other than FFTW (see Frigo & Johnson (2005)) which is used extensively for the FFT operations and memory allocations in the solver. The source code is developed in *Fortran 90* environment and post-processing routines are made avaliable in *Matlab* language. For flow visualization purposes a parallel *ParaView* (see Hansen & Johnson (2011)) file format, *.pvti, is used which allows each core to output the requested variable without a global merge. Additionally, the scaling performance of the code is tested under different flow cases and it can be concluded that the code scales linearly down to 0.1-1 wall-seconds per time step range. At the current stage, the new code is ready to serve for wind energy research in many different areas. Recently, the code was employed as a boundary layer flow solver for wind turbine noise research where the 3D velocity field with turbine wake was extracted in different snapshots and used as an input for an in-house wind turbine noise propagation model (see Barlas *et al.* (2017a,b)).

During three years of the PhD study, more than half of the time went into the development part of the flow solver. However, the main focus of the project was to investigate the ALM which, by default, produced inconsistent loadings that varied depending on the resolution/force projection width. With this thesis, a new correction procedure has benn introduced to overcome the numerical side-effects of the force projection in ALM. The computational cost of the new correction is almost invisible and it brings great improvement to the ALM loading distributions for both planar wings and wind turbine blades. It has been shown that, with the application of the correction, comparable loads can be obtained with grid resolutions as coarse as 10 grid points per blade and for a constant ϵ, varying CFD grid or actuator grid point resolutions does not alter the loadings. Additionally, from the integrated wake recovery plot Fig. 4.26, it can be seen that the correction causes the wake to recover faster for the same ϵ parameter, which is beneficial for the coarse grid resolution simulations where the wake recovery is often delayed due to the large projection widths.

In rotor studies for ALM correction, it was seen that the helical pitch change in the prescribed wake resulted with in a visible change in the correction behavior. By comparing Fig. 4.13 and Fig. 4.22, it can be concluded that results are less ϵ dependent if the helical pitch is defined in a more accurate way. Thus, one can conclude that if the correction results are ϵ dependent, the wake is not defined well. Furthermore, assumption of the wake constituted of helical vortices with a constant pitch is strictly invalid in turbulent and especially shear conditions. Nevertheless, in the last chapter, it has been shown that, in an averaged sense, the variations of the loadings by changing the projection width (see Fig. 4.25 and Fig. 4.26), are less than the overshooting of the tip loadings without the correction. Also, the CFD grid resolution comparisons in turbulent inflow showed that, although the grid resolution didn't have any effect on time averaged wake deficit, a visible change was obtained on the tangential loadings with viscous core corrections from different CFD grids (see Fig. 4.27(right)). These provide clues of a need for a better wake representation. To partially overcome this issue and improve the ALM correction to the next level, the correction technique is currently being updated where the CFD velocities are employed to define the helical pitch of the prescribed wake, instead of a predefined axial induction. In this way, the technique becomes tuning-free, since only uses the projection width as an input. The draft paper where this new update will be presented is attached to this thesis. In the paper, it can be seen that for the NREL Phase VI turbine, satisfying loading distributions are obtained with CFD resolutions as coarse as 5 grid points per blade.

In turbulent simulations, the reported loading distributions are time averaged as mentioned before. However, for the life-time equivalent loading computations, the unsteady loading responses are used by a rain-flow counting technique. Thus, one should first check the model behavior in an unsteady case and compare with a highly resolved ALM before applying the method on any fatigue research. Although current work proves that the viscous core effects are missing and can be fixed with such a simple correction, capturing the unsteady part of the viscous core effect may become troublesome. In addition to that, one could also investigate the required length of the trailing vortices for the correction to converge. As shown in Fig. 3.7 and Fig. 3.8, the correction is not effective after some distance which is a function of the viscous core size which is the ϵ parameter. Therefore, it would be interesting to check the required trailing vortex length from the turbine rotor to minimize the computational cost of the correction. It is anticipated that the required helical length to changes with respect to both the ϵ and the tip speed ratio λ.

From the development part of this thesis, it can be concluded that the simple Smagorinsky eddy viscosity model fails to capture the logarithmic slope in turbulent channel flow. This is seen from the time averaged velocity profile that high C_s values overshoot the slope, which can be explained by excessive eddy diffusion which lowers the momentum mixing. By decreasing the C_s parameter, the logarithmic slope could only be captured in a limited local height interval. As a future work, it is planned to improve this part and implement either a wall damping function or a more sophisticated eddy viscosity model such as the dynamic Smagorinsky. As discussed previously, for our current usage, the mean velocity is set by using the corresponding pressure gradient through a controller, thus a mis-transferred wall stress can not effect the mean velocity. Furthermore, it was seen from the previous chapter that the wake recovery was independent of the grid resolution for the same wind turbine forcing. Then, it can also be concluded that, the effect from the sub-grid-scale modeling is not large enough to alter the wake recovery rate. Though, from the blade loading point of view, an over estimated eddy diffusivity, may cause turbulence intensity to drop at a specific height which then would result in an underestimate of normal blade loadings.

The main focus in this thesis has been on the actuator line model which allows to capture the blade loadings. However, for power production, wake recovery or atmospheric boundary layer studies, it has been shown by many researchers that the actuator disk model produces similar results under turbulent conditions. Thus, for large domains it is reasonable to use an actuator disk instead of an actuator line to avoid finer spatial and temporal resolution requirements. Therefore, the actuator disk model is planned to be implemented in the new pseudo-spectral LES tool. Additionally, implementing the heat equation is also one of the future goals. It is known that the convective boundary layer increases the wake recovery speed for wind turbines whereas a stable boundary layer extends the wake lengths, which causes both power and loads to alter depending on the heat flux from the surface.

Regarding the CFD grid resolution, in the recent work of Martínez-Tossas *et al.* (2015), it is noted that for small ϵ values, a grid dependent power production was observed. Although, we have not conducted such a grid study for as low ϵ values as they used, in neither of our simulations (including the ones that are not reported here) the resulting power was grid dependent. This difference in behavior can be explained by the difference between spatial discretization schemes used in two different codes. The code that is used in their study is a finite volume code, whereas in our application, a spectral discretization is used for ground parallel axes and a second order finite difference for the vertical discretization. Due to the low order discretization on the vertical axis, one may expect to see a similar response in our simulations. However, in our implementation grid resolution on the vertical axis was kept at a minimum of two times finer than the resolution used in ground parallel axes and ϵ is varied based on the larger grid size. Therefore, from a grid resolve-ability perspective, this can be thought of as twice as good for the same given ϵ/Δ value.

Appendices

A.1 Visualization of the turbulent flow field

In figures below, flow field of a snap shot of NREL 5MW turbine operating in a developed boundary layer with mean wind speed of 8 m/s at hub height is shown.

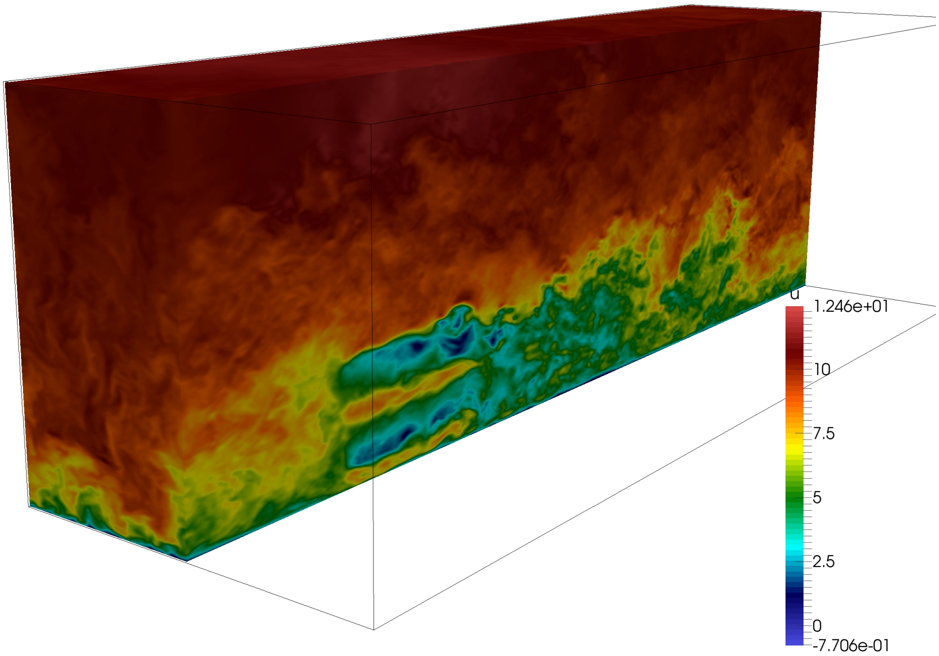

Figure A.1

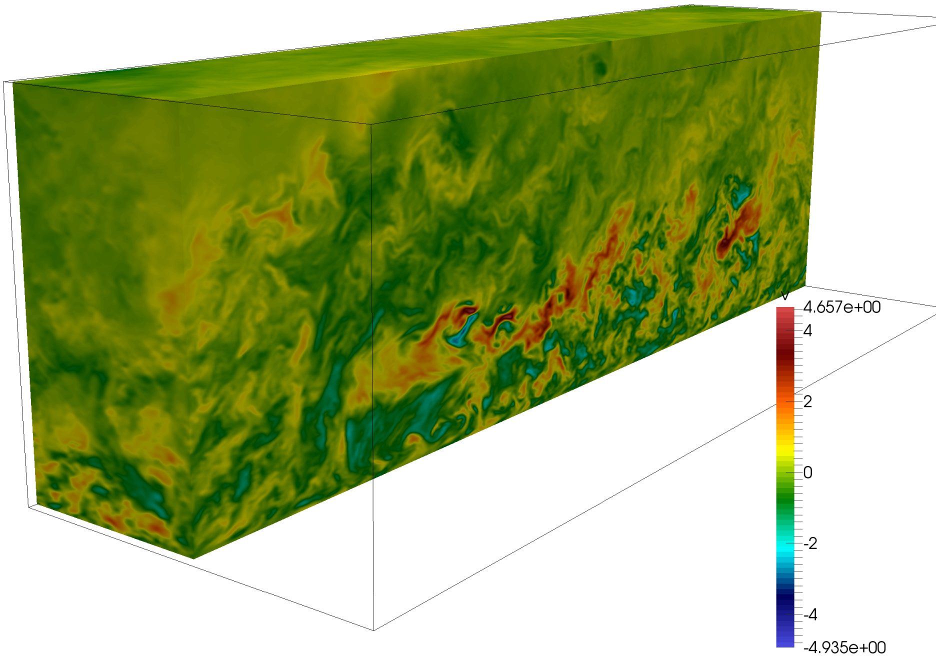

Figure A.2

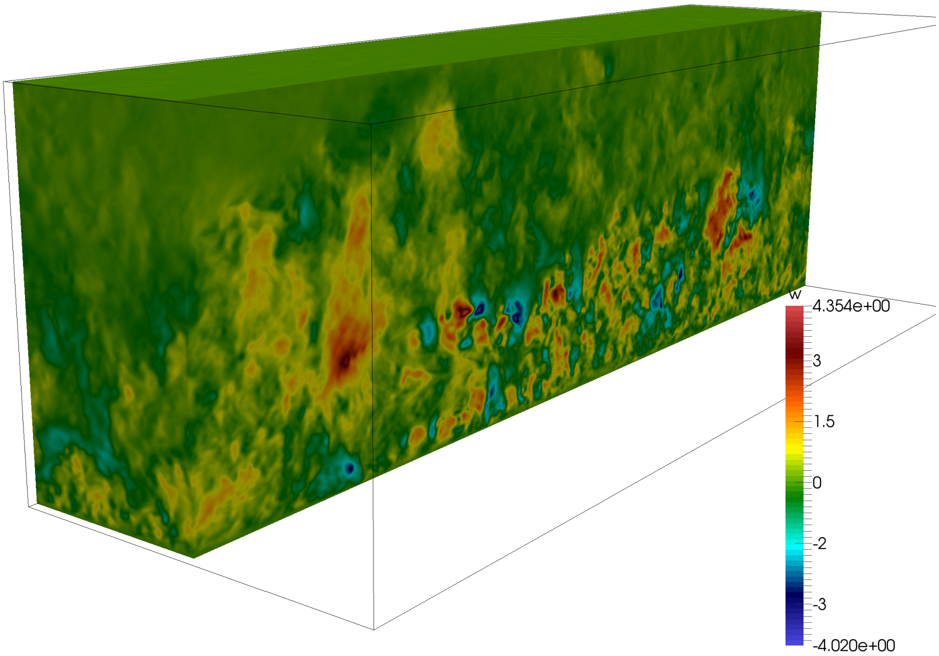

Figure A.3

A.2 Basic parameters and usage of the main user input file

In this part, a brief explanation of the parameters used in the main setup file is shown.

```
%---------------------------------------------------
%------------SIMULATION SETUP PARAMETERS------------
%---------------------------------------------------
## on the fly log output
logOutput = 0
## hardware allocations ##
number_of_cores = 200
number_of_sub_cores = 20
syncPrecursor = 0 ![simultaneous precursor simulation 0/1 ]
syncPrecursor_mpiMethod = 1 ![1:spread in each node, 2:scatter on total procs]
## physics
rho = 1.225 !1.225
mu  = 0.005599546779855 !0.001
dt  = 0.01 !0.0003 !0.0004
ttMax = 3000 !max time step
simType = 3 ![1:DNS channel, 2:LES channel w/ wallmodel, 3:LES half channel w/ wallmodel]
# if open top=0--> turn on const. pressure derivative.
## grid ##
Nx = 400
Ny = 160
Nz = 280
## physical domain lengths [m] ##
Lx = 630
Ly = 252
Lz = 216
## fringe zone ##
fringeZone = 0
fringe_relSize = 0.15
lambda_max = 50
drise = 0.6
dfall = 0.2
## wind turbine forcing ##
turbineType = 2  ![1:Nrel Phase VI, 2:NREL 5MW]
turbineForcing = 0
wingForcing = 0
epsilon = 5
smear_bubble_size = 3
logTurbData = 0
logWingData = 0
logDataFileName = 'forces3_1.dat'
## turb. modeling
Cs  = 0.18
wallModel = 1 !0:off, 1:rough surface - use z0,   2:smooth surface - use wm_E
z0 = 0.1
wm_E = 9
## save data
directory = '/SCRATCH/kdag'
folderName = 'ABL_v23'
veloSliceSave = 1
paraview_saveOffset = 0    !start saving visualization output after this time step
paraview_saveInterval = 30000  !visualization data save interval
snapshot_saveInterval = 1000000    !snapshot u,v,w save interval
## restart files
saveResFile = 1
resFileDir = '/mnt/aiolos/kdag/SCRATCH/resFiles'
readResFile = 1
```

logOutput : flag to turn on/off the terminal output record into a file.
number_of_cores : total number of allocated cores with the MPI job
number_of_sub_cores : number of cores for each ground parallel domain slice. For good scaling, shouldn't exceed Nz/10
syncPrecursor : flag to turn on/off the simulataneous precursor simulation. Requires min. 2 cores
syncPrecursor_mpiMethod = switch for distribution of the cores that are assigned to be allocated for precursor computation. Often 1 is better.

simType : defines the simulation type and enable/disable semi-implicit molecular diffusion or SGS modeling

fringeZone : switch to turn on/off fringe (buffer) region to drive the flow. Its disregarded if syncPrecursor is 1.

fringe_relSize : length of the fringe region relative to the domain length on x direction

lambda_max,drise,dfall : fringe parameters (see Eq. 2.40 and 2.41)

turbineType : a basic switch to switch rotor data input files. in the current version 2 rotors are implemented.

turbineForcing : turn on/off turbine forces (only in the physical domain incase syncPrecursor is 1)

wingForcing : a flag to turn on/off wing actuator line model. The wing geometry is hard coded yet can easily be linked to an input file.

epsilon : $\epsilon^* = \epsilon/\Delta$ value for 3d gaussian smearing.

smear_bubble_size : cut off distance for smearing.

logTurbData,logWingData : switches to log angle of attack and loading data in the log data file

Cs : Smagorinsky coefficient

wallModel,z0,wm_E : wall model switcher and required parameters. see Eq. 2.23 and 2.24

directory,folderName : all data output will be written to the provided directory/folderName location

veloSliceSave : enable/disable velocity save by slices. if set to 1, requires velocitySave.in file

saveResFile : switch to enable/disable record of the snapshots of the last and the last-1 time steps, which then will be used as an initialization

readResFile : if switched to 1, 2 time level initialization will be done with the given restart file with AB2 time scheme, else a uniform initialization with hard coded velocity

List of Figures

List of Tables

References

Akbar, M., Sharifi, A. & Porté-Agel, F. (2016). Wake flow in a wind farm during a diurnal cycle. *Journal of Turbulence*, **17**, 420–441.

Armfield, S. & Street, R. (2002). An analysis and comparison of the time accuracy of fractional-step methods for the navier-stokes equations on staggered grids. *International Journal For Numerical Methods In Fluids*, **38**, 255–282.

Barlas, E., Zhu, W.J., Shen, W.Z., Dag, K.O. & Moriarty, P. (2017a). Coupled modelling of wind turbine noise from source to receiver. *The Journal of the Acoustical Society of America*, (under review).

Barlas, E., Zhu, W.J., Shen, W.Z., Dag, K.O. & Moriarty, P. (2017b). Investigation of amplitude modulation noise with a fully coupled noise source and propagation model. In *International Conference on Wind Turbine Noise*.

Calaf, M., Meneveaueau, C. & Meyers, J. (2010). Large eddy simulation study of fully developed wind-turbine array boundary layers. *Physics of Fluids*, **22**, 015110.

Canuto, C., Hussaini, M.Y., Quarteroni, A. & Zang, T.A. (2007). *Spectral Methods Evolution to Complex Geometries and Applications to Fluid Dynamics*. Springer.

del Alamo, J.C., Jimenez, J., Zandonade, P. & Moser, R.D. (2004). Scaling of the energy spectra of turbulent channels. *Journal of Fluid Mechanics*, **500**, 135–144.

Ferziger, J.H. & Perić, M. (2002). *Computational Methods for Fluid Dynamics*. Springer.

Frigo, M. & Johnson, S.G. (2005). The design and implementation of FFTW3. *Proceedings of the IEEE*, **93**, 216–231, special issue on “Program Generation, Optimization, and Platform Adaptation”.

Grötzbach, G. (1987). Direct numerical and large eddy simulation of turbulent channel flows. In N.P. Cheremisinoff, ed., *Encyclopaedia of Fluid MechaMech Vol. 6*, vol. 6, chap. 34, 1337–1391, Gulf Publisihing Company.

Hand, M.M., Simms, D.A., Fingersh, L.J., Jager, D.W., Cotrell, J.R., Schreck, S. & Larwood, S.M. (2001). Unsteady aerodynamics experiment phase vi: Wind tunnel test confiugrations and avaliable data campaigns. Tech. rep., NREL.

Hansen, C.D. & Johnson, C.R. (2011). *Visualization Handbook*. Academic Press.

Jensen, N.O. (1983). A note on wind generator interaction. Tech. rep., Risø National Laboratory, Denmark.

Jha, P.K., Churchfield, M.J., Moriarty, P.J. & Schmitz, S. (2013). Accuracy of state-of-the-art actuator-line modeling for wind turbine wakes. In *51st AIAA Aerospace Sciences Meeting including the New Horizons Forum and Aerospace Exposition*, American Institute of Aeronautics and Astronautics.

Jha, P.K., Churchfield, M.J., Moriarty, P.J. & Schmitz, S. (2014). Guidelines for volume force distrubutions within actuator line modeling of wind tturbine on large-eddy simulation-type grids. *Journal of Solar Energy Engineering*, **136**, 031003.

Katz, J. & Plotkin, A. (2001). *Low-speed aerodynamics*. McGraw-Hill.

Lamb, H. (1932). *Hydrodynamics, 6th ed.*. Cambridge University Press.

Larsen, G.C., Madsen, H.A., Bingöl, F., Mann, J., Ott, S., Sørensen, J.N., Okulov, V., Troldborg, N., Nielsen, M., Thomsen, K., Larsen, T.J. & Mikkelsen, R. (2007). Dynamic wake meandering modeling. Tech. Rep. Risø-r–1607, Risø National Laboratory, Denmark.

Lele, S.K. (1992). Compact finite difference schemes with spectral-like resolution. *Journal of Computational Physics*, **103**, 16–42.

Martínez-Tossas, L.A., Churchfield, M.J. & Leonardi, S. (2015). Large eddy simulations of the flow past wind tturbine: actuator line and disk modeling. *Wind Energy*, **18**, 1047–1060.

Mason, P.J. & Callen, N.S. (1986). flows magnitude of the subgrid-scale eddy coefficient in large-eddy simulations of turbulent channel flow. *Journal of Fluid Mechanics*, **162**, 439.

Meyers, J. & Meneveau, C. (2010). Large eddy simulations of large wind-turbine aarray in the atmospheric boundary layer. In *48th AIAA Aerospace Sciences Meeting Including the New Horizons Forum and Aerospace Exposition*, 827, American Institute of Aeronautics and Astronautics, American Institute of Aeronautics and Astronautics, Orlando, Florida.

Michelsen, J.A. (1992). Basis3d - a platform for development of multiblock pde ssolver. Tech. rep., AFM 92-06, Department of Fluid Mechanics, Technical University of Denmark.

Mikkelsen, R. (2003). *Actuator disc methods applied to wind turbines*. Ph.D. thesis, Technical University of Denmark, fM-PHD; No. 2003-02.

Moeng, C.H. (1984). A large-eddy simulation model for the study of planetary boundary-layer turbulence. *Journal of Atmospheric Sciences*, **41**, 2052–2062.

Morinishi, Y., Lund, T.S., Vasilyev, O.V. & Moin, P. (1998). Fully conservative higher order finite difference schemes for incompressible flow. *Journal of Computational Physics*, **143**, 90–124.

Moser, R.D., Kim, J. & Mansour, N.N. (1999). Direct numerical simulation of turbulent channel flow up to $Re_\tau = 590$. *Physics of Fluids*, **11**, 943–945.

Orszag, S.A. (1971). On the elimination of aliasing in finite-difference schemes by filtering high-wavenumber components. *Journal of the Atmospheric Sciences*, **28**, 1074–1074.

Peña, A., Réthoré, P.E. & van der Laan, M.P. (2015). On the application of the jensen wake model using a turbulence-dependent wake decay coefficient: the sexbierum case. *Wind Energy*, **19**, 763–776.

Piomelli, U., Ferziger, J. & Moin, P. (1989). New approximate boundary conditions for large eddy simulations of wall-bounded flows. *Physics of Fluids A*, **1**, 1061–1068.

Pope, S.B. (2000). *Turbulent Flows*, vol. 12. IOP Publishing.

Porté-Agel, F., Meneveau, C. & Parlange, M.B. (2000). A scale-dependent dynamic model for large-eddy simulation: application to a neutral atmospheric boundary layer. *Journal of Fluid Mechanics*, **415**, 261–284.

Ramos-García, N., Sørensen, J.N. & Shen, W.Z. (2013). A strong viscous-inviscid interaction model for rotating airfoils. *Wind Energy*, **17**, 1957–1984.

Réthoré, P.E., van der Laan, P., Troldborg, N., Zahle, F. & Sørensen, N.N. (2014). Verification and validation of an actuator disc model. *Wind Energy*, **17**, 919–937.

Schumann, U. (1975). Subgrid scale model for finite difference simulations of turbulent flows in plane channel and annuli. *Journal of Computational Physics*, **18**, 376–404.

Shen, W.Z., Zhang, H.H. & Sørensen, J.N. (2009). The actuator surface model: A new navier-stokes based model for rotor computations. *Journal of Solar Energy Engineering*, **131**, 011002.

Shives, M. & Crawford, C. (2013). Mesh and load distribution requirements for actuator line cfd simulations. *Wind Energy*, **16**, 1183–1196.

Simisiroglou, N., Karatsioris, M., Nilsson, K., Breton, S.P. & Ivanell, S. (2016). The actuator disc concept in phoenics. In *13th Deep Sea Offshore Wind R&D Conference, EERA DeepWind*, vol. 94, 269–277, Elsevier BV.

Slotnick, J., Khodadoust, A., Alonso, J., Darmofal, D., Gropp, W., Lurie, E. & Mavriplis, D. (2014). Cfd vision 2030 study: A path to revolutionary computational aerosciences. Tech. Rep. NASA/CR-2014-218178, NASA.

Smagorinsky, J. (1963). General circulation experimetns with the primitive equations. *Monthly Weather Review*, **91**, 99–164.

Sørensen, J.N. & Kock, C.W. (1995). A model for unsteady rotor aerodynamics. *Journal of Wind Engineering and Industrial Aerodynamics*, **58**, 259–275.

Sørensen, J.N. & Shen, W. (2002). Numerical modeling of wind turbine wakes. *Journal of Fluids Engineering*, **124**, 393.

Sørensen, J.N., Dag, K.O. & García, N.R. (2016). A refined tip correction based on decambering. *Wind Energy*, **19**, 787–802.

Sørensen, N.N. (1995). *General purpose flow solver applied to flow over hills*. Ph.D. thesis, Risø National Laboratory.

Spalart, P.R. (1988). Direct numerical study of leading edge contamination. In *Fluid Dynamics of Three-Dimensional Turbulent Shear Flows and Transition, AGARD-CP-438, Neuilly-sur-Seine, France*.

Stevens, R., Graham, J. & Meneveau, C. (2014). A concurrent precursor inflow method for large eddy simulations and applications to finite length wind farms. *Renewable Energy*, **68**, 46–50.

Sullivan, P.P. & Patton, E.G. (2008). A highly parallel algorithm for turbulence simulations in planetary boundary layers: results with memesh up to 1024^3. Paper No. 11B5, 18th American Meteorological Society Symposium on Boundary Layers and Turbulence, Stockholm, Sweden.

Townsend, A.A. (1976). *The Structure of Turbulent Shear Flow*, vol. 21. Cambridge University Press.

Troldborg, N. (2008). *Actuator Line Modeling of Wind Turbine Wakes*. Ph.D. thesis, DTU.

Troldborg, N., Zahle, F., Réthoré, P.E. & Sørensen, N.N. (2015). Comparison of wind turbine wake properties in non-sheared inflow predicted by different compuational fluid dynamics rotor models. *Wind Energy*, **18**, 1239–1250.

Technical University
of Denmark
DTU

Joint author statement

If a thesis contains articles (i.e. published journal and conference articles, unpublished manuscripts, chapters etc.) made in collaboration with other researchers, a joint-author statement verifying the PhD student's contribution to each article should be made by all authors. However, if an article has more than three authors the statement may be signed by a representative sample, cf. article 12, section 4 and 5 of the Ministerial Order No. 1039 27 August 2013 about the PhD degree. We refer to the Vancouver protocol's definition of authorship.

A representative sample of authors is comprised of

- Corresponding author and/or principal/first author (defined by the PhD student), and if there are more authors:
- 1-2 authors (where appropriate, these should be the international/non-supervisor authors)

Title of the article: A refined tip correction based on decambering

Author(s): Jens N. Sørensen, Kaya O. Dag, Néstor Ramos García

Journal/conference
* if applicable: Wind Energy

Name of PhD student: Kaya Onur Dag

Date of Birth: 22.03.199

Description of the PhD student's contribution to the abovementioned article

The technique was developed by the PhD student together with the first author. Also, the implementation of the technique and validations for both planar and wind turbine wings were done by the PhD student. Computations for the paper were conducted together with the third author and a small part of the text was produced by the PhD student.

Signature
of the PhD student

Date 29/05/2017

Signatures of co-authors

As a co-author I state that the description given above to the best of my knowledge corresponds to the process and I have no further comments.

Date (DD/MM/YY)	Name	Signature
29/05/2017	Néstor Ramos García	
29/05/2017	Jens N. Sørensen	Jens N. Sørensen

Joint author statements shall be delivered to the *PhD administration* along with the PhD thesis

Wind Energy

WIND ENERGY
Wind Energ. 2016; **19**:787–802
DOI: 10.1002/we.1865

RESEARCH ARTICLE

A refined tip correction based on decambering

Jens N. Sørensen, Kaya O. Dag and Néstor Ramos-García

DTU Wind Energy, Technical University of Denmark, 2800 Kongens Lyngby, Denmark

ABSTRACT

A new tip correction for use in performance codes based on the blade element momentum (BEM) or the lifting-line technique is presented. The correction modifies the circulation by taking into account the additional influence of the induction of the vortices in the wake, using the so-called decambering effect and thin-airfoil theory. A limitation of the standard Prandtl tip correction is that it represents the surface loading by a line distribution that does not take into account the actual shape of the rotor blade. Thus, the chord distribution does not appear as a parameter in the model, and the loading in the proximity of the tip is generally found to be overestimated. The new tip correction is implemented as an additional correction in order to represent the surface loading by a line distribution. Comparing computations using the new model with standard BEM results and computations using a 3D panel code show that the inclusion of the correction greatly improves the results. The new model also explains some of the discrepancies that earlier on have been observed when using a BEM technique based alone upon standard tip corrections. Copyright © 2015 John Wiley & Sons, Ltd.

KEYWORDS
decambering; tip correction; wind-turbine aerodynamics; wind-turbine performance

Correspondence
J. N. Sørensen, DTU Wind Energy, Technical University of Denmark, Nils Koppels Alle, Bldg. 403, 2800 Kongens Lyngby, Denmark.
E-mail: jnso@dtu.dk

Received 18 December 2013; Revised 27 March 2015; Accepted 16 April 2015

1. INTRODUCTION

The tip correction was originally introduced by Prandtl in an appendix to the dissertation of Betz[1] as a means to correct the loading obtained from axisymmetric momentum theory to account for the difference between a rotor with infinitely many blades and a realistic rotor with a finite number of blades. The correction illustrated the ingenious way Prandtl introduced simple engineering solutions to complicated problems. Betz formulated the concept of the optimum rotor with a finite number of blades, by stating that maximum efficiency is obtained when the pitch of the trailing vortices in the wake of the rotor is constant, and each trailing vortex sheet translates backward as an un-deformed regular helicoidal surface with a constant speed. This was essentially inspired from the lifting-line theory for a planar wing, which states that maximum efficiency is obtained when a constant downwash is produced. However, at that time, it was not possible to actually solve the problem, although Goldstein[2] some years later showed that a solution indeed could be obtained using infinite series of Bessel functions. The way Prandtl solved the problem was to approximate the helical wake with a series of planar vortex surfaces and determine the tip correction as the ratio between the circulation of an N-bladed rotor and the circulation of a rotor with infinitely many blades. For the latter, the circulation was determined as the jump in velocity potential over the vortex sheet.[3] The outcome of this analysis was a simple expression giving the load reduction as a function of tip speed ratio, flow angle, and distance from the tip of the rotor. This correction was later slightly modified by Glauert,[4] who combined it with the blade element momentum (BEM) theory, as a simple remedy to take into account the difference between the blade element approach and the axisymmetric momentum theory. Although the theory today is routinely used as a tool for designing and analyzing wind-turbine rotors, it is also criticized for not representing accurately the loading in near vicinity of the tip of the rotor. This has led to different versions of the original formulation (e.g., De Vries[5]), and in a recent work of Shen *et al.*,[6] it was shown that the original formulation contains an inconsistency that, to a certain extent, can be remedied by introducing a further correction. Another problem with the tip correction is that it does not take into account the actual shape of the rotor blade. Thus, the chord distribution does not appear as a parameter in the model, and it seems that something more than just accounting for the number of finite blades is missing in the expression. This is further demonstrated with the development of the actuator line technique. The actuator line technique was developed by Sørensen and Shen[7] as a means of introducing a lifting-line model into the Navier–Stokes equations. In the model, the loading, which is obtained from tabulated airfoil data, is distributed along lines representing the rotor blades. Using this approach, it should in principle not be necessary to introduce any tip correction, because the loading is obtained directly on each individual blade. Nevertheless, the loading in the proximity of the tip seems always to be overestimated, suggesting that some additional correction is required in order to represent the surface loading by a line distribution.

In a short report, published in conjunction with a plenary meeting within a European project, Montgomerie[8] demonstrated that an error is introduced when using the lifting-line or the BEM method in their usual form. This error is caused by the fact that these methods rely on the blade representation being a line instead of a surface. Indeed, the downwash induced by the vortex system in the wake causes a curved streamline along the chord line that virtually corresponds to an additional negative camber of the airfoil. Because the induction generally will be higher at the trailing edge, which is the line from which the trailing vortices are shed into the wake, than at the leading edge, the aerodynamic consequence is that the effect of the induction from the free vortices is felt as a decambering of the airfoil. Hence, it tends to increase the zero lift angle and, by this, decrease the loading. The effect is, just as for the usual tip correction, felt everywhere on the blade but most significantly close to the tip. To illustrate the decambering effect, Figure 1 shows how the local induction affects the aerodynamic characteristics of the local airfoil section. It is here seen how the downwash from the free vortices induce a local velocity field that changes along the chord line.

In a lifting-line technique, only the velocity component at the c/4 position is used to compute the relative velocity and angle of attack. However, as can be seen from the figure, there is an additional velocity component, $\Delta w_i = w_i - w_{c.p.}$, that is positive from the leading edge to the center of pressure, $x_{c.p.}$, and negative from the center of pressure to the trailing edge. Thus, as seen from the airfoil, the additional velocity is felt as curved streamlines, which consequently represents a negative bending of the airfoil. This is shown in Figures 2(a),(b), which illustrates how the induced velocity of the free vortex wake is felt as a negative bending of the chord line. This effect was discussed by Montgomerie[8] and referred to as decambering. It should be noted that decambering also has been employed to correct airfoil data for curvature effects in aerodynamic models of vertical axis turbines.[9,10] Furthermore, the term is also employed for post-stall predictions using lifting-line or vortex lattice models.[11]

In this paper, a technique based on the Biot–Savart induction law is introduced, which can be used to determine the effect of decambering. Furthermore, using thin airfoil theory, a simple correction technique is developed by which the loading from lifting-line or BEM models can take into account the decambering effect and employ it together with the usual tip correction. By comparing the results from the model with a more advanced numerical technique representing the surface of the rotor, it will be shown that the introduction of a decambering correction indeed explains most of the discrepancies attained when using the lifting-line technique or a BEM model with only a Prandtl tip correction.

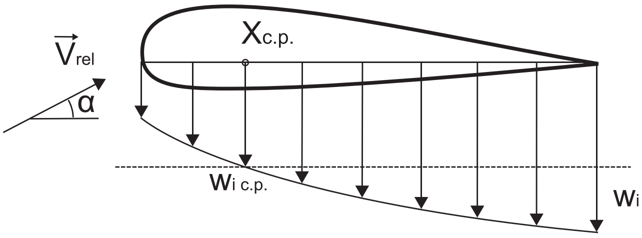

Figure 1. Downwash due to the induction of the free vortices in the wake.

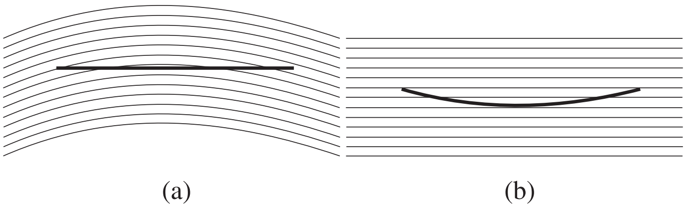

Figure 2. (a) Curved streamlines representing the additional downwash from the induction of the free vortices in the wake. (b) The effect from the additional downwash seen as an effective negative bending (decambering) of the airfoil.

The paper is organized as follows. In Section 2, the equations and the technique behind the decambering tip correction are introduced. In Section 3, the lifting line, the BEM method and their coupling with the new tip correction are described. Furthermore, the vortex lattice (panel) method used to validate the correction is described. In Section 4, the new technique is validated against the vortex lattice method. Finally, the work is concluded in Section 5.

2. THE DECAMBERING CORRECTION

Figures 3(a),(b) show a translating and a rotating wing, and the associated distribution of circulation of a simplified vortex system consisting of trailing vortex lines. Along the center of pressure, which here is taken as the c/4-chord line of the wing, is shown the bound vorticity. The lines extending downwards from the bound vortex line constitutes the trailing vortices. The strength of the trailing vortices is determined from the distribution of the circulation of the bound vortex. Representing the bound circulation distribution by discrete values Γ_i, with $i = 1, 2, \ldots, N$, where $i = 1$ represents the root and $i = N$ the tip, the associated system of trailing vortices are given as horseshoe vortices with strength $\hat{\Gamma}_i = \Gamma_{i+1} - \Gamma_i$. In the case of a planar wing, the trailing vortices are straight lines, whereas they form a helical spiral with a helical pitch corresponding to the local flow angle in the case of a rotor blade. It is the effect from the trailing vortices that induces a downwash along the chord line that, for each cross section, causes the decambering effect. The resulting correction is carried out in a series of control points, which in the spanwise direction, are located at the midpoint of each bound vortex filament.

The induction is determined from the Biot–Savart induction law according to the following compact formula:[12]

$$\vec{q} = \frac{\Gamma}{4\pi} \frac{(r_1 + r_2)(\vec{r}_1 \times \vec{r}_2)}{r_1 r_2 (r_1 r_2 + \vec{r}_1 \cdot \vec{r}_2)} \tag{1}$$

where $\vec{r}_1$ and $\vec{r}_2$ denote the position vectors between the control point and the two edges of the discretized vortex filament. In order to determine the effect of the downwash on the airfoil characteristics, thin-airfoil theory is employed. This is accomplished by dividing each airfoil section into a set of evaluation points following a cosine distribution. This distribution is sketched in Figure 4(a), from which it can be seen that the evaluation point, x_k, is given as

$$x_k = \frac{c}{2}(1 - cos\theta_k) \tag{2}$$

where

$$\theta_k = \pi \frac{k-1}{M-1}, \quad k \in [1, M] \tag{3}$$

Here, M denotes the number of evaluation points. The evaluation points are located along the chord line with the leading edge at $x = 0$ ($\theta = 0$) and the trailing edge at $x = c$ ($\theta = \pi$). The camber line of an airfoil is usually a known function, $\eta_c = \eta_c(x)$ (Figure 4(b)). However, in the present case, the camber line is formed from the additional induction of the free vortices along the chord line. From thin-airfoil theory, it is known that the slope of the local (total) velocity is equal to the camber line slope. Hence,

$$\frac{d\eta_c}{dx} = \frac{w}{u} \tag{4}$$

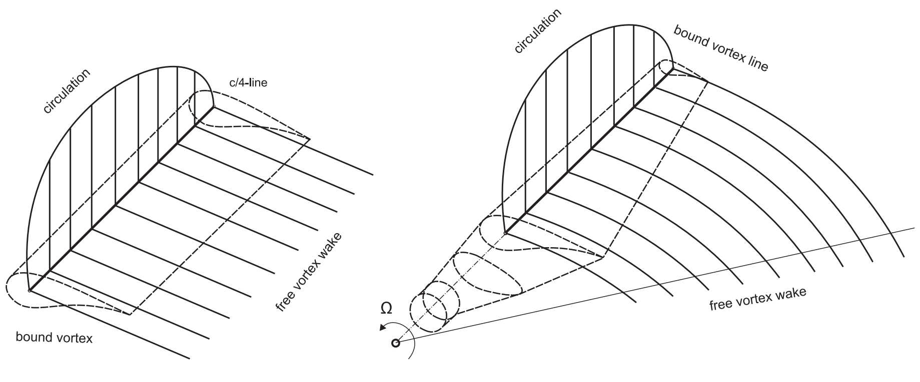

(a) (b)

Figure 3. (a) Translating wing and associated vortex lines. (b) Rotating wing and associated vortex lines.

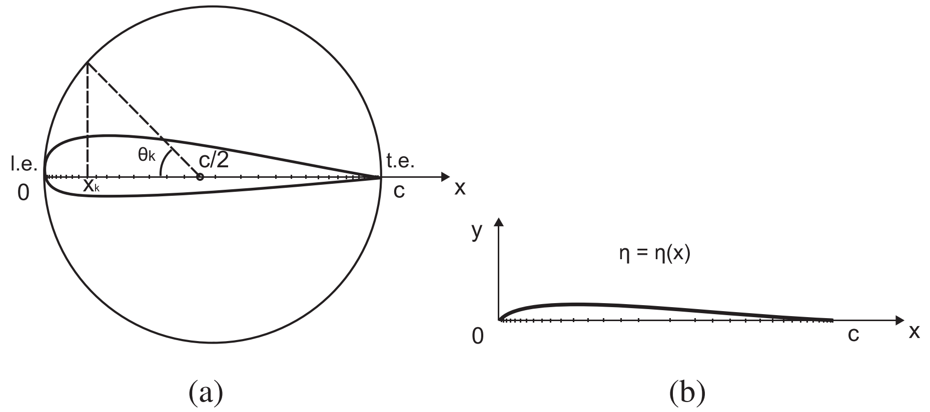

Figure 4. (a) Distribution of evaluation point, x_i, along the chord line. (b) Representation of the camber line $\eta = \eta(x)$.

where (u, w) denotes the velocity components tangential and normal to the chord lines, respectively. For each evaluation point on the chord line, the induced velocity is determined as the sum of contributions from the vortex segments of each of the N trailing vortices. Thus, for a wing section subject to a local relative velocity, $\vec{V}_{rel}$, and angle of attack, α_j, the induced velocity can be written as

$$w_{jk} = \sum_{i=1}^{N} a_{ijk}\Gamma_i, \quad u_{jk} = \sum_{i=1}^{N} b_{ijk}\Gamma_i \tag{5}$$

where a_{ijk} refers to the induced normal velocity on evaluation point k on chord line j due to the induction from vortex i with unit strength, and w_{jk} is the corresponding induced velocity, resulting from the induction of all free vortices, each of strength Γ_i. Likewise, b_{ijk} refers to the induced velocity in the tangent direction to the chord line. For simplicity, assuming that the center of pressure is located at the c/4 point, the additional camber line slope is determined by subtracting the local induction by the induction at the c/4-point. Thus, at each control point the additional slope due to the decambering effect reads

$$\frac{d\eta_c}{dx}\Big|_{jk} = -\frac{w_{jk} - w_{j,c/4}}{||V_{rel,j}|| \cos\alpha_j + u_{jk} - u_{j,c/4}} \tag{6}$$

where $w_{j,c/4} = \sum_{i=1}^{N} a_{ij,c/4}\Gamma_i$, and $u_{j,c/4} = \sum_{i=1}^{N} b_{ij,c/4}\Gamma_i$, with $a_{ij,c/4}$ referring to the induced normal velocity on the c/4-chord line j due to the interaction from unit vortex i and $b_{ij,c/4}$ the same for the tangential velocity. Note that the minus sign in equation (6) is introduced because the decambering denotes the effect of the additional streamline curvature seen from the airfoil.

For an airfoil with camber and zero-lift angle α_{L0}, the lift coefficient is given as

$$C_l = 2\pi(\alpha - \alpha_{L0}) \tag{7}$$

Thus, the difference in lift coefficient between an airfoil with and without camber is given as

$$\Delta C_l = -2\pi\alpha_{L0} \tag{8}$$

According to,[12] the zero-lift angle can be determined from the following expression:

$$\alpha_{L0} = -\frac{1}{\pi}\int_0^{\pi} \frac{d\eta_c}{dx}(\cos\theta - 1)d\theta \tag{9}$$

Combining equations (6) and (9) yields

$$\alpha_{L0} = \frac{1}{\pi}\int_0^{\pi} \left(\frac{w_{jk} - w_{j,c/4}}{||V_{rel,j}|| \cos\alpha_j + u_{jk} - u_{j,c/4}}\right)(\cos\theta - 1)d\theta \tag{10}$$

Replacing the integration with a discrete summation, the following formula is obtained for correcting the lift coefficient at cross section j:

$$\Delta C_{l,j} = -2\Delta\theta \sum_{k=1}^{M} \frac{(w_{jk} - w_{j,c/4})(\cos\theta_k - 1)}{||V_{rel,j}||\cos\alpha_j + (u_{jk} - u_{j,c/4})} \tag{11}$$

where $\Delta\theta = \pi/(M-1)$. In order to correct directly on the circulation distribution, the Kutta–Joukowsky theorem is employed,

$$\Gamma = \frac{1}{2} c V_{rel} C_l \tag{12}$$

Combining equations (11) and (12), assuming that $(u_{jk} - u_{j,c/4}) << V_{rel,j}$, results in the following correction formula

$$\Delta\Gamma_j = \frac{\Delta\theta \cdot c_j}{\cos\alpha_j} \sum_{k=1}^{M} (w_{jk} - w_{j,c/4})(\cos\theta_k - 1) \tag{13}$$

Equations (5) and (13) form the final set of equations for correcting the circulation because of the decambering effect of the free wake vortices. It is easily seen that the system constitutes an implicit set of equations, because the induced velocity depends on the circulation that is being corrected. The system may either be solved iteratively or as a full matrix system. In the latter case, combining equations (5), (8), (12) and (13), the full system may be written as

$$\Gamma_j + \frac{\Delta\theta c_j}{\cos\alpha_j} \sum_{k=1}^{M} \sum_{i=1}^{N} (a_{ijk} - a_{ij,c/4})(\cos\theta_k - 1)\Gamma_i = \frac{1}{2} c_j V_{rel,j} \bar{C}_{l,j} \tag{14}$$

where $\bar{C}_{l,j}$ is the lift coefficient obtained directly from the relative velocity, i.e., without the decambering correction. Equation (14) can be written in a more compact form as

$$\sum_{i=1}^{N} d_{ij}\Gamma_i = e_j, \quad j = 1, 2, \ldots, N \tag{15}$$

where

$$d_{ij} = \delta_{ij} + \frac{\Delta\theta c_j}{\cos\alpha_j} \sum_{k=1}^{M} (a_{ijk} - a_{ij,c/4})(\cos\theta_k - 1), \quad \text{and} \quad e_j = \frac{1}{2} c_j V_{rel,j} \bar{C}_{l,j} \tag{16}$$

with δ_{ij} denoting the Kronecker delta. In the expression, the coefficient a_{ijk} depends on the geometry of the wing and on the local flow angles at which the free vortices are shed into the wake. Thus, for a given wing geometry, d_{ij} may once and for all be computed for various flow angles and subsequently be determined by interpolation in the performance computations. To be in accordance with thin-airfoil theory, the center of pressure was assumed to be located in the c/4-point. However, for a typical wind-turbine airfoil, this is normally located close to the c/3-point. Nevertheless, this depends on the spanwise location and operating conditions. To evaluate the error committed by having an offset between the actual center of pressure and the one employed in the analysis, a simple estimate can be made by assuming a linear distribution of additional induction. The equation forming the background from this analysis is derived in **Appendix A**. From this, we get that utilizing the c/4-point instead of the c/3-point results in a change in the correction of the angle of attack of 16%. As an example, a correction $\Delta\alpha = 6°$ would be reduced to $\Delta\alpha = 5°$. In the next section, the application of the correction together with the lifting-line technique and the BEM method will be presented.

3. AERODYNAMIC MODELING

In this section, different aerodynamic models are introduced. In particular, the lifting-line method and the BEM techniques, which both will be used together with the new decambering technique, are presented. To validate the technique, a 3D panel method is employed, which will also be explained.

3.1. Lifting-line method

In the lifting-line method, the vorticity on the wing and in the wake are represented by horseshoe vortices in a way that is similar to the sketches shown in Figures 3(a),(b). The induction from the trailing vortices is computed from equation (1), and the local relative velocity is subsequently calculated at the c/4-point and employed to compute the local angle of attack. The resulting lift-coefficient distribution is then determined from tabulated airfoil data. In order to determine the strength of the trailing vortices, the Kutta–Joukowsky theorem, equation (12), is employed, which subsequently is corrected for the influence of decamber by solving equations (14)–(16). It is clearly seen that this technique is very well suited to include the influence of decamber as we are employing the same vortex system for computing the angle of attack as for computing the downwash forming the input to the decambering correction. In the present implementation, the overall numerical technique for determining the circulation distribution is iterative, and the vortices in the wake are prescribed to be located in the plane of the wing.

3.2. The Blade-Element Momentum (BEM) method

The BEM method was developed by Glauert[4] as a practical way to analyse and design rotor blades. In the BEM method the interference factors, a and a', are introduced as

$$a = 1 - u_R/U_0 \quad \text{and} \quad a' = \frac{u_\theta}{2\Omega r} \tag{17}$$

where u_R is the axial velocity in the rotor plane, U_0 is the wind speed, u_θ is the rotational velocity in the wake just after the rotor, and Ωr is the local tangential velocity of the rotor at position r. The loading is computed by combining a local blade element using tabulated two-dimensional airfoil data and the one-dimensional momentum theory. Carrying out the analysis (e.g. Hansen[13]), the following relations are obtained:

$$a = \frac{1}{4F sin^2\phi/(\sigma C_l cos\phi) + 1} \tag{18}$$

and

$$a' = \frac{1}{4F\cos\phi/(\sigma C_l) - 1} \tag{19}$$

where $\sigma = N_b c/2\pi r$ is the solidity, with N_b denoting the number of blades. ϕ is the local flow angle, $\tan\phi = \frac{U_0(1-a)}{\Omega r(1+a')}$, and F is the Prandtl 'tip correction' factor to account for a finite number of blades,

$$F = \frac{2}{\pi}\cos^{-1}\left[exp\left(-\frac{N_b(R-r)}{2r sin\phi}\right)\right] \tag{20}$$

where R is the radius of the rotor. Equations (18)–(20) are solved iteratively at each cross section, using tabulated airfoil data to determine the local flow properties. After each iteration, the decambering correction is introduced by correcting the circulation by solving equations (14)–(16). The induction coefficients in equation (5) are determined by computing the induction from the trailing vortices in the wake. These are represented by a number of helical segments, which are released from the trailing edge with the local flow angle, ϕ, and followed a certain distance downstream in the wake. Note that the decambering correction, equation (15), forms an $N \times N$ system whereas the BEM method is a $2 \times N$ system, meaning that the inclusion of the decambering correction is more computational costly that the BEM in itself. There is certainly room for making the technique more computationally efficient. This, however, is not the scope of the present work, where the main aim is to illustrate that the correction is required in order to obtain reliable results when using the BEM method.

3.3. The vortex lattice (panel) method

This method is introduced in order to validate the developed correction. In the panel method, the surface of the lifting body is simulated by a distribution of quadrilateral singularities satisfying the no-penetration velocity condition. In the present work, both the inviscid and the viscous version of the in-house developed Method for Interactive Rotor Aerodynamic Simulations (MIRAS)[14] are employed. In the inviscid part of the model, the problem is considered in two regions: the surface, which is represented by quadrilateral sources and dipoles, and the wake, which is modeled by vortex filaments. The vortex wake is released at the trailing edges using the unsteady Kutta–Joukowsky condition of zero trailing edge loading. To satisfy this condition, at each time step, a quadrilateral panel with a doublet distribution is created as the first wake panel for each one of the span-wise stations. The strength of these panels is equal to the difference between the corresponding upper and lower trailing edge quadrilateral doublets. The filaments are subsequently convected downstream according to the induction law of Biot–Savart, introducing a viscous core model to approximate viscous diffusion and thus including vortex core growth and vortex straining. More details about the model, including a thorough validation, can be found in.[15]

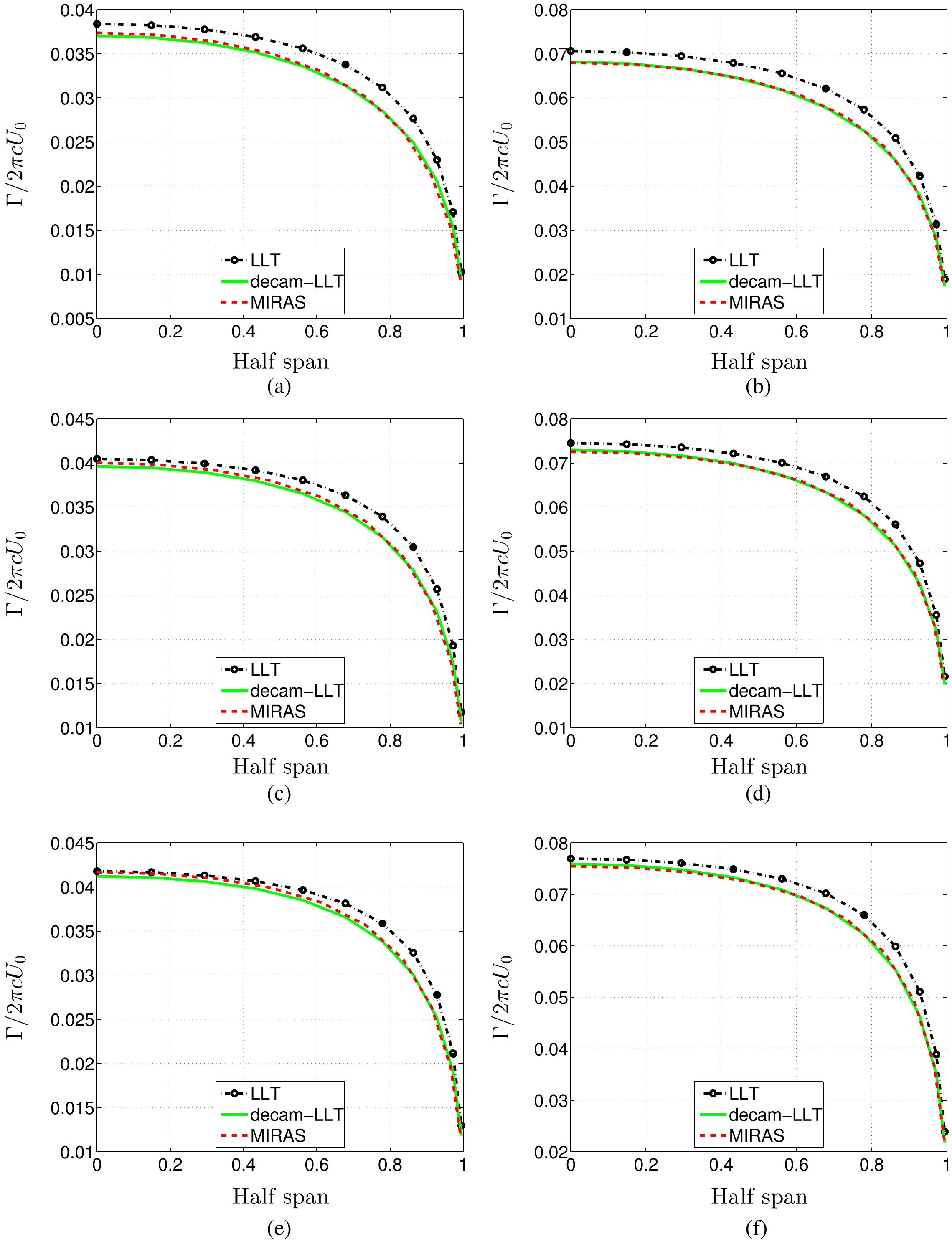

Figure 5. Distributions of normalized circulation, $\Gamma/2\pi cU_0$, for the planar wing configurations at a geometrical angle of attack of 5°. (a) NACA0012 AR=6, (b) NACA4412 AR=6, (c) NACA0012 AR=8, (d) NACA4412 AR=8, (e) NACA0012 AR=10, (f) NACA4412 AR=10.

4. RESULTS AND DISCUSSION

In this section, the new tip correction is validated against results obtained from the MIRAS code. The computations are carried out both for planar translating wings and wind-turbine rotor configurations.

4.1. Planar translating wing

In what follows, the results from the lifting-line method described in section 3.1 are compared with the MIRAS panel code. For comparison, the computations are carried out both with and without the new tip correction. The examples considered are planar wings with constant chord consisting of NACA 0012 or 4412 airfoil sections, and at different aspect ratios. From 2D viscous–inviscid computations, employing a 2D version of the MIRAS code, the lift coefficient for 2D airfoil sections has been calculated and approximated as $C_l \simeq 0.12 \cdot \alpha^\circ$ for the NACA 0012 airfoil and as $C_l \simeq 0.12 \cdot \alpha^\circ + 0.5$ for the NACA 4412 airfoil. These expressions are those used in equation (12) to obtain the circulation distribution. In Figures 5(a)–(f), computed circulation distributions for six different wing configurations are compared. The lifting-line computations are labeled $'LLT'$ and the corresponding results applying the decambering correction are labeled $'decam - LLT'$. In the figures, the circulation is made dimensionless by $2\pi c U_0$, where c is the chord length and U_0 is the free-stream velocity. As the circulation distribution is symmetric, only one half of the distribution is presented for each case. It is clearly

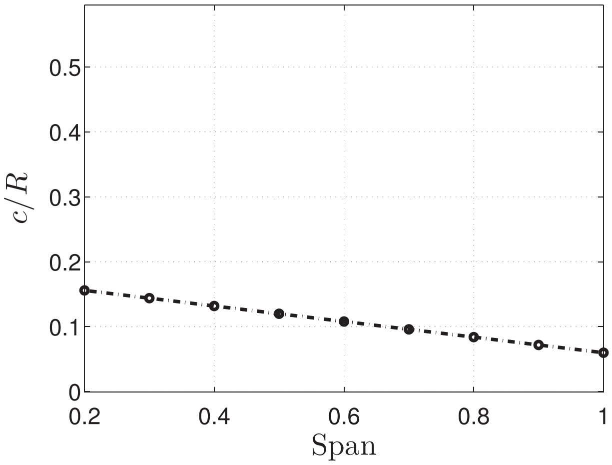

Figure 6. Chord distribution of the three bladed optimum rotor.

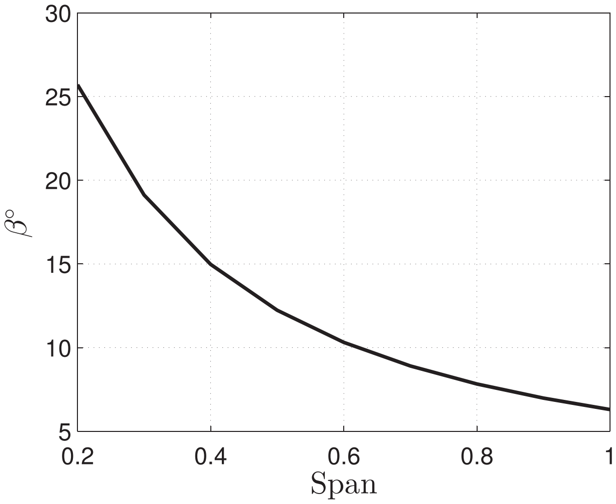

Figure 7. Twist distribution of the optimum rotors.

seen that the inclusion of the decambering effect improves the results. Generally, the lifting-line technique is over-predicting the circulation with 10–15%, whereas the inclusion of the decambering correction ensures a circulation distribution that within plotting accuracy corresponds to what is obtained when using a full panel discretization of the surface. From the figure, it is seen that the decambering correction works for both symmetric and unsymmetrical airfoils and for all aspect ratios considered.

4.2. Rotating wing

To validate the effect of using the decambering correction on a rotating wing, the correction is employed together with the BEM method. In this method, it is still necessary to use the Prandtl tip correction to correct for finite number of blades in the momentum theory. Hence, it is required to apply both the Prandtl tip correction and the decambering correction.

4.2.1. Simple optimally designed rotors.

In this part of the study, the influence of different number of blades is analysed. For this purpose, three wind-turbine rotors equipped with one, two or three blades are designed using the technique for designing aerodynamically optimum planforms outlined in the study of Burton *et al.*[16] In this technique, it is assumed that the optimum interference factors take the values

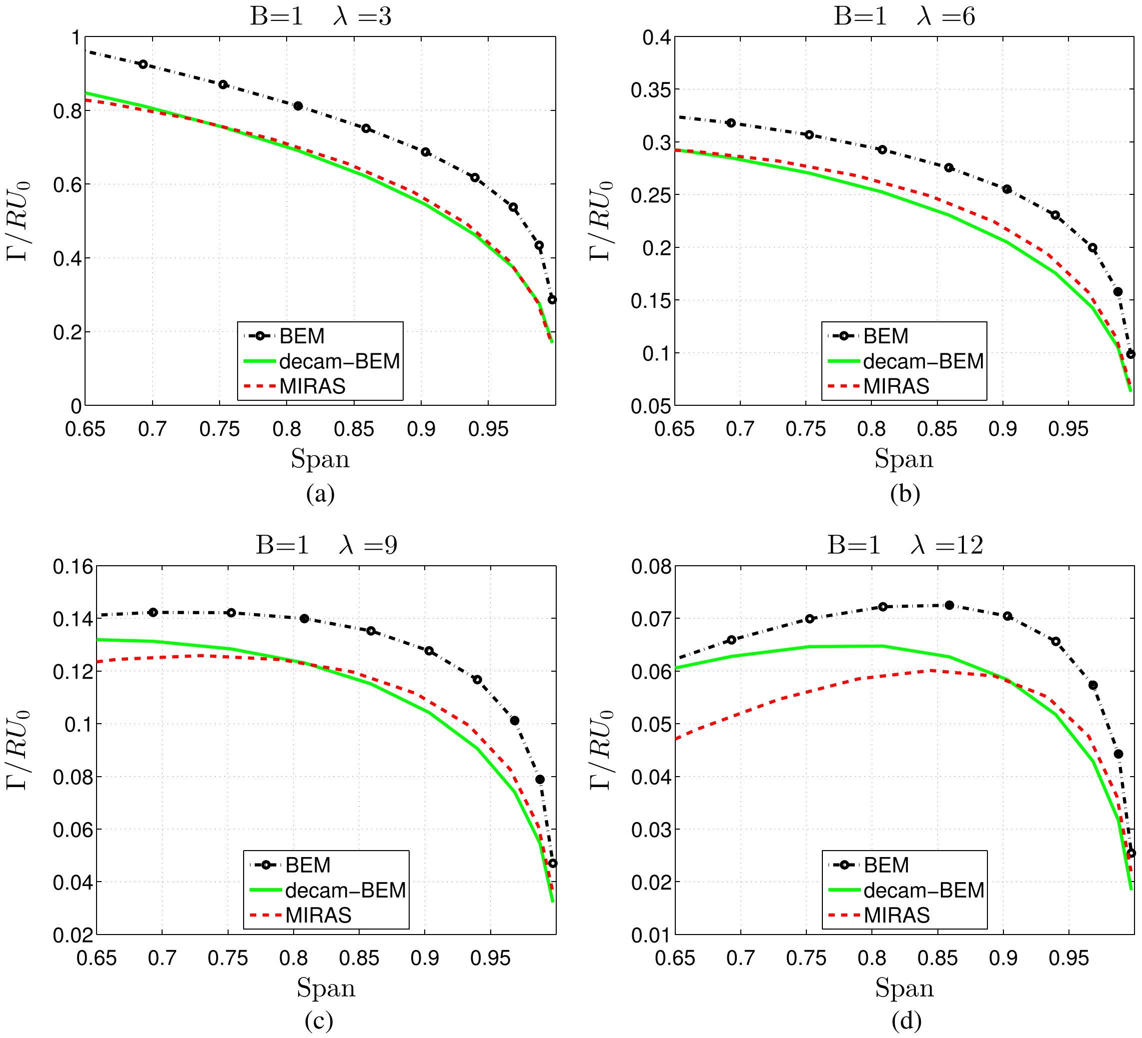

Figure 8. Distributions of normalized circulation, Γ/RU_O, for the single blade optimum rotor . (a) $\lambda = 3$, (b) $\lambda = 6$, (c) $\lambda = 9$, (d) $\lambda = 12$.

$$a_{opt} = 1/3 \quad \text{and} \quad a'_{opt} = \frac{2}{9\lambda^2 y^2} \tag{21}$$

where $y = r/R$, and λ is the tip speed ratio. The general expression to determine the planform is as follows:

$$N_b C_l \left(\frac{c}{R}\right) = \frac{8\pi \cos\phi a'}{1 + a'} y \tag{22}$$

with the corresponding twist angle distribution:

$$\beta = \tan^{-1}\left(\frac{1-a}{\lambda y(1+a')}\right) \tag{23}$$

It should be noted that the Prandtl tip correction has not been included in the equations for the design of the rotor.

To simplify the geometry, the NACA 4412 airfoil is used along the entire span, and the rotor is optimized to operate at a tip speed ratio, $\lambda = 6$, and an optimum angle of attack of 1.7°, corresponding to $C_l = 0.7$. To simplify further, the expression for the chord distribution, equation (22), is replaced by a linear expression with the same slope as at the $y = 80\%$ point. For a three-bladed rotor, this results in a blade with a chord length ranging linearly from $0.156R$ at the

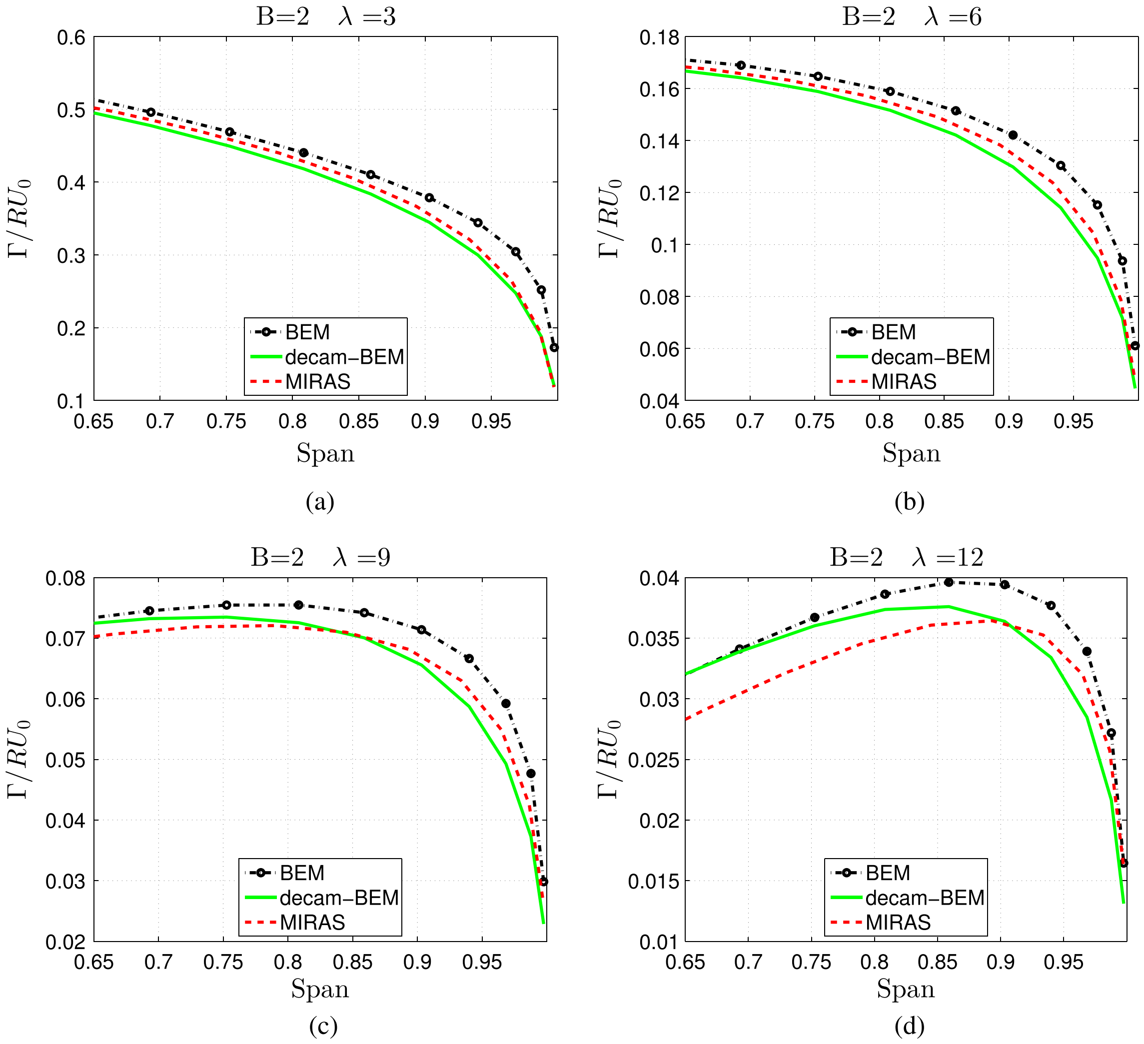

Figure 9. Distributions of normalized circulation, Γ/RU_0, for the two bladed optimum rotor. (a) $\lambda = 3$, (b) $\lambda = 6$, (c) $\lambda = 9$, (d) $\lambda = 12$.

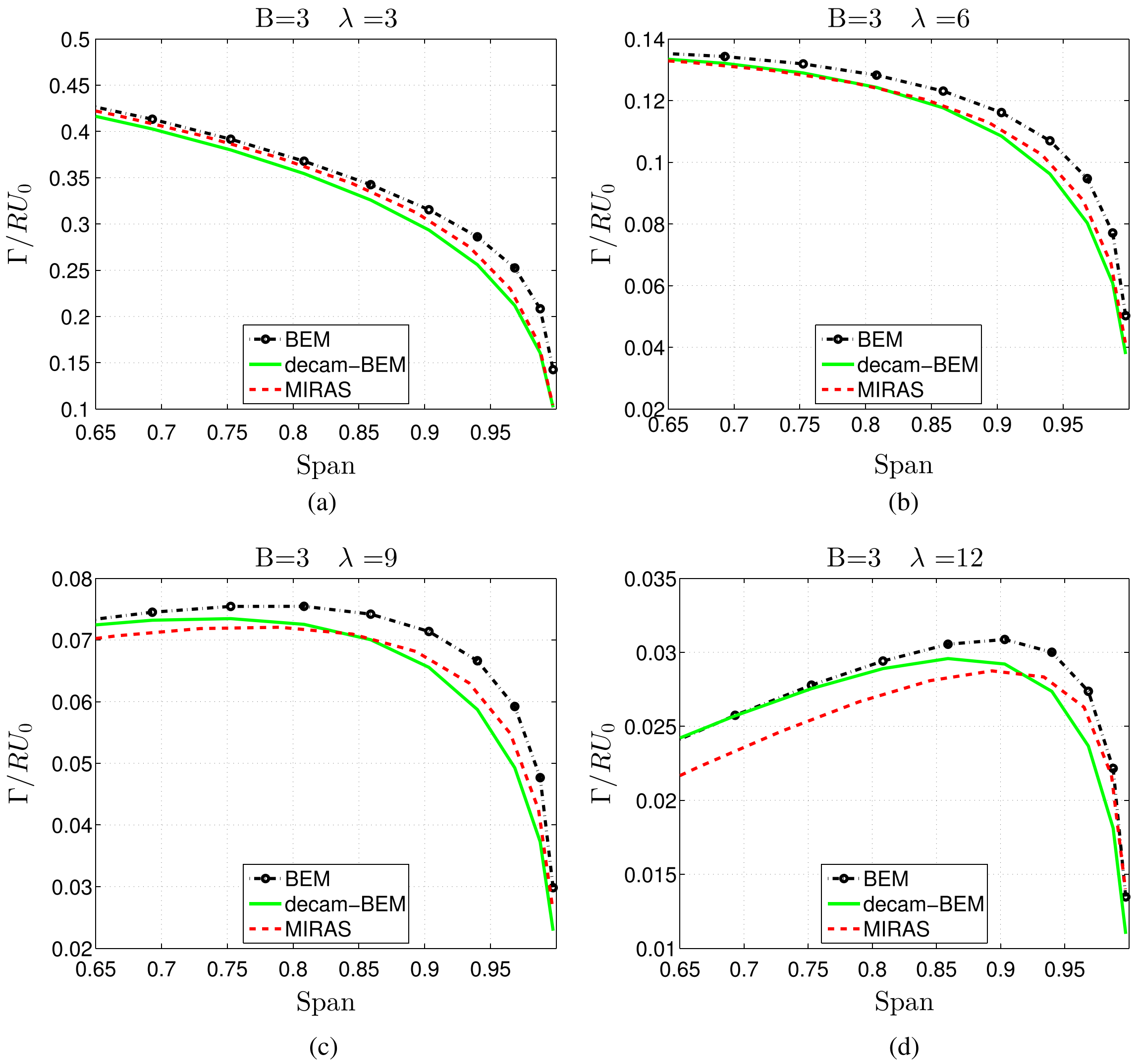

(a) (b) (c) (d)

Figure 10. Distributions of normalized circulation, Γ/RU_0, for the three bladed optimum rotor . (a) $\lambda = 3$, (b) $\lambda = 6$, (c) $\lambda = 9$, (d) $\lambda = 12$.

root to $0.06R$ at the tip. From equation (22), it is readily seen that rotors with other blade numbers are designed simply by scaling the chord distribution by the number of blades, and equation (23) shows that the twist distribution is invariant to the number of blades. The chord distribution for a three-bladed rotor designed from this technique is shown in Figure 6, and the associated twist distribution is plotted in Figure 7.

In Figures 8(a)–(d), 9(a)–(d) and 10(a)–(d), the computed circulation distributions are shown for one-bladed, two-bladed and three-bladed rotors, respectively. In the figures, the circulation is made dimensionless by RU_0, where R is the rotor radius and U_0 is the free-stream velocity. The plots compare BEM results, both with and without the decambering correction, with results from the MIRAS panel code at different tip speed ratios. In all the depicted cases, it is clear that the decambering correction has a positive effect on the resulting circulation distribution. In most cases, the improvement in the circulation is in of the order of 10–15%, being most significant, however, for the one-bladed rotor. As can also be seen from the figures, the computations without the decambering correction always over-predict the circulation. Hence, the word decambering should be taken literally in the sense that the effective lift distribution, and by this the circulation, is always being reduced when using the correction.

Wake dependency

To use the method in combination with the BEM technique, a helical wake sheet is generated by using the local axial induction values from BEM calculation to define the helical pitch. The length of each vortex line is taken to be three rotations

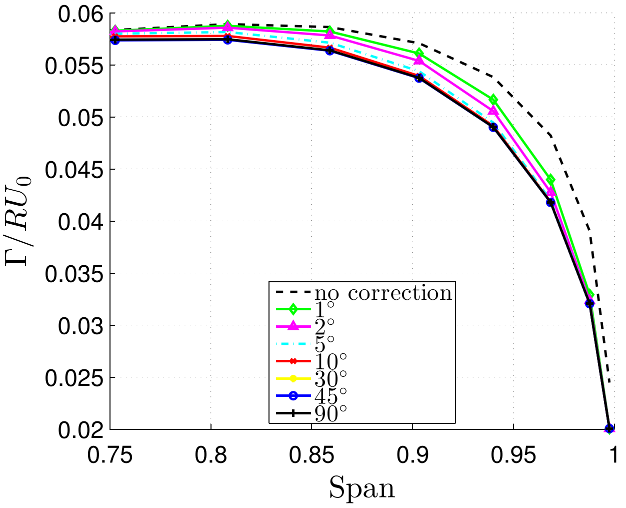

Figure 11. Wake length dependency of the decambering correction.

for the correction. However to analyze the dependency of the wake length, simulations are conducted with different wake lengths. For this purpose, the three-bladed optimally designed rotor with $\lambda = 9$ is used. As can be seen from Figure 11 that a wake length corresponding to 30° of the rotation is enough for correcting the additional curvature effects from the wake. To be on the safe side, a wake length corresponding to a 90° rotation has been used.

4.2.2. The NREL 5-MW reference rotor.

In order to validate further the decambering correction, simulations have been carried out for the NREL 5 MW virtual reference rotor. The NREL 5-MW reference wind turbine was designed at National Renewable Energy Laboratory (NREL) by Jonkman *et al.* in order to have a common test case for comparing different aero-elastic tools. The turbine does not represent an actual wind turbine but is designed as a good approximation of what an actual wind turbine of the associated size would be like. The diameter of the rotor is 128 m, and the blade geometry is based on cylindrical cross sections on the inner part, DU21 - DU40 airfoils at the mid-part and on NACA 64 series airfoils on the outer part. A full description, including airfoil data, can be found in.[17]

In the following, a comparison between viscous MIRAS simulations and BEM with and without the decambering correction will be presented for the reference rotor. The viscous MIRAS simulations were performed on a surface mesh consisting of 20 spanwise cells and 160 chordwise cells, and 16 wake revolutions were simulated with an angular discretization of 10°. Viscous effects were taken into account in the potential panel code by employing the transpiration velocity concept and solving the integral boundary-layer equations with free laminar to turbulent transition and a turbulent intensity of 0.1%. For further information on the 3D viscous–inviscid coupling technique, the reader is referred to Ramos-García *et al.*[15] The airfoil polars used in the BEM calculations were obtained from Quasi 3d Unsteady viscous-inviscid Interactive Code (Q^{3}UIC) 2D computations for the local airfoil geometry at the different spanwise locations. More details on the viscous–inviscid interaction technique can be found in Ramos-García *et al.*[14]

In Figures 12(a)–(f), comparisons between the calculated normal and tangential forces for the wind speeds of 6, 8 and 10 ms^{-1} are displayed. For the tangential loading in the inner part of the blade, the BEM computations are in good agreement with the viscous MIRAS computations. However, in the outer part, the BEM computations overestimate the forces. In terms of the normal forces, BEM computations are consistently overpredicting the loading along the whole blade span.

Because the decambering correction is applied to the circulation and therefore only influencing the lift force, it has a minor effect on the tangential load at small angles of attack, showing that the power performance of the rotor is practically unchanged by the correction. Comparing the results for the normal load shows that the decambering correction alleviates the loading by 7–8% on the outer 10% of the blade. The normal load from the BEM computations, however, seems in all cases to be too high at the outer 30% of the blade, as compared with the MIRAS code.

4.2.3. The experimental MEXICO rotor.

The Measurements and Experiments In Controlled conditions (MEXICO) experiment is used as a final validation of the presented decambering correction. The MEXICO experimental campaign was carried out on a three-bladed wind-turbine model of diameter 4.5 m. Measurements were performed under controlled conditions in the large-scale low-speed facility

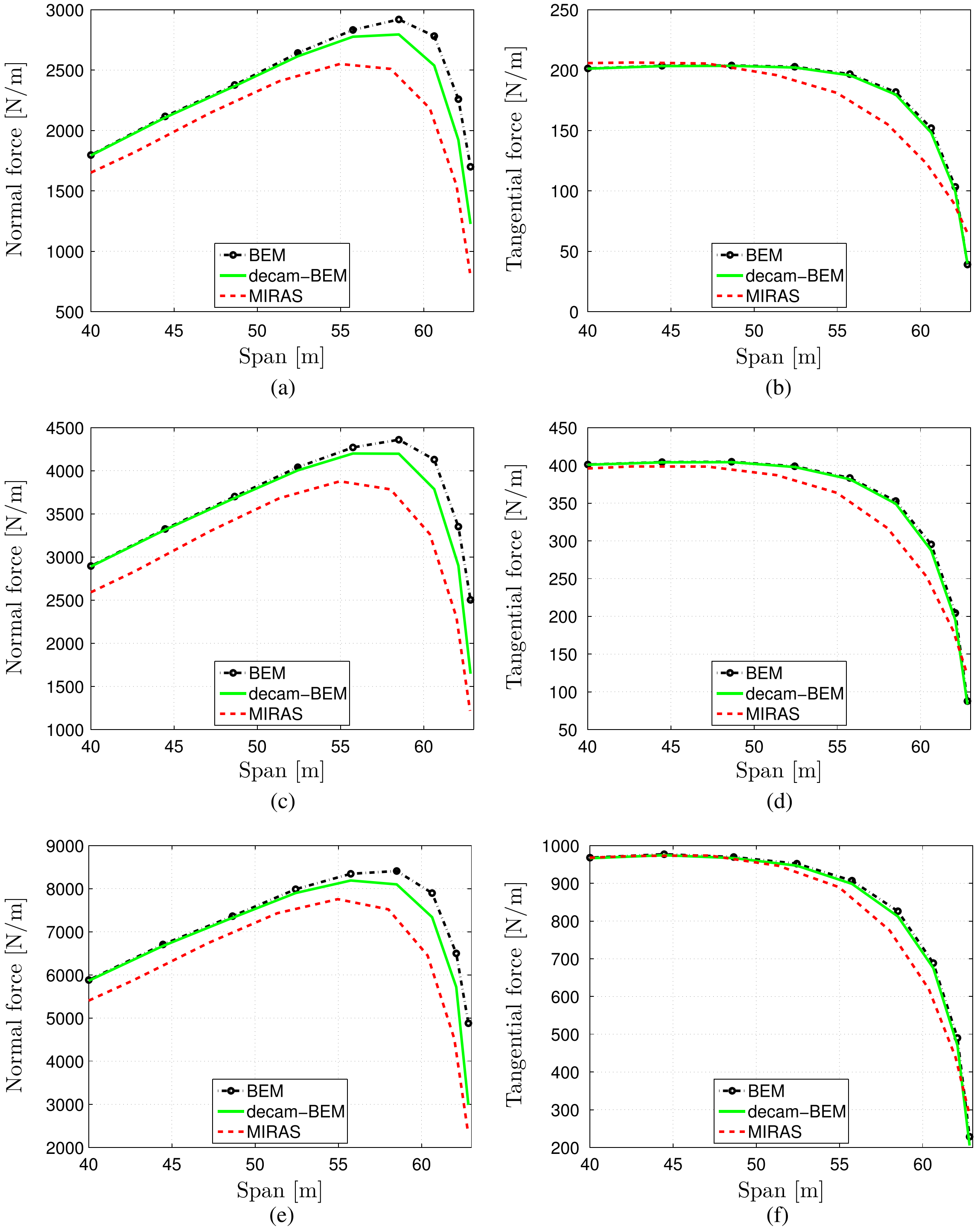

(a) (b)

(c) (d)

(e) (f)

Figure 12. Force distributions for the NREL 5-MW virtual rotor. (a) Normal force, $U_0 = 6\ \mathrm{ms}^{-1}$, (b) tangential force, $U_0 = 6\ \mathrm{ms}^{-1}$, (c) normal force, $U_0 = 8\ \mathrm{ms}^{-1}$, (d) tangential force, $U_0 = 8\ \mathrm{ms}^{-1}$, (e) normal force, $U_0 = 12\ \mathrm{ms}^{-1}$, (f) tangential force, $U_0 = 12\ \mathrm{ms}^{-1}$.

of the German–Dutch Wind Tunnel Organization DNW in a $9.5 \times 9.5\ \mathrm{m}^2$ open-test section. For the present analysis, two wind-speed cases are taken into account, 15 and 24 ms^{-1}. In both cases, the rotor angular velocity is set to 424.5 rpm, and the blades are subjected to a collective pitch of $-2.3°$. For more detailed information about the MEXICO experiment, the reader is referred to Schepers and Snel.[18]

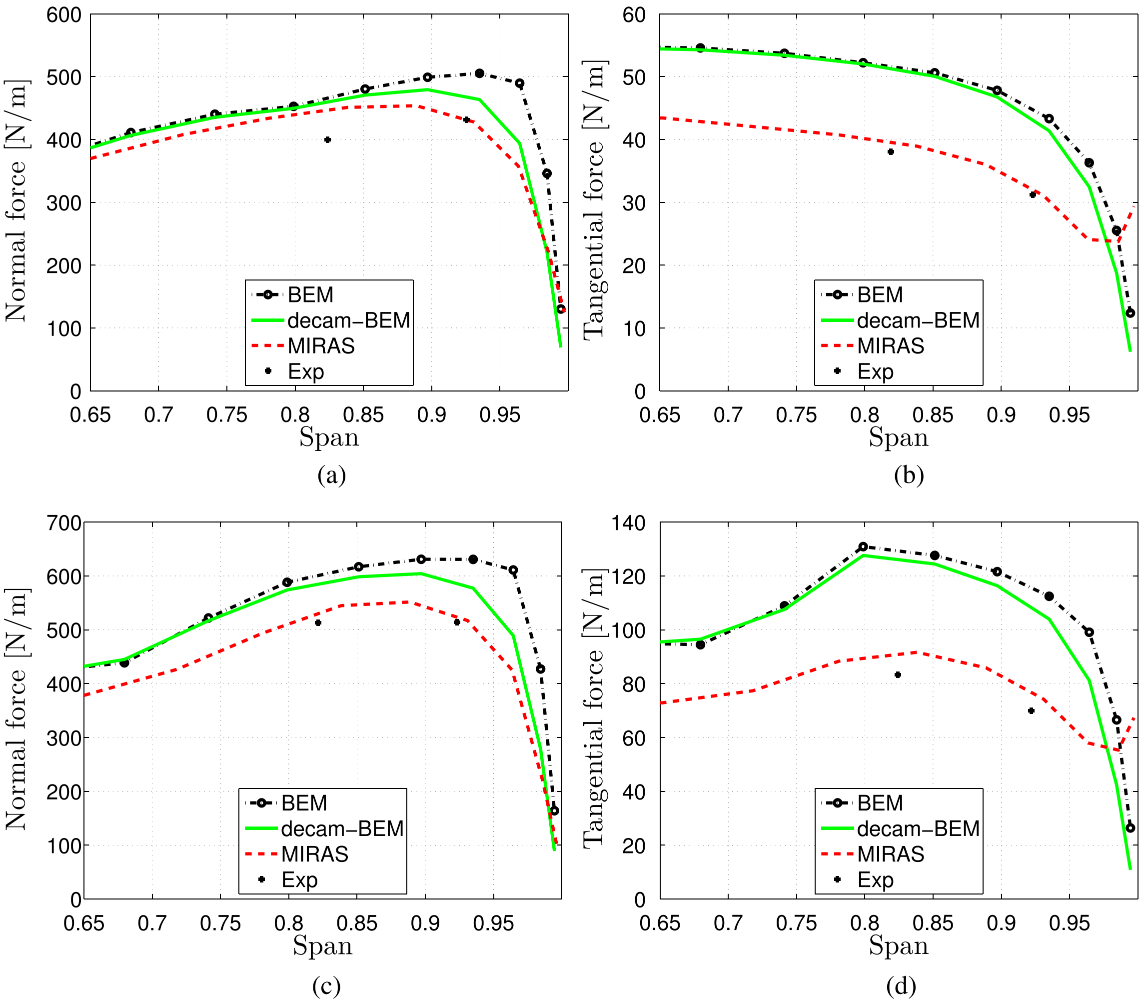

(a) (b) (c) (d)

Figure 13. Force distributions for the MEXICO model rotor. (a) Normal force, $U_0 = 15\ \mathrm{ms}^{-1}$, (b) tangential force, $U_0 = 15\ \mathrm{ms}^{-1}$, (c) normal force, $U_0 = 24\ \mathrm{ms}^{-1}$, (d) tangential force, $U_0 = 24\ \mathrm{ms}^{-1}$.

MIRAS simulations were performed using a surface mesh consisting of 20 spanwise and 50 chordwise cells for each of the three blades. In terms of wake discretization, a 20° angular discretization was used with a total amount of 20 simulated wake revolutions in all cases. Laminar to turbulent transition was forced to take place at 5% of the chord from the leading edge on both the upper and lower sides of the airfoil sections throughout the blade span.

The calculated normal and tangential forces for the wind speeds of 15 and 24 ms^{-1} are shown in Figures 13(a)–13(d). There is an excellent agreement between measured data and MIRAS simulations. For all cases, it is observed how the decambering correction applied to the BEM calculations bring the predicted values closer to the measured data. For the tangential forces the decambering effect has a slightly stronger influence than for the NREL 5-MW case, increasing with the wind speed. The decambering correction influences the normal force exclusively in the near tip region, rounding up its peak distribution in a similar fashion as the MIRAS calculations. However, the normal load from the BEM computations seems in all cases to be too high at the outer 40% of the blade, as compared with experiments and the MIRAS simulations.

5. CONCLUSIONS

A refined tip correction based on thin-airfoil theory and the induction from the vortices in the wake has been developed. The technique corrects the circulation obtained in lifting-line or BEM computations for the difference between a line load and a surface load using the so-called decambering approach. Decambering refers to the fact that the induction from the vortices in the wake by the airfoil is seen as an inverse cambering of the chord line. The resulting correction formula is derived by combining the Biot–Savart induction law with thin-airfoil theory. The developed correction has been implemented both in a lifting-line model and in a BEM model as an additional correction to the Prandtl tip correction. Comparisons with the results from a 3D panel code show that the new correction greatly improves the circulation at the outer part of the rotor blade. The comparison comprises both planar translating wings as well as one-bladed, two-bladed and three-bladed rotors, including the NREL 5-MW reference rotor and the Mexico model rotor. The correction is most significant for rotors with few blades, corresponding to rotor blades with low aspect ratios. For rotor blades with tapered tip geometries the correction mainly reduces the thrust at the outer part of the blade whereas the change in power performance is small. A main conclusion is that the inclusion of the decambering correction only changes slightly the predicted performance of the rotor, whereas it alleviates the loading by 7–8% at the outer part of the rotor blade.

ACKNOWLEDGEMENTS

The present work has been carried out with the support of the Danish Council for Strategic Research for the project Center for Computational Wind Turbine Aerodynamics and Atmospheric Turbulence (grant 2104-09-067216/DSF) (COMWIND). `http://www.comwind.org`

APPENDIX A: ERROR ESTIMATE FOR CENTER OF PRESSURE OFFSET

Assume a linear distribution of the additional induction as

$$\frac{\sum w}{V_{rel} cos\alpha} = a + (b-a)\left(\frac{x}{c}\right) \tag{A.1}$$

where a is the additional induction at the leading edge and $(b-a)$ is the slope. Then the local $\frac{d\eta}{dx}$ reads

$$\frac{d\eta}{dx} = \frac{\sum w - w_{c.p.}}{V_{rel}\cos\alpha} = (b-a)\left[\left(\frac{x}{c}\right) - \left(\frac{x}{c}\right)_{c.p.}\right] \tag{A.2}$$

From thin-airfoil theory, we have

$$\alpha_{L0} = -\frac{1}{\pi}(b-a)\int_0^{\pi}\left[\left(\frac{x}{c}\right) - \left(\frac{x}{c}\right)_{c.p.}\right](\cos\theta - 1)d\theta \tag{A.3}$$

and

$$\frac{x}{c} = \frac{1}{2}(1 - cos\theta). \tag{A.4}$$

By combining equations (A.3)–(A.4),

$$\alpha_{L0} = -\frac{1}{\pi}(b-a)\int_0^{\pi}\left[\frac{1}{2}(1 - cos\theta) - \frac{1}{2}(1 - cos\theta_{c.p.})\right](\cos\theta - 1)d\theta \tag{A.5}$$

$$\begin{aligned}
&\rightarrow \alpha_{L0} = -\frac{1}{2\pi}(b-a)\int_0^{\pi}[cos\theta_{c.p.} - cos\theta](\cos\theta - 1)d\theta \\
&\rightarrow \alpha_{L0} = -\frac{1}{2\pi}(b-a)\int_0^{\pi}[(cos\theta_{c.p.} + 1)cos\theta - cos^2\theta - cos\theta_{c.p.}]d\theta \\
&\rightarrow \alpha_{L0} = \frac{1}{2\pi}(b-a)\left[\frac{\pi}{2} + \pi\cos\theta_{c.p.}\right] = \frac{1}{4}(b-a)[1 + 2\cos\theta_{c.p.}] \\
&\rightarrow \alpha_{L0} = \frac{1}{4}(b-a)\left[1 + 2 - 4\left(\frac{x}{c}\right)_{c.p.}\right] \\
&\rightarrow \alpha_{L0} = (b-a)\left[\frac{3}{4} - \left(\frac{x}{c}\right)_{c.p.}\right]
\end{aligned} \tag{A.6}$$

and the relative error becomes

$$\frac{\Delta\alpha_{L0}}{\alpha_{L0,c/4}} = \frac{\alpha_{L0} - \alpha_{L0,c/4}}{\alpha_{L0,c/4}} = \frac{\left[\frac{3}{4} - \left(\frac{x}{c}\right)_{c.p.} - \frac{1}{2}\right]}{\frac{1}{2}} = \frac{1}{2} - 2\left(\frac{x}{c}\right)_{c.p.} \tag{A.7}$$

REFERENCES

1. Betz A. Schraubenpropeller mit geringstem energieverlust - mit einem zusatz von L. Prandtl. *Göttinger Klassiker der Strömungsmechanik* 1919; **3**: 68–88.
2. Goldstein S, *On the vortex theory of screw propellers*, Technical Report, St. Johns College, Cambridge, 1929.
3. Tollmien W, Schlichting H, Görtler H. *Ludwig Prandtl Gesammelte Abhandlungen zur angewandten Mechanik, Hydro- und Aerodynamik*. Springer-Verlag: Berlin-Göttingen-Heidelberg, 1961.
4. Glauert H. Airplane propellers, division 1. *Aerodynamic Theory* 1935; **4**: 169–360.
5. De Vries O. *Fluid Dynamic Aspects of Wind Energy Conversion. AGARDograph 243 ISBN 92-835-1326-6*. AGARD: Neuilly sur Seine, France, 1979.
6. Shen WZ, Mikkelsen R, Sørensen JN, Bak C. Tip loss corrections for wind turbine computations. *Wind Energy* 2005; **8**: 457–475.
7. Sørensen JN, Shen WZ. Numerical modelling of wind turbine wakes. *Journal of Fluids Engineering* 2002; **124**: 393–399.
8. Montgomerie B. De-camber: Explanation of an effect of lift reduction near the tip caused by the local flow around airplane wings or wind turbine tips. *Proceedings Plenary Meeting of the Group for Dynamic Stall and 3D Effects a European Union, Joule 2 Project*. Cranfield Institute of Technology, Cranfield, 1995, April 3–4.
9. Migliore PG, Wolfe WP, Fanucci JB. Flow curvature effects on Darrieus turbine blade aerodynamics. *Journal of Energy* 1980; **4**: 49–55.
10. Bianchini A, Ferrari L. A model to account for the virtual camber effect in the performance prediction of an H-Darrieus VAWT using the momentum models. *Wind Engineering* 2011; **35**: 465–482.
11. Mukherjee R, Gopalarathnam A. Poststall prediction of multiple-lifting-surface configurations using a decambering approach. *Journal of Aircraft* 2006; **43**: 660–668.
12. Katz J, Plotkin A. *Low-Speed Aerodynamics*. McGraw-Hill: New York, 2001.
13. Hansen MOL. *Aerodynamics of Wind Turbines* (2nd edn). Earthscan: London, 2008.
14. Ramos-García N, Sørensen JN, Shen WZ. A strong viscous-inviscid interaction model for rotating airfoils. *Wind Energy* 2014; **17**(12): 1957–1984.
15. Ramos-García N, Sørensen JN, Shen WZ. Validation of a three-dimensional viscous-inviscid interactive solver for wind turbine rotors. *Renewable Energy* 2014; **70**: 78–92.
16. Burton T, Sharpe D, Jenkins N, Bossanyi E. *Wind Energy Handbook*. John Wiley & Sons, Ltd: New York, 2002.
17. Jonkman J, Butterfield S, Musial W, Scott G, *Definition of a 5-MW Reference Wind Turbine for Offshore System Development*, Technical Report NREL/TP-500-38060, National Renewable Energy Laboratory, Golden, Colorado, USA, 2009.
18. Schepers JG, Snel H. Model Experiments in Controlled Conditions, *Final Report*. The Energy Research Center of the Netherlands: ECN-E–07-042, 2007.

PhD and Continuing Education
June 2016 | page 1/1

Technical University of Denmark

Joint author statement

If a thesis contains articles (i.e. published journal and conference articles, unpublished manuscripts, chapters etc.) made in collaboration with other researchers, a joint-author statement verifying the PhD student's contribution to each article should be made by all authors. However, if an article has more than three authors the statement may be signed by a representative sample, cf. article 12, section 4 and 5 of the Ministerial Order No. 1039 27 August 2013 about the PhD degree. We refer to the Vancouver protocol's definition of authorship.

A representative sample of authors is comprised of

- Corresponding author and/or principal/first author (defined by the PhD student), and if there are more authors:
- 1-2 authors (where appropriate, these should be the international/non-supervisor authors)

Title of the article	A new tip correction for actuator line computations
Author(s)	Kaya O. Dag and Jens N. Sørensen
Journal/conference * if applicable	Wind Energy
Name of PhD student	Kaya Onur Dag
Date of Birth	22.03.1989

Description of the PhD student's contribution to the abovementioned article

The correction was developed by the PhD student with supervision of the second author. The implementation of the new method and validations were conducted by the PhD student. Approximately half of the text and the figures were produced by the PhD student as well.

Signature of the PhD student

Date 29/05/2017

Signatures of co-authors

As a co-author I state that the description given above to the best of my knowledge corresponds to the process and I have no further comments.

Date (DD/MM/YY)	Name	Signature
29/05/2017	Jens N. Sørensen	

Joint author statements shall be delivered to the *PhD administration* along with the PhD thesis

WIND ENERGY
Wind Energ. 2017; **00**:1–14
DOI: 10.1002/we

RESEARCH ARTICLE

A new tip correction for actuator line computations

Kaya O. Dag and Jens N. Sørensen

DTU Wind Energy, Technical University of Denmark, 2800 Kongens Lyngby, Denmark

ABSTRACT

The actuator line method (ALM) is today widely used to represent wind turbine loadings in CFD computations. As opposed to resolving the whole blade geometry, the methodology does not require geometry-fitted meshes, which makes it relatively fast to apply. In ALM, tabulated airfoil data are used to determine the local blade loadings, which subsequently are projected to the CFD grid using a Gaussian smearing function. To achieve accurate blade loadings at the tip regions of the blades, the width of the projection function needs to be narrower than the local chord lengths, requiring CFD grids that are much finer than what is actually needed in order to resolve the energy containing turbulent structures of the atmospheric boundary layer (ABL). On the other hand, employing large widths of the projection function may result in too large tip loadings.Therefore, the actual number of grid points required to resolve the blade and the width of the projection function have to be restricted to certain minimum values if unphysical corrections are to be avoided. In this paper, we investigate the cause of the over estimated tip loadings when using coarse CFD grids, and, based on this, introduce a simple correction technique that only depends on the width of the projection function. First, the new correction is applied on a planar wing where results are compared with the lifting-line technique. Next, the NREL 5MW and Phase VI turbines are employed to test the correction on rotors. Here the resulting blade loadings are compared to results from the blade-element momentum (BEM) method. In both cases it is found that the new correction greatly improves the results for both normal and tangential loads, and that it is possible to obtain accurate results even when using a very coarse blade resolution. Copyright © 2017 John Wiley & Sons, Ltd.

KEYWORDS
actuator line, tip correction, wind turbine blade loadings, LES of wind turbines

Correspondence
DTU Wind Energy, Technical University of Denmark, 2800 Kongens Lyngby, Denmark

E-mail:kdag@dtu.dk

Received . . .

1. INTRODUCTION

The actuator line method (ALM) was developed as a numerical technique to facilitate the representation of the rotor blades in computational fluid dynamics (CFD) simulations of wind turbines [1]. The ALM is based on a blade-element approach in which body forces are introduced in the Navier-Stokes equations along lines representing the blades of the wind turbine. The body forces are obtained from tabulated airfoil data employing the local angle of attack along the blades as input. The local angle of attack is defined from the local local relative velocity, which is determined at each time step while running a simulation. After having determined the local forces, they are projected from the lines representing the rotor blades to the CFD grid points. A main issue of the technique is that it is required to smear out the body forces in order to avoid discontinuities in the resulting force distribution. This is typically carried out by using a 3D Gaussian filtering function with a given projection width ϵ, which eventually defines the thickness of the volume on which the blade forces are projected. It is known that very small ϵ-values cause oscillations in the flow field, whereas large values result in inaccurate loading distributions. There has been fair amount of work on determining the optimum value of the ϵ-parameter. Troldborg [2] suggested that fixing ϵ to twice the CFD grid resolution (Δ) is a good trade-off in between having high accuracy and avoiding oscillations in the flow field. In the work by Jha et al. [3], it was shown that oscillations could be avoided by using a blended dissipative scheme with $\epsilon = 2\Delta$. It was also noted that a constant ϵ parameter throughout the blade-span causes too large blade tip loadings. Additionally, Jha et al. [3] introduced a new methodology to vary the ϵ-parameter throughout the blade span in order to achieve a better loading distribution around the tip region. Their methodology improves the estimated loading distributions, but it also requires case-specific tuning of the parameter. In the work by Shives & Crawford [4], the effect of the ϵ-parameter and the resolution of the CFD grid was investigated for a fixed wing. For this case it was concluded that the ϵ-parameter should be in the order of $1/4c$, where c is the chord length of the local airfoil section. Further, they stated that, in order to be consistent with the vortex line approach, the self-induction at the vortex center should be zero. Their work also showed that ϵ-values smaller than 4Δ does not satisfy this condition. In a recent work by Martinez-Tossas et al. [5] a theoretical model based on the potential flow over a Joukowsky airfoil was developed to determine the optimum value of ϵ. Here it was concluded that for a grid resolution larger than the chord lengtht, the choise of the scale of the smoothing-kernel is dictated by the mesh, whereas for finner discretizations a value $\epsilon = 0.2c$ should be employed, which is in fact very close to the guidelines by Shives & Crawford [4].

Since the ALM is based on solving the three-dimensional Navier-Stokes equations around the actuator line, in principle, it is not needed to introduce a tip correction. However, when crude meshes are used there is no guarentee that the loading tends to zero at the tip, and therefore it is sometimes seen that researchers resort to the Prandtl/Glauert tip correction, which essentially is a technique for correcting the loading for finite number of blades effects in the momentum theory (see [6]). A technique for correcting the use of airfoil data near the tip was introduced by Shen et al. [7] by multiplying the lift coefficient by a function resembling the Prandtl tip-correction. This technique certainly improves the loading near the tip of the wing, but it is based on an empirical expression that may not be valid for all wing plan forms. An alternative correction of the one by Shen et al. [7] is the decamber correction introduced by Sørensen et al. [8]. This correction is based on the fact that the induction of the wake causes a curved streamline along the chord line that effectively corresponds to an additional camber of the airfoil. The correction was shown to be important for constant chord wings, but not significant for wing forms of modern wind turbines. Althogh there has been a lot of progress in determining the optimum ϵ-parameter and avoiding too high loadings near the tip when employing crude mesh resolutions, there is still an urgent need for deriving a consistent technique to determine mesh-independent solutions of the ALM. The aim of the present work is develop and validate such a technique.

The model we propose is based on the analogy there exists between the actuator line model and the inviscid lifting line model. In the lifting line model the wing is represented by a line consisting of a distribution of bound vortices. Each change in the strenght of the bound vortices results in the formation of a free trailing vortex, which is convected downstream by the local velocity field in the wake. In the lifting line model the free vortices induce a velocity field on the wing that alters the inflow and which ensures a smooth distribution of the circulation near the tip that eventually goes to zero at the very tip. Ideally, a solution to the Euler or Navier-Stokes equations employing the ALM should result in the same circulation distribution and wake vortex system as the lifting line model. However, the size of the smoothing kernel in the filtering function dictates the minimum resolution of the vortex kernel, and acts in principle as a viscous inner core. This modifies the induction of the wake vortices in the ALM as compared to the same wake obtained using a lifting line technique. The technique that we propose is a relatively simple correction in the induced angle of attack to compensate for the added influence of the viscous core. Although the correction is a method for correcting the additional induction of the smoothing-kernel, we refer to it as a tip correction, as it is at the tip that it is most pronounced.

DOI: 10.1002/we
Prepared using weauth.cls

The paper is structured as follows. In section 2 we briefly introduce to the ALM and show some results of computations without employing any corrections or by using directly the Prandtl tip correction. Next, in section 3, we introduce the proposed correction technique. In section 4 we show some results for both planar wings and rotors to validate the method. Finally, in section 5 we conclude the work.

2. NUMERICAL METHODS

2.1. Large Eddy Simulation Tool

The numerical tool used in this study is an incompressible pseudo-spectral Large Eddy Simulation (LES) solverl that has recently been developed at DTU Wind Energy. The code uses Fourier series to discretize the horizontal directions, and a second-order central finite difference scheme in the vertical direction. The pseudo-spectral computation of the non-linear terms in the momentum equations are fully dealiased with zero-padding operation. For the time integration, a second-order Adams-Bashforth scheme is used with a pressure-splitting technique, where the momentum equations are used to advance in time with the pressure field from the previous time step. The Poisson equation is subsequently solved directly to obtain the new pressure to project the velocities to a divergence free field. For the sub-grid-scale (SGS) modeling, a Smagorinsky model with a fixed constant of $C_s = 0.18$ is employed for the current study. Since Fourier series enforce periodicity in spanwise and streamwise axes, a buffer zone is used to gradually adjust the streamwise outgoing velocity to the desired, uniform, inflow condition. The length of the buffer zone is selected as 15% of the streamwise domain length. For the bottom and top boundaries, a stress-free condition is used. The forcing term from the wind turbine rotor is added as an additional term to the the momentum equations as

$$\frac{\partial U}{\partial t} = RHS + \boldsymbol{f_b}. \tag{1}$$

RHS here represents the advective, diffusion and pressure terms in the momentum equations and f_b is the body force obtained with ALM. The calculation of this term is detailed below. For more details about the code, we refer to the PhD dissertation of Dag [9].

2.2. The Actuator Line Technique

In ALM, the turbine blades are represented as distributed body forces on a line that is assumed to be located at the quarter-chord line of the blade, as illustrated in Fig.1. The velocity of the overall flow field is described in a global coordinate system, (x, y, z), with the origin located at the centerof the wind turbine rotor, the x-axis pointing downstream along the axis of the rotor, and the y- and z-axes perpendicular to this, as illustrated in Fig. 1. With the z-axis pointing upward in the vertical direction, an angle θ defines the azimuthal position of one of the blades, with the three blades located an angle $\Delta\theta = 2\pi/3$ from each other. To determine the relative velocity, as it is seen from the rotor blade, a local co-rotating coordinate system (r, θ, z) is utilized. This coordinate system is located in the rotor plane at a radial distance, r, from the rotor axis, and with the x-axis pointing in the same direction as in the global system and with θ defining the azimuthal coordinate direction. To calculate the body forces, tabulated airfoil data and the angle of attack are used in a blade-element approach. First, the velocities from the flow solver, denoted (u_x, u_y, u_z), are interpolated to the velocity values on the actuator line points, referred to as (u_x, u_y, u_z). Here Ω is the rotational speed of the rotor, r is the blade

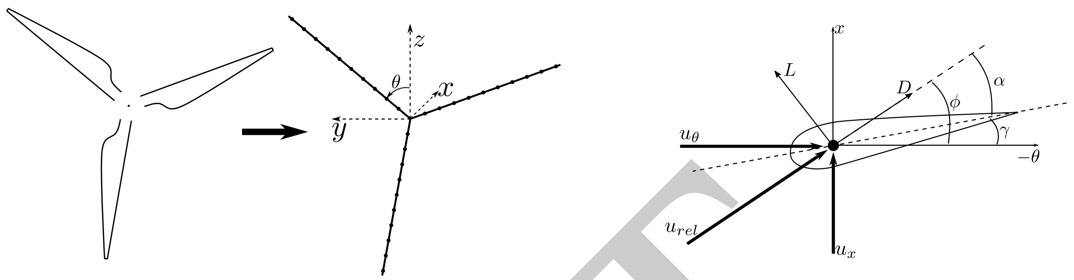

Figure 1. Illustration of the actuator line model (left), and local angles of a blade cross-section (right).

radius and the local relative azimuthal velocity of the blade is given as

$$u_\theta = \Omega r - \big(u_y\, cos(\theta) + u_z\, sin(\theta)\big)^{*}. \tag{2}$$

Then, the flow angle for each actuator line point is obtained as

$$\phi = \tan^{-1}(u_x/u_\theta), \tag{3}$$

which then used together with the local twist and the pitch angle of the blade (γ) to obtain angle of attack values (α) for each actuator line point

$$\alpha = \phi - \gamma. \tag{4}$$

Next, the lift and drag forces for unit span is obtained with

$$f_L = \frac{1}{2}\,\rho\, u_{rel}^2\; c\; C_L, \tag{5}$$

$$f_D = \frac{1}{2}\,\rho\, u_{rel}^2\; c\; C_D, \tag{6}$$

where $u_{rel} = \sqrt{u_\theta^2 + u_x^2}$ is the relative velocity, c is the chord length and C_L and C_D are the local lift and the drag coefficients. At this stage, these forces are projected to tangential and normal components by using the local flow angles as

$$f_\theta = f_L\;\sin(\phi) - f_D\;\cos(\phi), \tag{7}$$

$$f_n = f_L\;\cos(\phi) + f_D\;\sin(\phi). \tag{8}$$

Then in grid coordinates these forces read

$$f_x = -f_n, \tag{9}$$

$$f_y = -f_\theta\; cos(\theta), \tag{10}$$

$$f_z = f_\theta\; sin(\theta). \tag{11}$$

Applying these forces directly to the closest CFD grid point would produce oscillations, thus a filtering procedure is applied by using a 3D Gaussian filtering function which is a function of the distance d that is determined individually for each

---

[*] For the simplicity, the rotor plane is assumed to be perpendicular to the flow

DOI: 10.1002/we
Prepared using weauth.cls

grid-actuator line point couple as

$$d_{i,j,k}^{N,m} = \sqrt{(x_{i,j,k} - x^{N,m})^2 + (y_{i,j,k} - y^{N,m})^2 + (z_{i,j,k} - z^{N,m})^2}. \tag{12}$$

Here (i,j,k) are indices that refer to the $(x,\, y,\, z)$ axes in the global coordinate system, and superscript N, m represent the blade and actuator line point indices respectively. The the 3D Gaussian filter kernel reads

$$\eta_{i,j,k}^{N,m} = \frac{1}{\epsilon^3 \pi^{(3/2)}} exp\left[-\left(\frac{d_{i,j,k}^{N,m}}{\epsilon} \right)^2 \right], \tag{13}$$

with η is the kernel and ϵ-parameter defines the size of this kernel. With the known kernel, body forces $\boldsymbol{f_b}$ in momentum equations are determined with

$$\boldsymbol{f_{b(i,j,k)}} = \sum_N \sum_m \eta_{(N,m,i,j,k)} \begin{bmatrix} f_{x(N,m)} \\ f_{y(N,m)} \\ f_{z(N,m)} \end{bmatrix}. \tag{14}$$

2.3. Results using present formulation of the ALM

To demonstrate the inadequacy of using a crude mesh in the ALM , blade loading distributions of NREL Phase VI rotor is computed for a steady flow case on a relatively course mesh with a rotor resolution of 10 mesh points along the rotor radius. It should be noted that, as a general guideline, the minimum resolution of the wing should be around 30-50 grid points along the rotor radius. The main geometry and operational conditions of the rotor are given in Table I. The size of the employed domain is $[L_x, L_y, L_z] = 180 \times 60 \times 60$ m. The grid resolution is $\Delta = \Delta x = \Delta y = 0.5$ m and $\Delta z = 0.25$ m, with x and y being the axes parallel to the ground, and z the vertical axis. With this grid setting, a filter kernel $\epsilon = 3\Delta = 1.5m$ is used for the actuator line forces. The resulting normal and tangential loading distributions are shown in Fig. 2. To demonstrate the problems of representing correctly the tip loading when using course meshes, the ALM computations are compared to results from a similar blade-element momentum (BEM) computation and an ALM computation using the Prandtl tip corection. As seen in the figure, at the inner parts of the blade, the loadings from BEM and ALM match well. However, at the tip region an overestimation of the ALM loadings are clearly seen. Furthermore, the loading do not tend to zero at the very tip. Correcting the load distribution by the Prandtl tip correction, however, does not the remedy the situation, as the loading the becomes highly underestimated. As will be shown later, this problem only occurs when using a crude mesh. However, it is not always possible to carry out computations on sufficiently fine meshes, and there is obviously a need for a technique that may produce accurate results on crude meshes.

Table I. Operation conditions for NREL Phase VI rotor

Rotor diameter	10.058 m
Root cut out	0.9 m
Rotational speed	7.50107 rad/s
Pitch angle	3°
Cone angle	0°
Wind speed	7 m/s

2.4. Influence of kernel size

To further investigate the over-shooting issue of the ALM, we here simplify the case and apply the ALM for a non-rotating rectangular wing. To have a reference circulation distribution, the lifting line technique (LLT) is used for the same wing and results are compared with those obtained from ALM with different kernel sizes of the filtering function. The

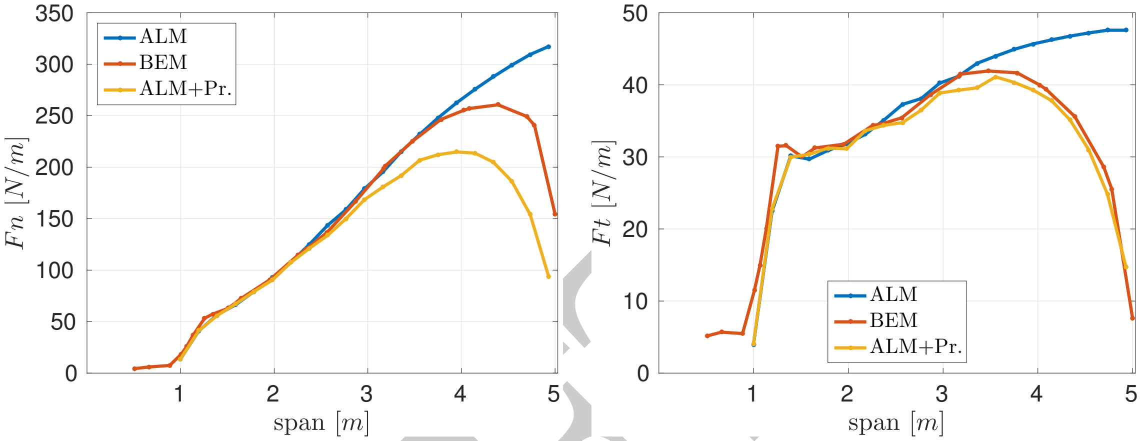

Figure 2. Comparison of loading distributions from BEM and ALM and ALM with Prandtl's correction for NREL Phase VI rotor operating under 7 m/s steady inflow

rectangular wing used in this study has a constant chord length of 1 m with a span length of 10 m. The wing is positioned at a geometrical angle of attack of 5°, and the incoming velocity is fixed at 8 m/s. Inviscid airfoil data of the NACA 0012 airfoil is used for both ALM and LLT. For the ALM computations, different ϵ-values are used together with a domain size of 50×30×20 m, with a varying grid resolution and a fixed kernel value $\epsilon/\Delta = 2$. A comparison of the circulation distributions is presented below in Fig.3. Due to symmetry, only the half-span is shown in the plot. In the LLT case, due to the strong tip vortices, the induction goes to infinity at the very tip of the wing, which causes the circulation to approach zero at the tip. This is not the case for the ALM where the circulation for all ϵ-values is seen to increase near the tip. On the other hand, with decreased ϵ-values, the ALM circulation levels converge towards the LLT results, yet with a peak at the tip region. This behavior can only be explained by an under-estimated wake induction near the tip, causing an increased angle of attack, which results in a stronger circulation.

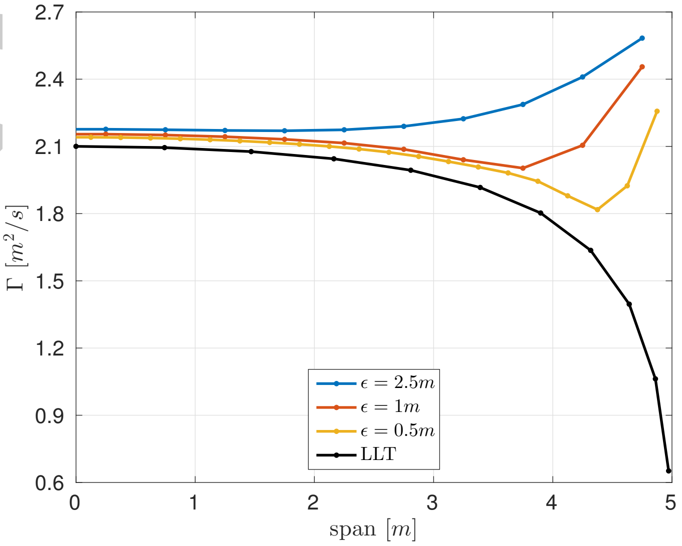

Figure 3. Comparison of circulation distributions from LLT and ALM with different ϵ values for AR=10 wing.

DOI: 10.1002/we

In order to clarify the effect of the ϵ-parameter on the bound vortices, an infinitely long wing with constant circulations is employed as model example. In this case the bound vortex generated by the ALM can be studied without being disturbed by the influence of the free vortices. The outcome of this is shown in Fig. 4, where the computed normal velocity distribution is shown for different ϵ/Δ-values. What is seen here is esentially the velocity distribution induced by a two-dimensional vortex which is being filtered by the Gaussian filter function. A high ϵ-value tends to smear out the velocity whereas a small ϵ-value results in a more distinct velocity distribution, tending towards the inviscid value of $\frac{\Gamma}{2\pi r}$. An important part of the ALM is to determine the local angle of attack as this forms the input to the airfoil data. Since the angle of attack is determined from the local velocity, as shown in eqs. 1-3, the induction from a vortex with a high ϵ-value tends to overpredict it, with the result that the loadings become overestimated. It should be emphasized that it is not the induction of the bound vortex per se that defines the angle of attack, but the induction from the free vortices in the wake (see e.g. [?]). However, since these vortices are born by the bound vortex, they have the same viscous core size as the bound vortex. A quick remedy to this problem would be to use smaller ϵ-values. However, it is known that such an approach decreases the accuracy of the physical location of the vortex origin and causes instabilities in the CFD results. Instead, based on the knowledge gained from the shown comparative study, we will in the next section develop a methodology for correcting the induced velocity when determining the angle of atttack.

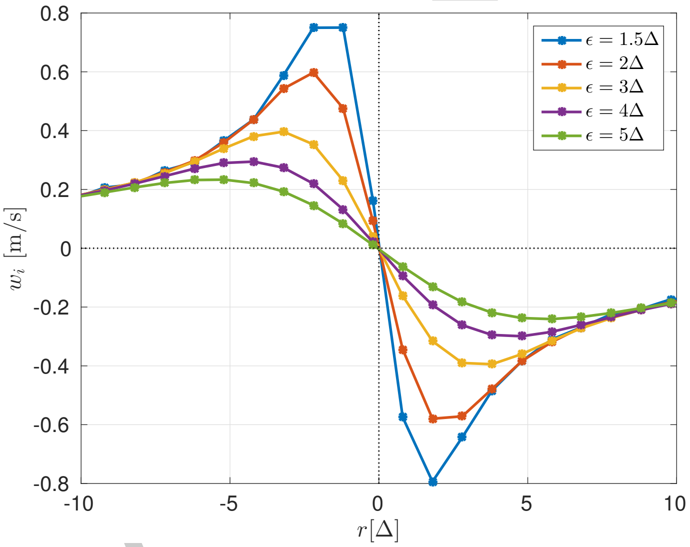

Figure 4. Induction change observed with different ϵ values.

3. CORRECTION METHODOLOGY

To account for the missing induction, it is noted the Lamb-Oseen vortex model ([10]) is equal to the employed filtering function and results in the exact same induction as the one obtained from an ALM computation with viscous core size corresponding to the size of the smoothing-kernel ϵ. The analytic formulation of a semi-infinite Lamb-Oseen vortex model is given as,

$$w_i = \frac{\Gamma}{4\pi r}\left(1 - exp\left(\frac{-r^2}{r_{vc}^2}\right)\right), \tag{15}$$

where Γ is the vortex strength and r_{vc} is the viscous core size. From this expression it is readily seen that the the first term corresponds to the inviscid part of the induction and the the second term accounts for the indfluence of the viscous core. In Fig. 5 it is shown that, by replacing r_{vc} with the ϵ-values used in an ALM computation, the vortex model gives the exactly same distribution of induced velocities.

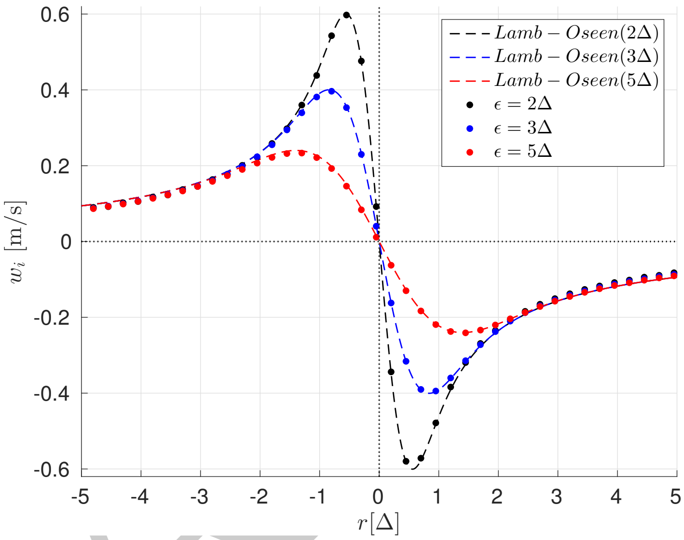

Figure 5. Comparison of Lamb-Oseen vortex model with induction levels obtained from CFD computation with given ϵ-parameter.

Hence, by subtracting the viscous part from the induction of the Lamb-Oseen model, one may establish a model for correcting the unwanted influence of the viscous core on the induced velocity,

$$w_{corr} = \frac{\Gamma}{4\pi r} exp\left(\frac{-r^2}{\epsilon^2}\right). \tag{16}$$

As the bound vortex does not contribute to the induced velocity defining the angle of attack (the angle of attack is essentially determined at the center of the bound vortex), the correction is applied on the trailing vortices in the wake, which then corrects the induced velocity through the Biot-Savart induction law. However, to do this it is required to know the position and induction of the wake vortices.

3.1. Application procedure

3.1.1. Planar wing

The correction is meant to be applied at the angle of attack calculation stage, where the total additional induction from the wake system w_{corr} is added to the local relative velocity and angle of attack value is altered. To apply the correction, the location of the wake vortices and their strengths have to be defined in advance as these are required by the Eq. 16. For a planar wing application, wake vortices can be assumed to form a straight vortex sheet which is parallel to the flow and trail from the quarter-chord line of the wing (see the Fig.6). Then, for each actuator line point, the total correction from the viscous cores of the wake vortices can be calculated as

$$w_{corr(i)} = \sum_{j=1}^{N+1} \frac{\Gamma_{w(j)}}{4\pi r_{(i,j)}} exp\left(\frac{-r_{(i,j)}^2}{\epsilon^2}\right). \tag{17}$$

The N here is the total number of actuator line points on and Γ_w here represents the circulation strength in the wake vortices, and the magnitudes are equal to the difference between the two neighboring bound circulations where the wake vortex trails,

$$\Gamma_{w(j)} = \Gamma_{(j)} - \Gamma_{(j-1)}. \tag{18}$$

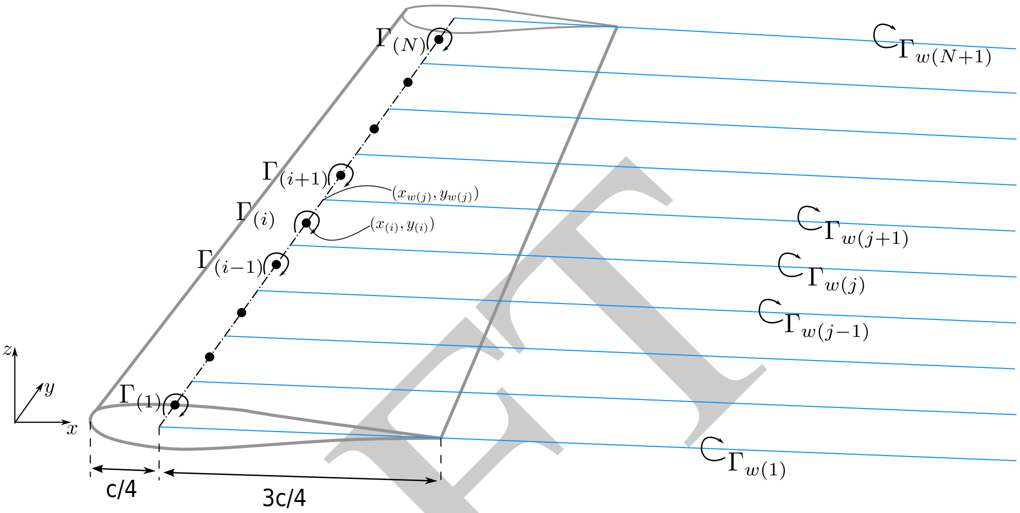

Figure 6. Illustration of a vortex system of a planar wing

For the tip vortices, the magnitudes are equal to the bound circulations which are closest to the tips. In this system, strength of a bound circulation is a function of the corresponding chord c, relative velocity u_{rel} and the lift coefficient C_L,

$$\Gamma_{(i)} = \frac{1}{2}\, c_{(i)}\, C_{L(i)}\, u_{rel(i)}. \tag{19}$$

In Eq.17, r variable is defined individually for each trail-actuator line point couple. The definition in the given coordinate system [†] (see Fig.6) can be written as

$$r_{(i,j)} = y_{(i)} - y_{w(j)}. \tag{20}$$

With the known total induction correction, angle of attack values on each actuator line point can be corrected by simply accounting the additional induction,

$$\alpha_{(i)} = \alpha_g - tan^{-1}\left(\frac{-u_{z(i)} + w_{corr(i)}}{u_{rel(i)}}\right). \tag{21}$$

In Eq. 21 α_g represents the geometrical angle of attack of the wing, u_{rel} and u_z are the relative and the vertical velocity components respectively. An illustration of the induction correction for a single vortex line is shown in Fig. 7. In the figure, the dashed blue line represents the underestimated induction from the tip vortex in the CFD computation, which causes over estimated tip loadings. The thick blue line is the induction that would occur in a LLT case. Hence, the red swept are is the induction correction which correct the angle of attack values at the region. The consequence of modifying the values of angle of attack, bound vorticity and, hence, the strengths of the wake vortices change. Therefore, the correction requires an iterative procedure in each time step of the CFD computation.

3.1.2. Wind turbine rotor

Application procedure for a turbine rotor is similar to the wing case. The only difference is due to the wake structure, which adds a level of complication to the calculation. Due to the three-dimensional formation of the wake (see Fig. 8 (left)), it is needed to define a discrete vortex lines and calculate the induction correction in three-dimensional space accordingly.

[†] Note that span of the wing is aligned with the y axis for the simplicity.

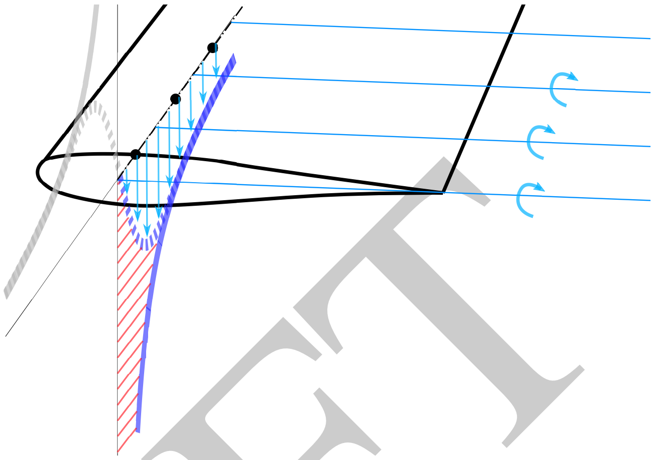

Figure 7. Illustration of the induction correction for the tip vortex

By using the vector notation, the induction correction from a vortex line can be calculated as

$$\begin{bmatrix} w_{xcorr} \\ w_{ycorr} \\ w_{zcorr} \end{bmatrix} = \frac{\Gamma}{4\pi}\frac{\vec{dl}\times\vec{r}}{|\vec{r}|^{3}}\left(exp\frac{-|\vec{r}|^{2}}{\epsilon^{2}}\right), \tag{22}$$

where $\vec{dl}$ is the the vector represents the direction and the length of the vortex line, $\vec{r}$ is the vector from the center of the vortex line to the induction calculation point (see Fig. 8 (right)). Then for each actuator line point the total induction correction can be calculated by summing all the corrections from the wake system as

$$\begin{bmatrix} w_{xcorr} \\ w_{ycorr} \\ w_{zcorr} \end{bmatrix}_{(N,m)} = \sum_{h}\sum_{p}\sum_{q}\frac{\Gamma_{w(h,p,q)}}{4\pi}\frac{\vec{dl}_{(h,p,q)}\times\vec{r}_{(h,p,q,N,m)}}{|\vec{r}_{(h,p,q,N,m)}|^{3}}\left(exp\frac{-|\vec{r}_{(h,p,q,N,m)}|^{2}}{\epsilon^{2}}\right). \tag{23}$$

Here, the indices h,p and q represent the blade number, span position and the azimuthal position respectively for the wake vortices, and N and m represent the blade number and span position for actuator line points (see Fig.8 (right)). The circulation strengths are calculated similar to the planar case as

$$\Gamma_{(N,m)} = \frac{1}{2}\, c_{(N,m)}\, C_{L(N,m)}\, u_{rel(N,m)}, \tag{24}$$

and

$$\Gamma_{w(h,p,q)} = \Gamma_{(p-1,q)} - \Gamma_{(p,q)}. \tag{25}$$

With the calculated total induction correction for each actuator line point, the flow angle can be corrected as

$$\phi_{(N,m)} = tan^{-1}\left(\frac{u_{x(N,m)} + w_{xcorr(N,m)}}{u_{\theta(N,m)} + w_{\theta corr(N,m)}}\right), \tag{26}$$

where

$$w_{\theta corr(N,m)} = w_{ycorr(N,m)}\, cos(\theta_N) + w_{zcorr(N,m)}\, sin(\theta_N). \tag{27}$$

Next, the new angle of attack values can be computed locally by the Eq.4.

To generate the discrete wake, we assumed that the helical pitch of the each individual trailing vortex is constant and equal to the relative flow angle at the position where the trailing vortex is released. Since the flow angle is updated in every time-step depending of the local flow conditions, this gives a queasy-steady behavior for the correction. In this work, the length of the helical vortex sheet is fixed at two full revolutions, and the azimuthal discretization of the wake is made with 2° intervals.

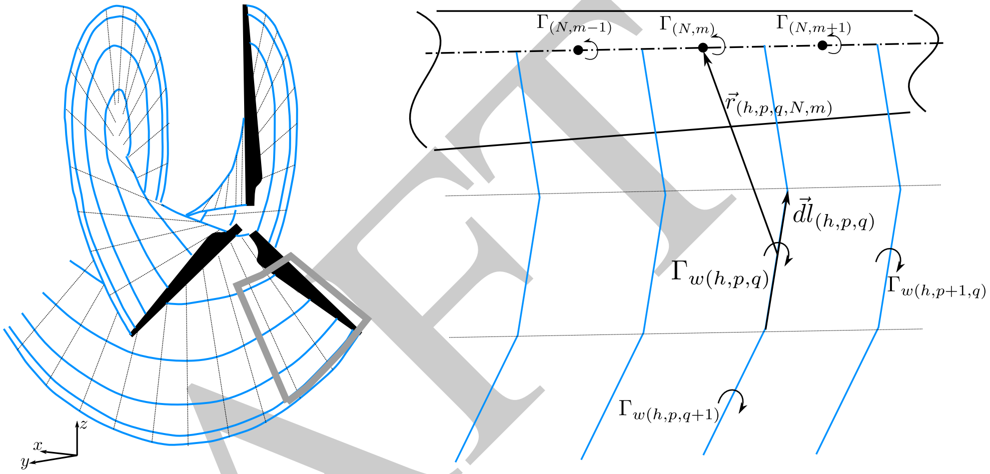

Figure 8. Illustration of the helical wake released from a wind turbine rotor(left), a close-up illustration of the wake formation of the single blade(right).

4. RESULTS

4.1. Planar wing

To validate the new correction, we first compute the flow past a tranlating rectangular wing with a constant chord $c = 1m$ and aspect ratios 6 and 10. For the ALM computations, a CFD grid resolution of $100 \times 60 \times 80$ is used. This resolution corresponds to $\Delta = 0.5$ m in the span-wise and stream-wise directions, and 0.25 m in the vertical direction. The filter parameter, ϵ, is taken as a chord length, which corresponds to 2Δ for any given grid resolution. The inflow velocity is fixed at 8 m/s and the geometrical angle of attack for both wings is 5°. In Fig. 9, circulation distributions are plotted for both wings and compared against LLT computations. In the figure, the corrected ALM computations are shown as *ALM**, and, due to symmetry, only the half-span distributions are shown.

As seen from the figure, the overestimation of the tip circulations is visible in the ALM simulations, with a peak value that is higher than the maximum circulation occurring at the middle section of the wing. Applying the new correction fixes the issue and provides comparable results with LLT. Additionally, it is important to note that it is not only at tip region, but also at the mid-regions, that the correction provides circulation levels similar to LLT computations.

4.2. Wind turbine rotor

For rotor applications, in order to cover a wider range of possibilities with minimum computation we used two distinctive rotors namely NREL Phase VI and NREL 5MW. The Phase VI is a two-bladed rotor with tip speed ratio of 5.39 and blade aspect ratio at an average of 7.5, whereas the 5MW rotor is a three-bladed type operating at a higher tip speed ratio of 7.55, with slender blades of an average aspect ratio of 15.8. The operating conditions of the rotors are detailed in Table II.

For this study we have conducted 8 simulation cases for each rotor. For the Phase VI rotor, a domain size of

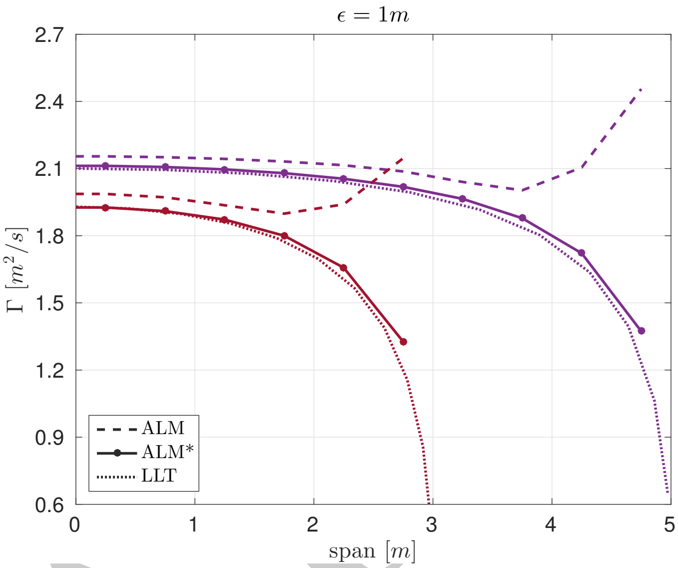

Figure 9. Comparison of circulation distribution obtained from ALM, corrected ALM (ALM*) and LLT computations for planar wings with AR=6,10

	PHASE VI	**5MW**
Rotor type	2-bladed	3-bladed
Tip speed ratio	5.39	7.55
Blade aspect ratio	7.5	15.8
Rotor diameter	10.058 m	126 m
Root cut out	0.9 m	5 m
Rotational speed	7.50107 rad/s	0.9584 rad/s
Pitch angle	3°	0°
Cone angle	0°	0°
Wind speed	7 m/s	8 m/s

Table II. Operation conditions for NREL Phase VI and 5MW rotors

$180 \times 60 \times 60$ m is used and the rotor center is positioned at $20 \times 30 \times 30$ m, whereas for the 5MW rotor, a domain size of $1512 \times 504 \times 504$ m is employed and the rotor center is positioned at $252 \times 252 \times 252$ m. For both domains, the blockage effects are checked and it is concluded that current domain sizes are sufficient. Further details of the CFD cases are provided in Table III. In the table, Δt represents the time step size in CFD computation, which is restricted to be smaller than the time it takes for a blade tip to travel one grid spacing. The total number of time steps for each simulation are shown in the table as $tsMax$. Before fixing the blade loadings, simulations were run long enough for the wake to develop. The number of time steps where the loading is fixed and averaged over is shown under $tsAvg$. The r/Δ and $nrAero$ columns show the number of CFD grid points per radius and number of aerodynamic control points used in the blades respectively. Additionally, the figure in which the corresponding data set is presented is addressed in the $dataFig$ column.

The resulting normal and tangential loading distributions are plotted against BEM computations in Fig. 10 and Fig. 11 for the Phase VI and the 5MW rotors, respectively. Although there are experimental data available for the Phase VI turbine, since the problem we are trying to fix is a numerical issue, in order to avoid introducing additional unknown parameters we did not compare our results against measurements. As seen from the figures, correction provides great improvement in all the tested cases. For the Phase VI rotor, the corrected results are in good agreement with BEM computations for both coarse and fine resolutions and for two different projection widths. For the 5MW rotor, in coarse

simNr.	rotor	resolution	Δ[m]	r/Δ	ϵ[m]	$\epsilon^*(\epsilon/\Delta)$	nrAero	tsMax	Δt[s]	tsAvg	correction	dataFig
1	P6	180x60x120	2	5	6	3	11	3E3	4.3E-2	250	✓	Fig. 10-upper
2	P6	180x60x120	2	5	6	3	11	3E3	4.3E-2	250	-	Fig. 10-upper
3	P6	180x60x120	2	5	10	5	11	3E3	4.3E-2	250	✓	Fig. 10-upper
4	P6	180x60x120	2	5	10	5	11	3E3	4.3E-2	250	-	Fig. 10-upper
5	P6	720x240x480	0.5	20	1.5	3	21	20E3	2E-3	1E3	✓	Fig. 10-lower
6	P6	720x240x480	0.5	20	1.5	3	21	20E3	2E-3	1E3	-	Fig. 10-lower
7	P6	720x240x480	0.5	20	2.5	5	21	20E3	2E-3	1E3	✓	Fig. 10-lower
8	P6	720x240x480	0.5	20	2.5	5	21	20E3	2E-3	1E3	-	Fig. 10-lower
9	5MW	120x40x80	12.6	5	37.8	3	10	8E3	3.9E-2	250	✓	Fig. 11-upper
10	5MW	120x40x80	12.6	5	37.8	3	10	8E3	3.9E-2	250	-	Fig. 11-upper
11	5MW	120x40x80	12.6	5	63	5	10	8E3	3.9E-2	250	✓	Fig. 11-upper
12	5MW	120x40x80	12.6	5	63	5	10	8E3	3.9E-2	250	-	Fig. 11-upper
13	5MW	480x160x320	3.15	20	9.45	3	20	24E3	1.3E-2	1E3	✓	Fig. 11-lower
14	5MW	480x160x320	3.15	20	9.45	3	20	24E3	1.3E-2	1E3	-	Fig. 11-lower
15	5MW	480x160x320	3.15	20	15.75	5	20	24E3	1.3E-2	1E3	✓	Fig. 11-lower
16	5MW	480x160x320	3.15	20	15.75	5	20	24E3	1.3E-2	1E3	-	Fig. 11-lower

Table III. Details of the CFD cases for rotor simulations

resolution cases correction application lowers the peak error from 23% to 5% and 77% to 17% respectively for the normal and tangential loads. In the finer grid case, the results are again in good agreement with BEM computations for both ϵ-values.

5. DISCUSSION AND CONCLUSIONS

In this paper, a new correction for actuator line computations is presented and tested with two planar wings and two wind turbine rotors. It is shown that the overestimation of the tip loads due to the force projection operation can be cured with application of the new correction, even with very low CFD grid resolutions. For both turbine rotors, correction showed great improvement in blade loadings for grid resolutions as little as 5 grid points per radius. Although, correction applied ALM computations for the Phase VI rotor resulted with load levels which are very close to BEM computations, the 5MW rotor cases showed that such low resolution may still result with slightly off tangential loads even with applied correction. For both turbines, it can be concluded that CFD resolutions that correspond to 20 grid points per radius is sufficient with $\epsilon = 3\Delta$ or $\epsilon = 5\Delta$ and the results are in good agreement with BEM computations for both normal and tangential loadings.

REFERENCES

1. J. N. Sørensen and W. Shen, "Numerical modeling of wind turbine wakes," *Journal of Fluids Engineering*, 2002.
2. N. Troldborg, *Actuator Line Modeling of Wind Turbine Wakes*. PhD thesis, DTU, 2008.
3. P. K. Jha, M. J. Churchfield, P. J. Moriarty, and S. Schmitz, "Guidelines for volume force distrubutions within actuator line modeling of wind tturbine on large-eddy simulation-type grids," *Journal of Solar Energy Engineering*, 2014.
4. M. Shives and C. Crawford, "Mesh and load distribution requirements for actuator line cfd simulations," *Wind Energy*, 2013.

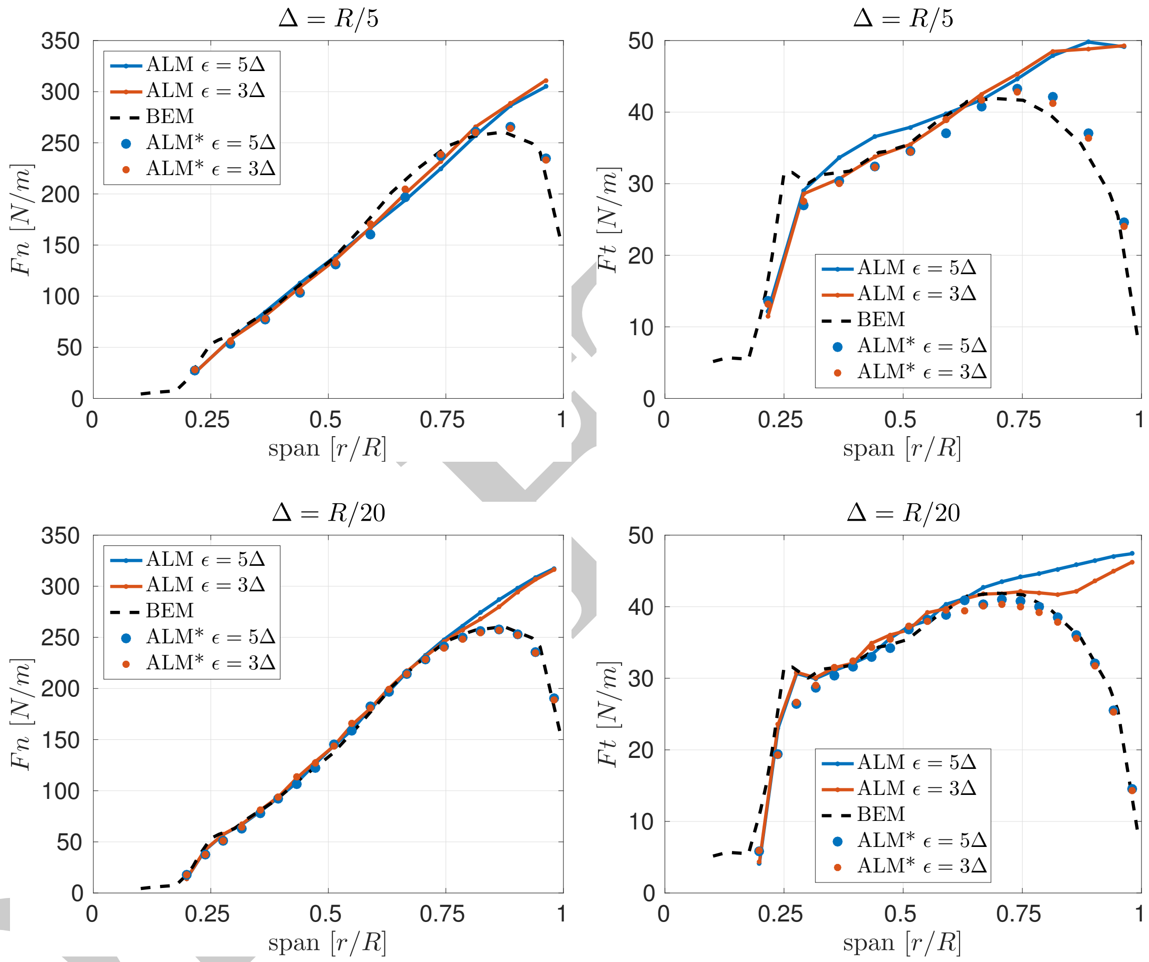

Figure 10. Comparison of normal and tangential loadings from ALM with and without the correction, and BEM computations for NREL Phase VI turbine.

5. L. A. Martínez-Tossas, M. J. Churchfield, and C. Meneveau, “Optimal smoothing length scale for actuator line models of wind turbine blades,” *Wind Energy*, 2017.
6. J. N. Sørensen, *General Momentum Theory for Horizontal Axis Wind Turbines*. Springer, 2016.
7. W. Z. Shen, J. N. Sørensen, and R. Mikkelsen, “Tip loss correction for actuator/navier-stokes computations,” *Journal of Solar Energy Engineering*, 2005.
8. J. N. Sørensen, K. O. Dag, and N. R. García, “A refined tip correction based on decambering,” *Wind Energy*, 2016.
9. K. O. Dag, *Combined pseudo-spectral / actuator line model for wind turbine applications*. PhD thesis, Technical University of Denmark Department of Wind Energy, May 2017.
10. H. Lamb, *Hydrodynamics, 6th ed.* Cambridge University Press, 1932.

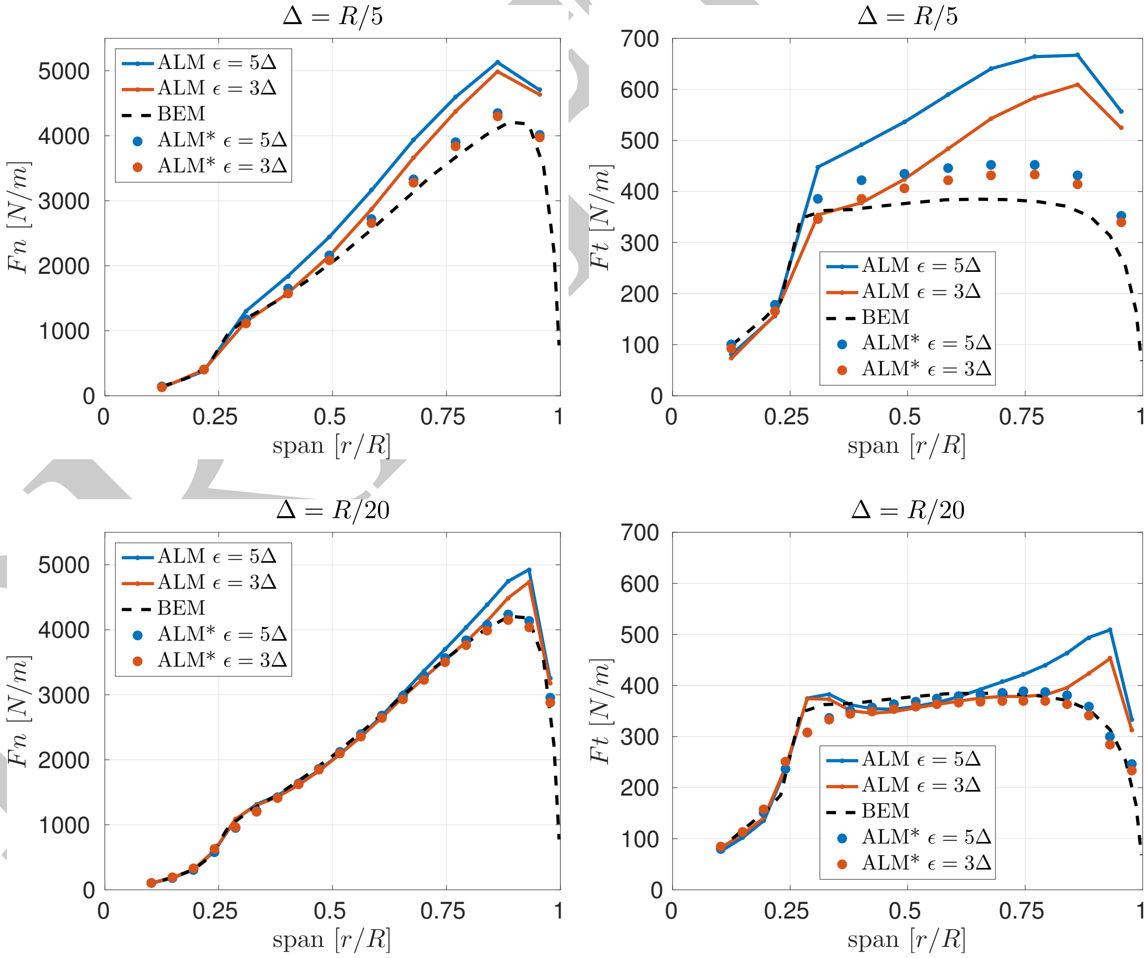

Figure 11. Comparison of normal and tangential loadings from ALM with and without the correction, and BEM computations for NREL 5MW turbine.

DTU Wind Energy is a department of the Technical University of Denmark with a unique integration of research, education, innovation and public/private sector consulting in the field of wind energy. Our activities develop new opportunities and technology for the global and Danish exploitation of wind energy. Research focuses on key technical-scientific fields, which are central for the development, innovation and use of wind energy and provides the basis for advanced education at the education.

We have more than 240 staff members of which approximately 60 are PhD students. Research is conducted within nine research programmes organized into three main topics: Wind energy systems, Wind turbine technology and Basics for wind energy.

Technical University of Denmark
Department of Wind Energy
Nils Koppels Allé
Building 403
2800 Kgs. Lyngby
Denmark
Telephone 46 77 50 85

info@vindenergi.dtu.dk
www.vindenergi.dtu.dk